COLOR PREDICTING MODEL FOR ELECTROPHOTOGRAPHIC PRINTS ON COMMON OFFICE PAPER

THÈSE № 2708 (2003)

PRÉSENTÉE À LA FACULTÉ INFORMATIQUE ET COMMUNICATIONS

SECTION D'INFORMATIQUE

ÉCOLE POLYTECHNIQUE FÉDÉRALE DE LAUSANNE

POUR L'OBTENTION DU GRADE DE DOCTEUR ÈS SCIENCES TECHNIQUES

PAR

SAFER MOURAD

Dipl. El.-Ing. ETH
de nationalité suisse et originaire de Bäretswil (ZH)

acceptée sur proposition du jury:

Prof. R.-D. Hersch, directeur de thèse
Dr P. Emmel, rapporteur
Prof. B. Kruse, rapporteur
Dr K. Simon, rapporteur
Prof. S. Süsstrunk, rapporteur

Lausanne, EPFL
12. 2. 2003

To

our children,

Luzia

and my parents

وَ لِأَهلِي في دِمَشق

Acknowledgments

I would like to express my sincere gratitude to my supervising Professor Roger David Hersch at the Ecole Polytechnique Fédérale de Lausanne, for his support and trust. Despite the distance between Lausanne and St. Gallen, he managed to support me with careful advice, continuous inspiration, encouragement and confidence. I would also like to thank Dr. Patrick Emmel for his steady company and his constructive comments during our repeated review meetings. Special thanks go to my mentor, Dr. Klaus Simon, for his leadership and encouragement. His constructive and critical questions were an incomparable stimulus and always helped me to consider issues in greater depth. Additionally, I appreciated the guidance and objective input from Prof. Viktor Ostromoukhov, Dr. Isaac Amidror and Nicolas Rudaz during the initial scientific reviews.

I would also like to thank my other examiners, Prof. Björn Kruse, Prof. Sabine Süsstrunk and Prof. Pascal Fua for participating on the jury, I am looking forward to an inspiring discussion of this thesis.

Many colleagues have generously given me the possibility to benefit from their experience. Special thanks are due to the staff members of the Media Technology Department at the Swiss Federal Laboratories for Materials Testing and Research. I address my acknowledgment to Prof. Kurt Schläpfer, Karl Heuberger and Dr. Hansjörg Künzli for preparing the cooperation with the EPFL, Dr. Kurt Münger, Walter Steiger, Markus Dätwyler, Erwin Widmer, Hans Schefer, Urs Bünter, Brigitte Bänziger, Donata Faust, Beat Trachsler, Marion Frey, and Karl Kurz for introducing me into the vibrant field of graphic arts industry and for always being available for discussions and assistance. Many thanks also go to our reliable librarian, Martin Meier, and to Dr. Beat Münch alias Úlfar Steingrímsson for being a demanding, interesting and helpful workmate.

Without the support of my wife, my daughters, my family and my friends I would have only got halfway through the project. They added to and enriched my daily experience with curiosity, spontaneity, acumen and endurance. I owe them my deepest gratitude.

St. Gallen, November 2002
Safer Mourad

I enthusiastically recommend the principal software used: GNU Emacs, MikTeX, LaTeX, The Memoir Class, $\mathcal{A}\mathcal{M}\mathcal{S}$-LaTeX, PXfonts, AdineKirnberg-Script font, Graphicx, Ghostscript, GSview, MathWorks MATLAB™, Wolfram Research's MATHEMATICA®, Adobe Acrobat® and PostScript™.

Abstract

Digital color desktop printers are widely used in modern offices. However, the ability of the printers to reproduce input colors faithfully is limited and they need to be recalibrated frequently. This is a time-consuming and cumbersome process, which usually needs to be carried out manually.

In order to simulate the interaction of light and color prints and to facilitate the calibration process, this thesis proposes new models for digital color printers and more specifically for dry toner electrophotographic printers. The proposed mathematical models describe the main contributing physical phenomena and offer support for the closed loop control of color halftone printers.

A first model concerns the phenomenon of light scattering within paper and takes into account the fluorescence of brightened office papers. Given the spectral point transmittance of a halftone patch, the model estimates the spectral point reflectance. It is verified by spectral microscopic measurements and is able to estimate the optical dot gain in halftone prints and its effect on the color reproduction curve of common printed papers.

A second model simulates the behavior of the electrophotographic printing process. Starting from the input bitmap of a color halftone, the simulation model computes the microstructures of the toner deposition on a given printing substrate. Assuming non light scattering toners, the obtained toner relief is transformed into the spectral point transmittance required by the first model.

For an electrophotographic printer, both models together allow an accurate estimate of the spectral color response and its description as a function of given input halftoned color separation layers.

Résumé

Les imprimantes de couleur numériques sont largement utilisées dans les bureaux d'aujourd'hui. Toutefois, leur capacité à reproduire fidèlement des images couleur reste limitée, et elles doivent être fréquemment calibrées. Il s'agit-là d'un procédé long et pénible que l'utilisateur doit habituellement faire à la main.

Afin de faciliter le calibrage de ces appareils, la présente thèse propose de nouveaux modèles pour l'impression couleur et, plus particulièrement pour les imprimantes électro-photographiques à toner sec. Les modèles mathématiques proposés englobent les phénomènes physiques principaux et permettent ainsi la claibration des imprimantes en circuit fermé.

Un premier modèle se rapporte au phénomène de la dispersion de la lumière dans le papier et tient compte de la fluorescence des papiers blanchis utilisés dans les imprimantes de bureau. Sur l'indication du microprofil spectral de transmission d'une plage tramée, le modèle évalue le porfil de réflectance. Les résultats du modèle sont vérifiés par des mesures microspectrophotomètre. Le modèle estime le gain de tonalité optique dans les impressions tramées, ainsi que ses effets sur la courbe de reproduction de couleur dans les procédés usuels d'impression sur papier.

Un deuxième modèle simule le comportement du processus d'impression électro-photographique. En partant des plans de bits des trames couleur, le modèle de simulation calcule la microstructure du dépôt de toner sur un support d'impression donné. A partir des spectres de transmission du toner, le relief du toner permet d'obtenir le microprofil spectral de transmission requis pour le premier modèle.

Pour une imprimante électrophotographique, les deux modèles réunis assurent une évaluation précise de la réponse spectrale des couleurs en fonction des séparations couleur tramées définies en entrée.

Contents

Introduction

1 Introduction

One goal of this thesis is to support the task of *designing* digital printers by proposing a comprehensive mathematical model. Designing new printing devices is rather complex and requires developing several mutually dependent submodules. In order to meet the required print quality, each submodule must be properly specified and parameterized.

Another goal is minimizing the time and cost involved in the *characterization* and *calibration* of digital color printers. These tasks are necessary in order to obtain a relationship between the specific amounts of printer inks needed to reproduce any device independent of input color. Usually, the characterizing relationship is acquired by measuring thousands of printed colors and tabulating the results in accordance with the input color values. Printing a specific color is then controlled by inverse lookup table operations. Despite the simple use of such a technique, the tasks involved are cumbersome, time-consuming and inaccurate. Modifications of a single printing parameter, such as the paper or ink, entail a complete recalibration.

Introducing models based on physical characteristics improves the understanding of the participating subprocesses, and clarifies the interaction between them. This facilitates the analysis and verification of the design and helps to shorten the invention cycles. The proposed models support the printer characterization process, and enable frequent automatic recalibration.

A short historical and scientific survey of paper, its properties and color printing is given in part I. It presents basic optical models of color filters and reviews classical prediction models of halftone prints. This part concludes with a short overview of the shortcomings of the classical models and illustrates the needs for novel approaches.

A new model characterizing light scattering and fluorescence of brightened office papers is presented in part II. Given the spectral transmittance microprofile of a halftone patch, the model estimates the spectral reflectance of the halftone print on a paper sheet. Performing a three-dimensional light scattering analysis within the body of paper, the model predicts the effects of the optical dot gain on the color of halftone prints. Considering lateral scattering of light, it extends the Kubelka–Munk theory and derives a closed analytical solution in the Fourier domain, which is evaluated numerically. Furthermore, the model takes into account multiple reflections within the interfaces of both sides of the paper in order to accurately estimate the measured reflectance profile of the color print.

Part III introduces a second model, which simulates the behavior of the electrophotographic printing process as an example for well established digital printers. Given the input bitmap of a color halftone, the simulation model predicts the deposited toner microstructure on a paper sheet. Assuming non-light scattering inks and applying Bouguer–Beer–Lambert's law, the obtained microscopic toner relief is transformed into a microscopic spectral transmittance profile. This transmittance profile is needed by the light scattering model.

The toner deposition model estimates the printed microstructure by starting from an input bitmap and simulating the effects of all main electrophotographic process steps. They comprise the exposure of the bitmap, the forming of the attracting electrostatic field, the toner random charge and diameter distributions, the toner transfer and color accumulation, as well as the final fusing step.

The numerous model coefficients are fitted using spectral measurements of about thirty printed halftone patches. Using both models sequently makes it possible to estimate the spectral color response of an electrophotographic printer as a function of any given input color bitmap. The thesis concludes with an experimental report demonstrating the achieved accuracy of the prediction.

2 History of paper and color printing

Throughout history, reproduction material and technologies have developed alongside each other. This chapter presents a historical synopsis of their evolution. It also points out the relevant optical and technical aspects, which limit the controllability of modern printing technologies.

2.1 Paper, a recording substrate

Writing is an essential component of any civilization. The development of pictographic writing dates back to the Sumerians in the Middle East during the fourth millennium BC. In the third millennium, their pictograms evolved into wedge-shaped characters inscribed on clay tablets, called the cuneiform writing system. The small clay tablet shown in figure 2.1 depicts the oldest yet found, almost

Figure 2.1: Ugarit cuneiform alphabet exhibited at the Damascus Museum

complete alphabetical order of 27 different Hebrew-Phoenician characters. It was excavated from the ruins of Ugarit near Ra's Shamra in Syria. It demonstrates the use of clay as a recording medium at a time when paper still was unknown to mankind. Beside clay, various other materials such as wood, papyrus, parchment, vellum, cloth, tree leaves and bark have been used for the same purpose. Of these, papyrus has played a major role in history.

2.1.1 The invention of paper and its properties

The word *paper* stems from the Greek and Latin words for papyrus. The oldest use of written papyrus rolls dates back to the third millennium BC. With the

invention of paper during the second century BC in China, a light, practical and cheap medium took over the role of recording written information. From China, papermaking moved to Korea in the sixth century AD, from where it was brought to Japan. The Chinese took their craft to Tibet, central Asia, India and, by the eighth century, the Middle East. Finally, papermaking reached Europe by the turn of the first millennium. However, it took another four hundred years until paper was accepted in Europe as a replacement for parchment or vellum for official records [Kip01, IPS].

Paper ingredients

Paper consists of fibers that are agglutinated and felted together in a tabular structure by thermo-mechanic and chemical treatment. In modern paper plants, the fibers are sprayed on a net running at a speed of about 1800 m/min. In this process, the fibers are mainly oriented in the running direction, forming an anisotropic material. 70 – 95% of paper consists of mostly natural fibers and up to 30% of functional additives. The choice of additives depends on the trade-off between economic, fiber bonding, paper opacity and brightness factors.

Optical properties

The bulk appearance of paper is neither perfectly dense nor opaque. Light illuminating the paper surface enters the substrate and scatters many times among the filler particles and millions of fibers. The induced *multiple* or *dependent scattering* is a phenomenon which makes it very difficult to track tracking the light path accurately within the body of paper. This complicates any accurate prediction of the optical properties of a sheet of paper. Although an isolated fiber resembles a tube of glass, it is too small to permit an accurate application of Fresnel's law, and the problem of analyzing its interaction with light using Maxwell's equations is as yet unresolved. This makes the application of classical, first principles analysis to paper impractical [Ran82]. Nevertheless, as of the twentieth century, instrumentation of paper appearance succeeded in ranking the different characteristic grades of paper and ensuring its manufacturing quality control. Supported by the development of photoelectronic components and several standardization efforts, different types of instruments and measurement techniques have found wide acceptance in scientific and graphic labs [Hun98]. However, nearly all of the instruments used rely on simulating of the visual assessment of color, gloss and other properties. Therefore, it is crucial for the quality assurance of an instrument to use light sources with well-known spectral power distribution and to keep the geometric setup close to standard specifications.

Optical instrumentation

2.2 Color printing

The invention of printing was a key event in the cultural advancement of the Middle Ages towards contemporary civilization. With his pioneering invention of the letterpress in the fifteenth century, Johannes Gutenberg laid the foundation for modern reproduction technology. Meanwhile, color was already recognized as an independent cultural feature and colorists made every effort to create dense

and shiny colors. Reproductions were colored either for decorative purposes by using solid colors or for illustrations executed by wooden or metallic cut masters.

At that time, color mixing was based on empirical knowledge and not developed in the sense of optimum ink consumption. The first documented *trichromatic* color illustration technique was introduced by Jacob C. Le Blon in the early eighteenth century [Fie99]. Inspired by Isaac Newton and convinced of the *triple* nature of color, he engraved plates by hand and used blue, red and yellow inks to reproduce full-color illustrations. The present-day *process colors cyan*, *magenta* and *yellow* were introduced in order to meet an optimum gray balance and to reproduce technically as many different color shades as possible (see [Sch02, p. 112] and [Kip01, p. 83]).

Illustrating technique

Most traditional printing technologies are unable to directly reproduce intermediate tones. They are only capable of printing limited tone levels, which makes it difficult to illustrate continuous shades. Most devices either print or do not print dots, and are thus known as *bilevel* or *binary* printers. It was only in the late nineteenth century with the invention of the *autotypical halftoning* process by Georg Meisenbach that modern illustration techniques were finally launched [Leu93]. To reproduce intermediate tones, the image is broken down into tiny picture elements, which are beyond the visible spatial resolution. Viewed from a certain distance, the halftoned screens are seen by the observer as the original tonal distribution, due to the spatial integration performed by the human eye.

Autotypical color synthesis

The placement of dots in multicolor prints induces two different types of *color mixing* principles. On the one hand, non-scattering ink dots printed all over the others act almost like a pile of absorbing filters. This principle is known as *subtractive* color mixing, referring to the spectral reducing property of the filters. On the other hand, the perceived color of adjacently placed dots is achieved by integrating the color stimuli of each one of them, which is common to the *additive* color mixture [WS82, p. 31 & 118]. The overall color composition of both principles is called *autotypical color synthesis* [Kip01, p. 81].

2.3 Impairment of halftone prints

Optical dot gain

Halftone prints on paper are particularly influenced by the phenomenon of light scattering. Light that strikes an unprinted area between printed dots scatters within the substrate and emerges under the dithered ink film and vice versa. This creates a smoothing effect called the *optical dot gain* [Gus97]. It causes bright halftoned tints to appear at a higher lightness level, while the surrounding white part tends to appear darker. With decreasing dot sizes of modern high resolution printers, this effect becomes more and more significant.

Mechanical dot gain

Another factor that affects halftone prints is the variation in size and shape of the printed dots. With increasing resolution, the ability of the printer to reliably reproduce isolated dots is limited, and the distorted dots begin to have a major

impact on the resulting images [HK98, LA01]. The deviation between the attained dot formation and the intended shape is called the *mechanical dot gain*.

In order to calibrate modern printers, both the optical and the mechanical dot gain have to be considered. However, up to now, most printer calibration routines are still manual processes, based on repetitive measurements and experiments. Calibrating halftone printers has therefore become cumbersome, not always accurate, quite time-consuming and expensive.

3 Basics of colorimetry

To produce a color printing model, it is essential to understand the composition and the perception of printed colors. While the fundamental spectral property of light and the trichromatic nature of color vision have been known since the early eighteenth century, it took an additional century for their mathematical instrumentation to appear. This chapter briefly introduces the colorimetric theories most relevant to the thesis.

3.1 Color measurement

The accuracy of color reproduction is one of the main quality measures of modern prints. However, color is not a physical quantity, it is an optical phenomenon sensed by the eye and perceived by the brain. The sensation of different colors is produced by viewing, at certain given conditions, irradiated objects that reflect different spectral parts of light. The spectral composition of such a stimulus is the only accessible physical variable that can be reliably determined. Regarding the perception of color, the *International Commission on Illumination (Commission Internationale de L'Éclairage or CIE)* provides standards and models approximating the response of the human eye to color.

According to this instrumentation and these recommendations, the performance of a color reproduction model can be reported by root mean square (*RMS*) spectral radiation difference as a physical scale, and by applying the CIE color difference formulae as a psychophysical scale [WB00]. The underlying measurements are made by commercially available *spectrophotometers*. These instruments measure the ratio of visible radiant power leaving the sample, to the power incident on it at successive wavelength bands $\Delta\lambda_i$. According to measurement geometry, a distinction is drawn between the *spectral reflectance factor* R_λ and the *spectral transmittance factor* T_λ. The following sections introduce these spectral factors as well as colorimetric aspects and distance specifications useful for the experimental investigation.

3.1.1 Spectral reflectance and transmittance factors

Terminology

Reflection and *transmission* define the processes of radiation being returned by or passed through a medium without any change in wavelength. *Reflectance* and *transmittance* are the measured quantities describing these phenomena. Typically, they are measured in relative terms of radiometric quantities, which is the subject of *spectrophotometry*. The term *factor* is used when the collected radiation lies within an isolated geometric cone of the covering hemisphere. However, for simplicity, this term is omitted after this chapter without confusing the physical relations. If the radiant power is determined for successive wavelength intervals, the adjective *spectral* is used [Hun98, p. 47,255].

Spectrophotometers

Most common spectrophotometers use a (45/0°)-observing condition as recommended by CIE. The illumination unit generally consists of a cone-shaped glass illuminated by up to three different unpolarized light sources. This setup produces an approximately circular illuminating condition, which helps to diminish the measurement dependencies on the sample orientation. Within the visible wavelength range at consecutive wavelength steps λ_i, well calibrated instruments provide averaged concentrations of radiant power $\langle P_\lambda \rangle_i$ per successive small-width band $\Delta\lambda_i$ [WS82, p. 230]

$$\langle P_\lambda \rangle_i = \frac{\int_{\lambda_i-\Delta\lambda_i/2}^{\lambda_i+\Delta\lambda_i/2} \mathcal{P}(\lambda)\ \mathrm{d}\lambda}{\int_{\lambda_i-\Delta\lambda_i/2}^{\lambda_i+\Delta\lambda_i/2} \mathrm{d}\lambda} \ . \tag{3.1}$$

The symbol $\langle\cdot\rangle$ denotes the mean value operation, and the subscript indicates the ith captured *spectral* value. Both mathematical symbols are subsequently omitted. The integrated wavelength bandwidth $\Delta\lambda$ reaches a typical range of about 10 nm and is determined by the applied device that isolates narrow portions of the spectrum called the *monochromator*. This considerable bandwidth averages out any effect of *optical interference* among the various transmitted and reflected beams within the observed filter layers.

Spectral factors

In practice, the *spectral reflectance factor* R_λ is determined by the spectral ratio of radiant power P_λ reflected from an object relative to the radiant power P_{D_λ} reflected from a *perfectly reflecting diffuser* identically illuminated [CIE78]

$$R_\lambda = \frac{P_\lambda}{P_{D_\lambda}} \ . \tag{3.2}$$

Usually, the perfectly reflecting diffuser is replaced by a calibrated *white standard*. Accordingly, the *spectral transmittance factor* T_λ is obtained by replacing the divisor of eq. (3.2) with a perfect transmitting diffuser and by applying (0/0°) transmission geometry. These spectrophotometric quantities are expressed as either percentages (0 − 100%) or as factors (0.0 − 1.0) [Fai97, p. 73].

The spectral reflection and transmission data of non-fluorescent materials are illuminant-independent. They describe the spectrum of an object observed in a given geometry. However, these measures on their own cannot account for the human visual response, where the same object appears differently in changed illumination conditions and which has only three color sensors.

Psychometric drawbacks

3.1.2 CIE *XYZ* tristimulus values

In order to handle the above-mentioned drawbacks of the measured spectra, foundations of trichromatic colorimeters have been investigated mainly by Wright [Wri28], Guild [Gui31] and others. Supported by Grassman's law [Gra53] of the additive color mixture and the principles of trichromacy, they studied chromatic matchings with experiments executed by independent groups of observers. The goal was to record the amounts of three additive primaries required to visually match each of the color stimuli presented in a viewing field of 2°. In 1931 the results gave rise to the introduction of the *CIE standard colorimetric observer* in terms of tabulated *CIE color-matching functions* $\bar{x}_\lambda$, $\bar{y}_\lambda$ and $\bar{z}_\lambda$, on which modern-day colorimetry is still based [CIE86]. Later, in 1964, the *CIE* recommended the new color-matching functions for more accurate correlations of visual color matching of fields with an angular subtense greater than 2°. The new color-matching functions, $\bar{x}_{10_\lambda}$, $\bar{y}_{10_\lambda}$ and $\bar{z}_{10_\lambda}$, define the *CIE supplementary standard colorimetric observer*. These functions were supplied by color-matching experiments of a 10° field completed by Stiles and Burch [SB59] and Speranskaya [Spe59].

As proposed by CIE, the *tristimulus values* of an illuminated object with the spectral reflectance R_λ is the mathematical spectral product integration over the total region of visible light

CIE XYZ

$$
\begin{aligned}
X &= k \int_\lambda R_\lambda \cdot I_\lambda \cdot \bar{x}_\lambda \, \mathrm{d}\lambda \,, \\
Y &= k \int_\lambda R_\lambda \cdot I_\lambda \cdot \bar{y}_\lambda \, \mathrm{d}\lambda \,, \\
Z &= k \int_\lambda R_\lambda \cdot I_\lambda \cdot \bar{z}_\lambda \, \mathrm{d}\lambda \,, \\
k &= \frac{100}{\int_\lambda I_\lambda \cdot \bar{y}_\lambda \, \mathrm{d}\lambda} \,,
\end{aligned}
\tag{3.3}
$$

where X, Y and Z are the obtained tristimulus values of the object, and I_λ is the relative spectral power distribution of the light source or illuminant of interest. Applying the normalization constant k as defined in eq. (3.3) implies the use of the *relative colorimetry* concept. The tristimulus values for transmitting materials are determined by replacing R_λ with the spectral transmittance T_λ. In this thesis, all colorimetric calculations were performed applying the color-matching functions $\bar{x}_\lambda$, $\bar{y}_\lambda$ and $\bar{z}_\lambda$ and the standard illuminant D_{65} in accordance with the *CIE* colorimetric recommendations.

3.1.3 CIE *LAB* color space

CIELAB (1976) is one of the *uniform color spaces* recommended by CIE that provides a perceptually more equidistant metric of color differences. The dimensions introduced in CIELAB correspond to the perceived lightness, chroma and hue of an object color viewed by an observer adapted to average daylight. The introduced space applies to comparisons of differences between object colors of the same size and shape, viewed in identical white to medium-gray surroundings [CIE78, p. 19].

Uniform color space

The CIELAB calculation is based on a nonlinear compression of the tristimulus values X, Y and Z normalized to the tristimulus of the *reference white* X_n, Y_n and Z_n. The nonlinear compression was designed to account for the typical relation between physical energy measurements and perceptual responses

CIELAB

$$\begin{aligned} L^* &= 116 \cdot f\left(\frac{Y}{Y_n}\right) - 16 \,, \\ a^* &= 500 \cdot \left[f\left(\frac{X}{X_n}\right) - f\left(\frac{Y}{Y_n}\right) \right] \,, \\ b^* &= 200 \cdot \left[f\left(\frac{Y}{Y_n}\right) - f\left(\frac{Z}{Z_n}\right) \right] \,, \end{aligned} \tag{3.4}$$

$$\text{with} \qquad f(x) = \begin{cases} \sqrt[3]{x} & \forall x > 0.008856 \\ 7.787 \cdot x + \frac{16}{116} & \forall x \leq 0.008856 \,. \end{cases}$$

The symbol $\forall$ is read as "for all". The introduced coordinates are used to construct a Cartesian color space. L^* represents *lightness*, a^* *redness-greenness* and b^* *yellowness-blueness* respectively. The cylindrical representation of the same space is given by the radius C^*_{ab}, which is called the *chroma* of the color, and the *hue* angle h_{ab}

Chroma and hue

$$\begin{aligned} C^*_{ab} &= \sqrt{a^{*\,2} + b^{*\,2}} \,, \\ h_{ab} &= \arctan\left(\frac{b^*}{a^*}\right) \,. \end{aligned} \tag{3.5}$$

3.1.4 Color difference formulae

Though not strictly attained, the CIELAB color space is considered to be perceptually uniform throughout the space. Therefore, perceptual color differences ΔE^*_{ab} are as simple as a Euclidean distance between the coordinates of two stimuli

ΔE^*_{ab}

$$\Delta E^*_{ab} = \sqrt{\Delta L^{*\,2} + \Delta a^{*\,2} + \Delta b^{*\,2}} \,. \tag{3.6}$$

A barely perceptible difference is equal to about 1 ΔE^*_{ab} unit [Hun98]. In 1994, CIE recommended a revised color-difference system for industrial use called the CIE ΔE^*_{94}. The color-difference system improves the uniformity of the color-difference

metric and is calculated as follows [CIE95]

$$\Delta E^*_{94} = \sqrt{\left(\frac{\Delta L^*}{k_L \cdot S_L}\right)^2 + \left(\frac{\Delta C^*_{ab}}{k_C \cdot S_C}\right)^2 + \left(\frac{\Delta H^*_{ab}}{k_H \cdot S_H}\right)^2}\,, \tag{3.7}$$

$\Delta \mathbf{E}^*_{94}$

with

$$\begin{aligned}
\Delta H^*_{ab} &= \sqrt{\Delta a^{*\,2} + \Delta b^{*\,2} - \Delta C^{*\,2}_{ab}}\,, \qquad \text{and} \\
k_L &= 1\,,\ k_C = 1\,,\ k_H = 1\,, \\
S_L &= 1\,, \\
S_C &= 1 + 0.045 \cdot \sqrt{C^*_{ab,1} \cdot C^*_{ab,2}}\,, \\
S_H &= 1 + 0.015 \cdot \sqrt{C^*_{ab,1} \cdot C^*_{ab,2}}\,.
\end{aligned}$$

The factors k_L, k_C and k_H adjust the weighting of lightness, chroma, and hue differences respectively. In addition, the CIE established a set of reference conditions that apply for the use of CIE ΔE^*_{94} [Fai97, p. 95]:

$\Delta \mathbf{E}^*_{94}$ reference conditions

Illumination:	CIE illuminant D_{65}
Illuminance:	1000 lux
Observer:	normal color vision
Background:	uniform, achromatic, $L^* = 50$
Viewing mode:	object
Sample size:	visual angle $\geq 4°$
Sample separation:	direct edge contact
Color-difference magnitude:	between 0 and 5 CIELAB units
Sample structure:	no visually apparent pattern or nonuniformity.

4 Optical models of color filters

Printed inks are either dissolved within a paper coating layer, as for instance in wet printing technologies, or they are adhered, pressed and melted on the paper surface as in most electrophotographic processes. Optically, these ink layers behave like color filters in direct contact with the printed substrate. Restricted to the case of *solid* prints, i.e. colors printed at 100% area coverage, this chapter introduces some mathematical approaches that can be used to analyze the optical properties of such a color filter.

4.1 Optical models of transparent color filters

Printing uses predominantly transparent or translucent inks that scatter light weakly. Thus, in an initial approach, printed layers are treated roughly as optical *absorption filters*. This section introduces the relevant optical models needed to analyze transparent color filters.

Ink specifications

The inks are assumed to be non-fluorescent, non-light scattering and non-metallic. They do not incorporate optical interferences that lead to an iridescent appearance. For further information about colors of various materials please refer to [Cal98].

4.1.1 Fresnel reflection

At the interface of an optical filter, part of the incident radiant power is lost due to *surface reflection* resulting from the discontinuity of the *refractive index*. Based on Fresnel's law, the reflectance ρ depends on the refractive index of the entering side medium n_{1_λ} and on the index of the filter itself n_{2_λ} as well as on the angle of incidence φ. Furthermore, ρ depends on the state of polarization, which is neglected due to the commonly used circular, homogenous illumination in color measurement equipment (section 3.1.1) .

For unpolarized illuminated nonmetallic filters, the Fresnel reflectance is given by [WS82, p. 52]

$$\rho_\lambda(\varphi) = \frac{\rho_{\lambda\parallel}(\varphi) + \rho_{\lambda\perp}(\varphi)}{2}\,, \tag{4.1}$$

with

$$\rho_{\lambda\parallel}(\varphi) = \left[\frac{\cos(\varphi) - \sqrt{\left(\frac{n_{2_\lambda}}{n_{1_\lambda}}\right)^2 - \sin^2(\varphi)}}{\cos(\varphi) + \sqrt{\left(\frac{n_{2_\lambda}}{n_{1_\lambda}}\right)^2 - \sin^2(\varphi)}}\right]^2,$$

$$\rho_{\lambda\perp}(\varphi) = \left[\frac{\left(\frac{n_{2_\lambda}}{n_{1_\lambda}}\right)^2 \cdot \cos(\varphi) - \sqrt{\left(\frac{n_{2_\lambda}}{n_{1_\lambda}}\right)^2 - \sin^2(\varphi)}}{\left(\frac{n_{2_\lambda}}{n_{1_\lambda}}\right)^2 \cdot \cos(\varphi) + \sqrt{\left(\frac{n_{2_\lambda}}{n_{1_\lambda}}\right)^2 - \sin^2(\varphi)}}\right]^2.$$

For normal radiant incidence angle ($\varphi = 0°$) eq. (4.1) reduces to

Fresnel's law

$$\rho_\lambda(0°) = \left(\frac{n_{1_\lambda} - n_{2_\lambda}}{n_{1_\lambda} + n_{2_\lambda}}\right)^2. \tag{4.2}$$

4.1.2 Internal spectral transmittance

After being partially reflected from the filter's boundaries, the remaining radiant power is transmitted and partly absorbed through the filter medium. The *internal* spectral transmittance of a homogeneous, transparent filter is defined by the ratio of the radiant power reaching the back surface of the filter to the power that entered the filter at its front surface. This quantity cannot be directly measured without specific arrangements. According to Bouguer's law, the internal transmittance ϑ_λ is given by

Bouguer's law

$$\vartheta_\lambda = 10^{-d \cdot m_\lambda}\,, \tag{4.3}$$

where d is the radiant *diffusion length* and m_λ is the *spectral absorptivity* of the medium. Beer's law refers the absorptivity of the medium for moderately concentrated, non-scattering liquids, to the product of the *extinction coefficient* ϵ_λ of the solution with its *concentration* c, hence

Beer's law

$$\vartheta_\lambda = 10^{-d \cdot c \cdot \epsilon_\lambda}\,. \tag{4.4}$$

By contrast, Lambert's law is often used to estimate transmittance values of filters that vary only in terms of their thickness [WS82, p. 31]. It relates the internal transmittance of the filter with a new thickness d to the reference internal transmittance ϑ_{0_λ} and its reference thickness d_0

Lambert's law

$$\vartheta_\lambda = \vartheta_{0_\lambda}^{\frac{d}{d_0}}\,. \tag{4.5}$$

4.1.3 Reflection and transmittance of transparent filters

The overall measured spectral transmittance τ_{f_λ} of an optical filter with plane-parallel surfaces is subject to internal reflections between its boundaries. Within the filter's boundaries, a part ρ_{i_λ} of the internal radiant power is reflected back into the medium due to the transition of the refractive index (see section 4.1.1).

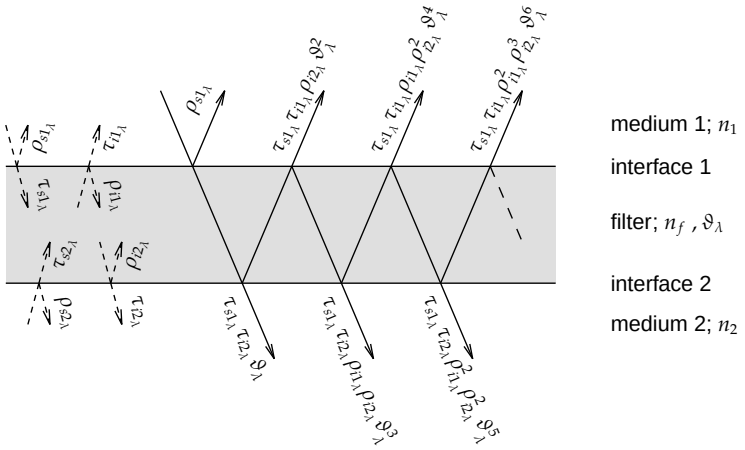

Figure 4.1: Internal reflections in a filter interfacing two different media. The dashed rays depict pure Fresnel factors.

Emerging through the filter again, the radiant is reabsorbed according to ϑ_λ, thus augmenting the filter's density. With a material transition and a given radiant incidence angle, the underlying Fresnel reflectance ρ_λ is basically equal to $1-\tau_\lambda$, where τ_λ is the Fresnel transmittance factor. However, this simple relation may lose its general validity if different illumination geometries are considered [JW75, p. 416]. Different factors are therefore observed, depending on the flux angle and direction.

Furthermore, the Fresnel reflectance and transmittance factors at both sides of the filter are not equal if the filter is interfacing two media of different refractive indices. According to figure 4.1, the multiple reflection process forms an infinite series of internal reflections and transmissions that defines τ_{f_λ}, yielding the generalized form of the filter transmittance and reflectance as follows [JW75, p. 440]

General filter transmittance and reflectance

$$\begin{aligned}\tau_{f_{12\,\lambda}} &= \tau_{s1_\lambda}\cdot\tau_{i2_\lambda}\cdot\vartheta_\lambda + \tau_{s1_\lambda}\cdot\tau_{i2_\lambda}\cdot\rho_{i1_\lambda}\cdot\rho_{i2_\lambda}\cdot\vartheta_\lambda^3 + \tau_{s1_\lambda}\cdot\tau_{i2_\lambda}\cdot\rho_{i1_\lambda}^2\cdot\rho_{i2_\lambda}^2\cdot\vartheta_\lambda^5 + \cdots \\ &= \tau_{s1_\lambda}\cdot\tau_{i2_\lambda}\cdot\frac{\vartheta_\lambda}{1-\rho_{i1_\lambda}\cdot\rho_{i2_\lambda}\cdot\vartheta_\lambda^2}\,, \qquad \text{and accordingly} \end{aligned} \tag{4.6}$$

$$\rho_{f_{12\,\lambda}} = \rho_{s1_\lambda} + \tau_{s1_\lambda}\cdot\tau_{i1_\lambda}\cdot\frac{\rho_{i2_\lambda}\cdot\vartheta_\lambda^2}{1-\rho_{i1_\lambda}\cdot\rho_{i2_\lambda}\cdot\vartheta_\lambda^2}\,, \tag{4.7}$$

where ρ_{i_λ} and τ_{i_λ} are the Fresnel reflectance and transmittance factors at the inner side of the considered interfaces. ρ_{s_λ} and τ_{s_λ} are the corresponding reflectance and transmittance factors at the surface of the interfaces. These factors depend on the

transition of the refractive indices which are almost constant over the measured wavelength range of light. Therefore, the dependence of the Fresnel factors upon the wavelength λ is ignored.

4.2 Optical models of translucent and turbid media

When light impinges on dissolved particles, such as colorant pigments or paper fibers, in addition to being partially absorbed, it is also scattered, changing its direction arbitrarily and several times in space. Light that passes through such a turbid media loses a considerable part of its intensity, and the relationship between the colorant concentration and the observed spectral response becomes more and more complicated.

The analysis of light scattering in translucent, *turbid media*, such as clouds, ice structures, human tissues, food and paper is a wide and yet increasingly active research field. Hereafter, a few of the classical approaches will be briefly reviewed. An extended survey of the reflectance theories for the reflectance of diffusing media is given in [PID01].

4.2.1 Survey of fundamental light scattering theories

Rayleigh scattering

Rayleigh scattering is a fundamental theory that provides a tool to analyze the phenomenon of light scattered by air molecules. According to this theory, the scattering power is strongly wavelength-dependent, which explains the blue appearance of the sky away from the sun. The theory can be extended to light scattered from particles with a diameter of up to a maximum of a tenth of the radiant wavelength. This restriction makes the theory impractical for analyzing the scattering of light in technical opaque or translucent media.

Mie scattering

The Mie theory, on the other hand, describes the scattered light from a single spherical particle with a diameter that may be even larger than the scattered wavelength. Mie scattering is less wavelength-dependent than Rayleigh scattering and explains the almost white glare around the sun and the neutral colors of fog and clouds. It is a *single scattering* theory that ignores any rescattered light from neighboring particles. Therefore, without being further extended, this approach does not apply to light scattered from an assembly of particles [GB80]. To circumvent this disadvantage, the *multiple scattering* approach is proposed for a particle crowding with an average separation between particles greater than three particle diameters. However, when the particle crowding gets tighter, the problem of *dependent scattering* begins to increase as Mie scattering starts to fail, due to wavelength-dependent interference between the neighboring scatterers.

Radiative transfer

Nevertheless, most colorimetric problems do not require such elaborate handling and, in technology, more emphasis is placed on simpler calculation methods. One of the most important simplified scattering approaches is based on a theory known in astrophysics as the *radiative transfer* [Cha60]. In its original form

it studies the transmission of light through absorbing and scattering media such as stellar and planetary atmospheres. The radiative transfer equations are rather complex, and the *multichannel technique* is a suitable approach that overcomes the imposed complexity. This technique subdivides the analyzed medium into as many channels as needed, each of them covering a different range of angles from the perpendicular to the horizontal [MR71, MR72]. Each channel is supplied with specific absorption and scattering coefficients, which determine how much light is being absorbed and scattered into other channels. The interesting aspect of this concept is its ability to connect the series of coefficients directly to Mie's theory. This helps to incorporate fundamental properties of the scatterer into the model, such as the particle size and the refractive index.

Reducing the number of considered channels even further, one arrives at the case of *two-flux* models proposed by Schuster [Sch05] and other authors. However, the Kubelka & Munk model, which is presented in the following section, is probably the most recognized approach and best suits the purpose of analyzing light scattered within colorant layers and paper sheets.

4.2.2 Kubelka-Munk's theory

The original theory of Kubelka and Munk [KM31] was developed for uniform colorant layers. Due to its simple use and its acceptable prediction accuracy, the model has become widely used in industrial applications [JW75, 3rd. chapter]. It is suitable for turbid layered media.

The eminent dimensionality of the scattering problem is reduced by assuming that light is being absorbed and scattered only in two directions, up and down. Thus, no special account need be taken of fluxes proceeding parallel to the boundaries, and only two vertical fluxes need be considered. The illumination of the top face of the turbid medium is expected to be homogeneous and diffuse. Besides being infinitely extended, the concept assumes that the medium forms a plane layer of constant, generally finite thickness. The material is presumed to be homogeneous, i.e. the optical inhomogeneities are incomparably smaller than the thickness of the specimen and uniformly distributed in the material. Finally, the material is assumed to emit no fluorescent radiation. In addition, it is assumed to have the same refractive index as the medium from which the light comes [Kub48, Kub54].

KM-theory assumptions

As depicted in figure 4.2 the colorant layer has a total thickness D and is in direct optical contact with a backing of reflectance R_{b_λ}. The model analyzes two fluxes through an elementary layer of thickness $\mathrm{d}z$, the flux $i_\lambda(z)$ proceeding downward, and $j_\lambda(z)$ simultaneously upward. The depth parameter z is considered to be zero at the background of the layer and D at the illuminated interface of the layer.

During its passage through $\mathrm{d}z$, the upward flux $j_\lambda(z)$ is attenuated by *absorption* $\alpha_\lambda \cdot \mathrm{d}z$ and by *scattering* downwards $\sigma_\lambda \cdot \mathrm{d}z$. At the same time, $j_\lambda(z)$ gains by

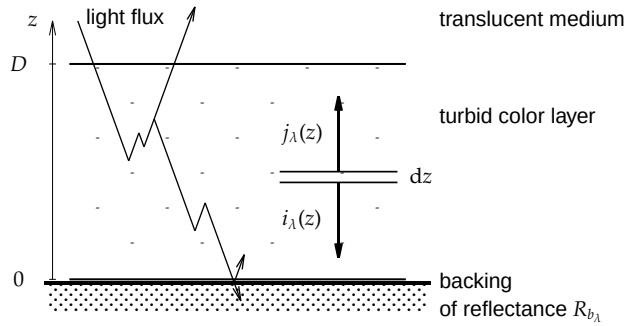

Figure 4.2: Light path consideration of the Kubelka–Munk model in conjunction with the depth coordinate z. Both light fluxes within the colorant layer are diffuse.

scattering from the opposed flux amount to $\sigma_\lambda \cdot \mathrm{d}z$ yielding the flux variation $\mathrm{d}j_\lambda(z)$ per thickness element $\mathrm{d}z$

$$\frac{\mathrm{d}j_\lambda(z)}{\mathrm{d}z} = \sigma_\lambda \cdot i_\lambda(z) - \left(\alpha_\lambda + \sigma_\lambda\right) \cdot j_\lambda(z) \ , \tag{4.8}$$

Kubelka–Munk light flux balances

The corresponding variation of the downward flux $i_\lambda(z)$ is derived in the same manner with the exception that $\mathrm{d}z$ is negative, as the process is occurring in the reverse direction,

$$-\frac{\mathrm{d}i_\lambda(z)}{\mathrm{d}z} = \sigma_\lambda \cdot j_\lambda(z) - \left(\alpha_\lambda + \sigma_\lambda\right) \cdot i_\lambda(z) \ . \tag{4.9}$$

The obtained differential equations (4.8) and (4.9) describe the net changes of both light fluxes, $i_\lambda(z)$ and $j_\lambda(z)$. The equations are classified to the *two-constant* theory, referring to the introduced colorant optical coefficients, absorption and scattering. Using calculus methods, Kubelka and Munk first solved these equations for the special case of a colorant layer with an opaque thickness, i.e. any further increasing of the layer thickness does not change its reflectance R_{∞_λ}

The material reflectivity

$$R_{\infty_\lambda} = 1 + \frac{\alpha_\lambda}{\sigma_\lambda} - \sqrt{\frac{{\alpha_\lambda}^2}{{\sigma_\lambda}^2} + \frac{2 \cdot \alpha_\lambda}{\sigma_\lambda}} \ . \tag{4.10}$$

Analyzing a thinner layer, the colorant appears translucent and the backing of reflectance R_{b_λ} starts to shine through. Kubelka and Munk gave a general solution for the reflectance R_{KM_λ} of such a translucent layer using eq. (4.10)

Exponential KM solution

$$R_{\mathrm{KM}_\lambda} = \frac{\frac{R_{b_\lambda} - R_{\infty_\lambda}}{R_{\infty_\lambda}} - R_{\infty_\lambda} \cdot \left(R_{b_\lambda} - \frac{1}{R_{\infty_\lambda}}\right) \cdot e^{\sigma_\lambda D \left(\frac{1}{R_{\infty_\lambda}} - R_{\infty_\lambda}\right)}}{R_{b_\lambda} - R_{\infty_\lambda} - \left(R_{b_\lambda} - \frac{1}{R_{\infty_\lambda}}\right) \cdot e^{\sigma_\lambda D \left(\frac{1}{R_{\infty_\lambda}} - R_{\infty_\lambda}\right)}} \ . \tag{4.11}$$

Equation (4.11) is known as the *exponential solution* of the Kubelka–Munk analysis. It ignores any surface or internal reflections at the colorant boundaries caused by

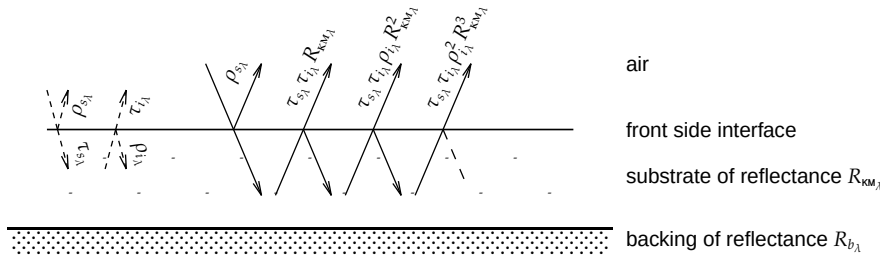

Figure 4.3: Internal reflections considered by the Saunderson correction. The dashed rays depict pure Fresnel factors.

the transition of the refractive indices. Usually, a measured reflectance R_{m_λ} of a colorant layer differs considerably from that R_{KM_λ} given in eq. (4.11).

Based on figure 4.3, Saunderson presented a convenient adjustment of the estimated value to the measurement, taking into account the ignored internal reflections [Sau42, eq. 6]

$$R_{m_\lambda} = \rho_s + \tau_s \cdot \tau_i \cdot \frac{R_{\mathrm{KM}_\lambda}}{1 - \rho_i \cdot R_{\mathrm{KM}_\lambda}} \,, \tag{4.12}$$

Saunderson correction

where ρ_i and τ_i are the internal reflectance and transmittance factors at the inner top boundary face. The emerging light flux $j_\lambda(z)$ at the top boundary is assumed to be completely diffuse. ρ_s and τ_s are the specular reflectance and transmittance factors of the incident light at the top surface of the layer.

5 Classical halftone prediction models

As introduced in section 2.2, halftoning is the technique of converting a continuous tone image to a screen of colored distinct dots of limited intensity levels. Both the *mechanical* and the *optical* dot gain introduce non-linearities in contrast to the linear processes assumed by most common color prediction models. Nevertheless, these color models provide first line prediction basics for printed patches and are therefore introduced in this chapter [EH99, Kan99, WB00].

5.1 Color mixing

Colors produced by halftone prints are perceived as a combination of subtractive and additive color mixing processes. *Subtractive color mixing* refers to the process in which light passes through absorbing filters with the spectral transmittance T_{i_λ}, which are brought into optical contact. The resulting spectral transmittance T_λ arises from a spectral *subtraction* of radiant power and is given in accordance to Bouguer–Lambert–Beer's law by multiplying its constituent spectral factors

$$T_\lambda = \prod_i T_{i_\lambda} \ . \tag{5.1}$$

Subtractive color mixing

An *additive color mixing* stimulus I_λ is a composition of different spectral power distributions. Each power contribution I_{i_λ} contributes to the resulting spectrum I_λ weighted by its relative amount of occupied viewing field f_i

$$I_\lambda = \sum_i f_i \cdot I_{i_\lambda} \ . \tag{5.2}$$

Additive color mixing

5.2 Murray–Davies, monochrome halftone model

The Murray–Davies model is a direct application of the additive color mixing theory and is the most rudimentary predicting model of monochrome halftone prints [Mur36]. Hereinafter, the terms *substrate* and *paper* are used synonymously. In its original form, the Murray–Davies model predicts the fractional *area coverage* a_t from a halftone optical-density value D, which is the normalized area covered by the printing ink. It is derived on the basis of figure 5.1, where the estimate $\hat{R}_\lambda$

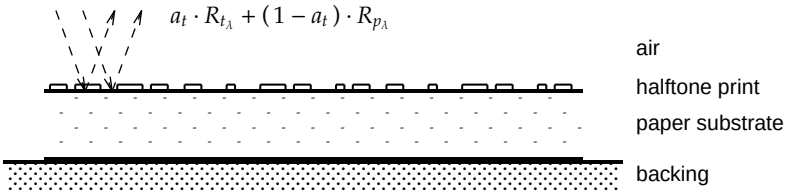

Figure 5.1: Light path considered in the Murray–Davies model.

of the spectral reflectance R_λ of a printed monochrome halftone is given by the weighted sum of the constituent reflectances

Murray–Davies spectral monochrome estimate

$$\hat{R}_\lambda = a_t \cdot R_{t_\lambda} + (1 - a_t) \cdot R_{p_\lambda} \; . \tag{5.3}$$

The hat symbol $\hat{\cdot}$ stands for the prediction of a corresponding measure. Solving eq. (5.3) for a_t and replacing the reflectance estimate by the measurement yields the simple area coverage estimate $\hat{a}_t$

Murray–Davies area coverage estimate

$$\hat{a}_t = \frac{R_\lambda - R_{p_\lambda}}{R_{t_\lambda} - R_{p_\lambda}} \; , \qquad \text{which is equal to} \qquad \hat{a}_t = \frac{1 - 10^{-D}}{1 - 10^{-D_t}} \; , \tag{5.4}$$

$$\text{where} \qquad D = -\log_{10}\Big(\frac{R}{R_p}\Big) \quad \text{and} \quad D_t = -\log_{10}\Big(\frac{R_t}{R_p}\Big) \, . \tag{5.5}$$

D_t is the normalized density of a monochrome ink of tint t printed at full area coverage. R_p is the reflectance of the bare unprinted substrate and R is the measured reflectance of the halftone print. Equation (5.5) establishes the relationship between normalized density terms and the reflectance spectra.

The Murray–Davies equation assumes uniform inked areas and an ideal and uniform substrate. Under these assumptions, the predicting equation can be considered a linear interpolation between the substrate reflectance and the reflectance of the printed ink. It is an intuitive, elementary physical approach that neglects many accompanying effects such as Fresnel's reflection and light scattering. In practice, the prediction is not satisfyingly accurate, neither with the theoretical area coverage $a_{t_{in}}$, nor with a fitted *effective area coverage* $a_{t_{fit}}$ obtained by fitting eq. (5.3) to the measured reflectance spectra R_λ simultaneously over all spectral values. A corresponding example of estimating a magenta halftone print is shown in figure 5.2. The input area coverage $a_{t_{in}}$ was set to 35.1%. With this nominal coverage, the prediction equation (5.3) yields a colorimetric error of as much as 44.7 ΔE^*_{ab} units. Also, the fitted effective area coverage $a_{t_{fit}}$ of 77.1% yields an estimation error of 11.7 ΔE^*_{ab}. These poor estimation accuracies demonstrate the nonlinearity of the halftoning process.

5.3 Yule–Nielsen correction

Light scattering is one of the main inaccuracy reasons in eq. (5.3). Based on figure 5.3, an elementary adjustment—called the Yule–Nielsen correction [YN51]—is

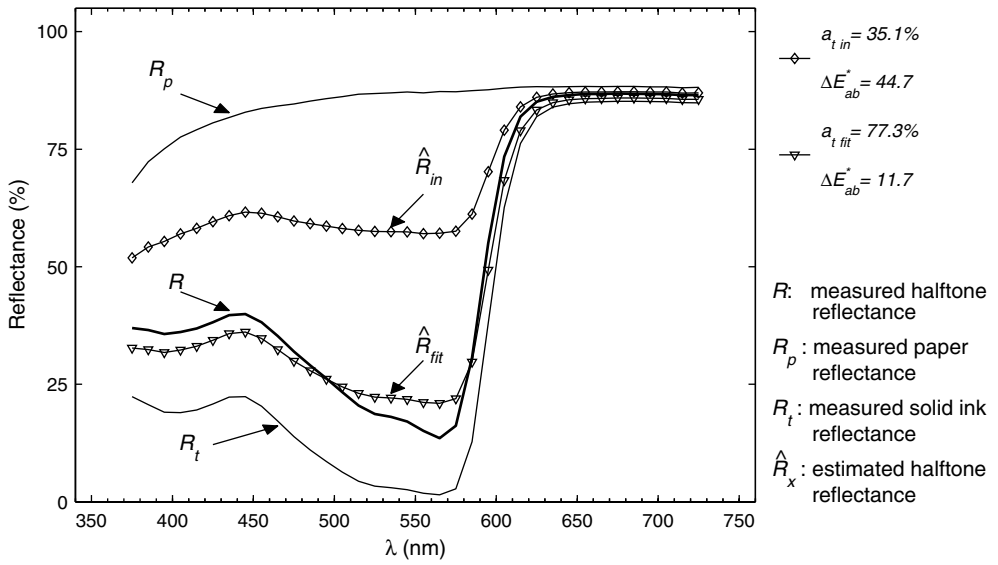

Figure 5.2: MURRAY–DAVIES based estimation of a magenta halftone print on an electrophotographic printer with a nominal area coverage of 35.1%. $\hat{R}_{in_\lambda}$ and $\hat{R}_{fit_\lambda}$ are the halftone reflectance estimates applying the input area coverage $a_{t\,in}$ and the fitted one $a_{t\,fit}$ as parameters of equation (5.3) respectively.

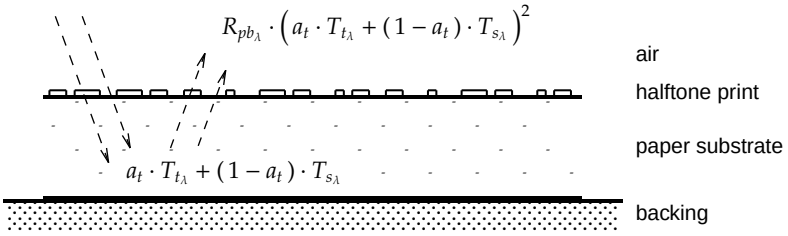

Figure 5.3: Considered light path in the YULE–NIELSEN model.

proposed for substrates with a large light diffusion length. Neglecting any FRESNEL reflection at the print surface, the transmitted light into the substrate is considered to be partially absorbed by a homogenous filter. Applying the MURRAY–DAVIES equation (5.3), the spectral transmittance t_λ of the print layer is given by

$$t_\lambda = a_t \cdot T_{t_\lambda} + (1 - a_t) \cdot T_{s_\lambda} \,, \tag{5.6}$$

with T_{s_λ} the transmittance of the paper-white surface, usually equal to 1. T_{t_λ} is the transmittance of the ink layer derived based on LAMBERT's law

$$R_{t_\lambda} = T_{t_\lambda} \cdot R_{p_\lambda} \cdot T_{t_\lambda} \,, \qquad \text{yielding} \qquad T_{t_\lambda} = \sqrt{R_{t_\lambda} / R_{p_\lambda}} \tag{5.7}$$

assuming light traveling back and forth through the ink. With increasing light diffusion length, the entered ray begins to be *completely scattered*, i.e. the probability that it will exit through an inked or non-inked area is independent of the entrance position and is proportional to its surface coverage a_t [Rog97]. Hence, the radiant power is diffusely reflected by the substrate inner reflectance R_{pb_λ} and is reabsorbed again by t_λ

Complete scattering

$$\hat{R}_\lambda = R_{pb_\lambda} \cdot \left(a_t \cdot T_{t_\lambda} + (1 - a_t) \cdot T_{s_\lambda} \right)^2 , \tag{5.8}$$

which is rearranged to

$$\hat{R}_\lambda = \left(a_t \cdot \sqrt{R_{t_\lambda}} + (1 - a_t) \cdot \sqrt{R_{pb_\lambda}} \right)^2 \tag{5.9}$$

$$\text{using} \quad R_{t_\lambda} = R_{pb_\lambda} \cdot T_{t_\lambda}^2 \quad \text{and} \quad T_{s_\lambda} \equiv 1 \, .$$

In order to improve fits of experimental data, Yule–Nielsen introduced their equation in a more general form. They proposed using an adjustable parameter n, called the *n-value*, as exponents in eq. (5.9)

Yule–Nielsen correction

$$\hat{R}_\lambda = \left(a_t \cdot \sqrt[n]{R_{t_\lambda}} + (1 - a_t) \cdot \sqrt[n]{R_{pb_\lambda}} \right)^n . \tag{5.10}$$

R_{pb_λ} is usually set to R_p, the bare paper or substrate reflectance. From a physical point of view, using n-values of $1 \leq n \leq 2$ accounts for intermediate light diffusion length, between Murray–Davies's non-scattering condition up to complete scattering [RH78]. However, in practice, some reports claim to achieve better fits using n-values higher than two, representing corrections of other effects, such as scattering inks, variations in dot densities [SM93, WB00] or internal reflections [Rog00]. Figure 5.4 illustrates a comparison of two predictions obtained by fitting

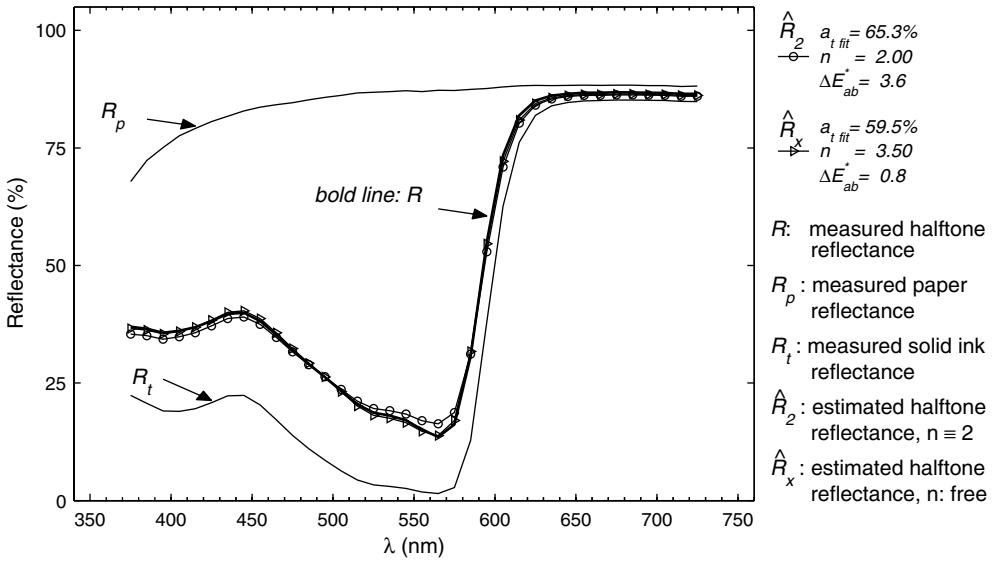

Figure 5.4: Yule–Nielsen based estimation (same data as in figure 5.2).

both parameters a_t and n of equation (5.10) simultaneously. The measured data are the same as those presented in section 5.2. The illustrated estimation $\hat{R}_{2_\lambda}$, marked by the circles, represents the case of complete scattering. It is obtained using a fitted area coverage $a_{t_{fit}}$ of 65% and a fixed n-value to 2, yielding an estimation error of 3.6 ΔE^*_{ab}. The second estimation $\hat{R}_{x_\lambda}$, marked by the triangles, is obtained with a simultaneously fitted effective area coverage $a_{t_{fit}}$ of 60% and an n-value of 3.5, yielding an error of less than 1 ΔE^*_{ab}.

5.4 Clapper–Yule, internal reflections model

Another approach in considering the effective light path within halftone printed substrates was proposed a couple of years later by Clapper–Yule [CY53], as illustrated in figure 5.5. Following an incident ray of unity power, a first component falls off by surface reflection ρ_{ap} due to the refractive index transition at the air-paper interface. The front side is considered to be formed mainly by the paper,

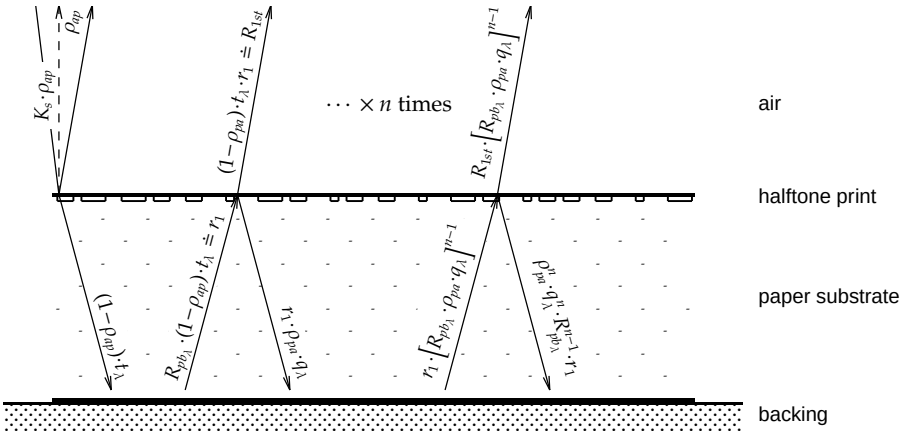

Figure 5.5: Considered light path in the Clapper–Yule model.

either without ink or with a given ink coverage. Using a 45/0°-spectrophotometer, only a part K_s of the surface reflection ρ_{ap} is measured. The outstanding remainder $1 - \rho_{ap}$ enters the substrate body and is attenuated at the ink layer by t_λ given in equation (5.6). Within the substrate and on its reverse side, the paper-backing boundary at the latest, the incident ray is partially absorbed and reflected by the paper's body inner reflectance R_{pb_λ}. Due to the different refractive indices at the front side, the ray emerging from the substrate loses a fraction ρ_{pa} by reflection at the paper-air boundary into the substrate body. The reflected fraction resumes a new cycle of internal reflections and passes through the ink layer a second time, hence it is attenuated by

$$q_\lambda = a_t \cdot T_{t_\lambda}^2 + (1 - a_t) \cdot T_{s_\lambda}^2 \ . \tag{5.11}$$

The estimated reflected light $\hat{R}_\lambda$ is then the sum of all the fractions emerging from the front side into the instrument aperture

$$\begin{aligned}
\hat{R}_\lambda = {} & K_s \cdot \rho_{ap} + && \textit{surface reflection} \\
& \left(1 - \rho_{ap}\right) \cdot \left(1 - \rho_{pa}\right) \cdot R_{pb_\lambda} \cdot \left(a_t \cdot T_{t_\lambda} + (1 - a_t) \cdot T_{s_\lambda}\right)^2 + && \textit{1st emergence} \\
& \left(1 - \rho_{ap}\right) \cdot \left(1 - \rho_{pa}\right) \cdot R_{pb_\lambda} \cdot \left(a_t \cdot T_{t_\lambda} + (1 - a_t) \cdot T_{s_\lambda}\right)^2 \times \\
& \quad \rho_{pa} \cdot R_{pb_\lambda} \cdot \left(a_t \cdot T_{t_\lambda}^2 + (1 - a_t) \cdot T_{s_\lambda}^2\right) + \cdots && \textit{2nd emergence} \\
& \left(1 - \rho_{ap}\right) \cdot \left(1 - \rho_{pa}\right) \cdot R_{pb_\lambda} \cdot \left(a_t \cdot T_{t_\lambda} + (1 - a_t) \cdot T_{s_\lambda}\right)^2 \times \\
& \quad \left[\rho_{pa} \cdot R_{pb_\lambda} \cdot \left(a_t \cdot T_{t_\lambda}^2 + (1 - a_t) \cdot T_{s_\lambda}^2\right)\right]^{n-1} \ . && \textit{nth emergence}
\end{aligned}$$

The sum of this infinite series yields

Clapper–Yule equation

$$\hat{R}_\lambda = K_s \cdot \rho_{ap} + \frac{\left(1-\rho_{ap}\right)\cdot\left(1-\rho_{pa}\right)\cdot R_{pb_\lambda}\cdot\left(a_t\cdot T_{t_\lambda} + (1-a_t)\cdot T_{s_\lambda}\right)^2}{1-\rho_{pa}\cdot R_{pb_\lambda}\cdot\left(a_t\cdot T_{t_\lambda}^2 + (1-a_t)\cdot T_{s_\lambda}^2\right)}\,, \tag{5.12}$$

which is particularly familiar to the Saunderson correction for solid prints equation (4.12).

Clapper–Yule's model is an extension of the Yule–Nielsen correction in its physically relevant complete scattering form, equation (5.8), taking into account the internal reflections at the boundary between the substrate and the air. Figure

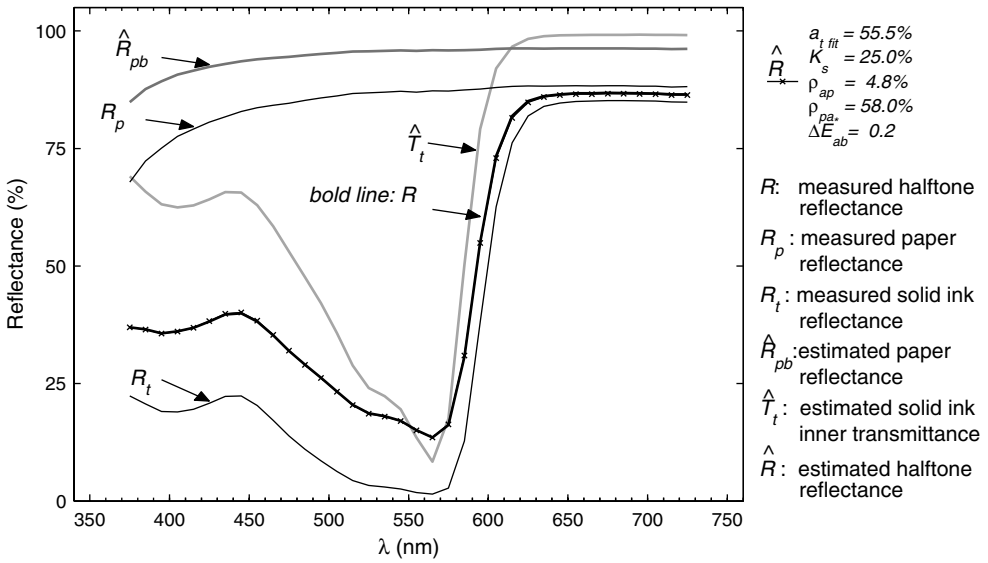

Figure 5.6: Clapper–Yule based estimation (same data as in figure 5.2).

5.5 illustrates a prediction example obtained by fitting all the unknown parameters of equation (5.12) simultaneously to spectral reflectance measurements of the paper-white R_{p_λ}, the solid ink R_{t_λ} and the halftone print R_λ. The unknown parameters comprise the area coverage a_t, the specular reflectance factor ρ_{ap} and its importance K_s, the inner reflectance factor ρ_{pa}, the inner substrate reflectance $\hat{R}_{pb_\lambda}$ as well as the inner ink transmittance $\hat{T}_{t_\lambda}$. The obtained estimate of the halftone reflectance $\hat{R}_\lambda$ is marked by the triangles. In accordance with the case of diffuse internal reflection reported by Judd [Jud42], the estimated inner reflection coefficient ρ_{pa} reaches 58% and the surface reflection ρ_{ap} equals 4.8%. K_s is 25% and $a_{t_{fit}}$ 55%. This application demonstrates the effectiveness of the Clapper–Yule model, yielding an almost exact match between the prediction and the results, with an estimation error of as little as 0.2 ΔE^*_{ab} on a halftone patch of the calibration set.

5.5 Neugebauer, halftone color predicting model

In color halftones, the dots of the process colors—cyan, magenta and yellow, (*CMY*)—are printed partially in overlap and partially adjacent to each other. The colors of the overlapped dots are combined according to subtractive mixing (section 5.1) producing red ($R = M + Y$), green ($G = C + Y$), blue ($B = C + M$) and black ($K = C + M + Y$). Analyzing such a trichromatic halftone print, Neugebauer recognized the additive-like behavior of these *dominant colors* in addition to the paper-white, the so-called eight Neugebauer-colors [Neu37]. According to eq. (5.2) the spectral reflectance estimate $\hat{R}_\lambda$ of the composed color is the sum of the reflectances of its constituent tints R_{t_λ} weighted by their respective spatial occupation f_t

three-primary Neugebauer spectral estimate

$$\begin{aligned}\hat{R}_\lambda = & f_w \cdot R_{w_\lambda} + f_c \cdot R_{c_\lambda} + f_m \cdot R_{m_\lambda} + f_y \cdot R_{y_\lambda} + \\ & f_r \cdot R_{r_\lambda} + f_g \cdot R_{g_\lambda} + f_b \cdot R_{b_\lambda} + f_k \cdot R_{k_\lambda} \ , \end{aligned} \tag{5.13}$$

$$\text{or} \qquad \hat{R}_\lambda = \sum_{i \in \mathcal{N}_{ngb}} f_i \cdot R_{i_\lambda} \ , \tag{5.14}$$

$$\text{with} \quad \mathcal{N}_{ngb} = \{w, c, m, y, r, g, b, k\} \qquad \text{the dominant color set .}$$

Obviously, if eq. (5.14) is extended by Yule–Nielsen to improve the results, the combination yields [Vig85, Vig90]

Yule–Nielsen extended Neugebauer

$$\hat{R}_\lambda = \left[\sum_{i \in \mathcal{N}_{ngb}} f_i \cdot \sqrt[n]{R_{i_\lambda}} \right]^n \ . \tag{5.15}$$

Given a statistical independent halftone color dot placement, i.e. if the *cross-correlation* between the color halftone planes are negligible, the spatial occupation factors f_t are easily calculated applying Demichel's equation [Dem24]

Demichel's dot overlap model

$$\begin{aligned} f_w &= (1 - a_c) \cdot (1 - a_m) \cdot (1 - a_y) \ , & f_r &= a_m \cdot a_y \cdot (1 - a_c) \ , \\ f_c &= a_c \cdot (1 - a_m) \cdot (1 - a_y) \ , & f_g &= a_c \cdot a_y \cdot (1 - a_m) \ , \\ f_m &= a_m \cdot (1 - a_c) \cdot (1 - a_y) \ , & f_b &= a_c \cdot a_m \cdot (1 - a_y) \ , \\ f_y &= a_y \cdot (1 - a_c) \cdot (1 - a_m) \ , & f_k &= a_c \cdot a_y \cdot a_m \ , \end{aligned} \tag{5.16}$$

using the input halftone area coverage a_t of the halftone process color planes.

5.6 Shortcomings of the classical models

Dot's irregularities

None of the reviewed classical models is able to predict the printer's correct spectral response as a function of the input color halftone screens. The input halftone is composed of digital pixels placed on a square digital grid. In practice however, depending on the printer characteristics, the screen dots are usually formed as a circle, an ellipsis, a square or other shapes [Kan99]. And, due to uncontrollable

process residuals, the reproduced screen dots may vary dramatically in shape from their ideal geometry, resulting in irregular, sometimes highly distorted dots. The resulting *distortion* of the dot formation causes major difficulties in estimating the effective area coverage of a particular halftone scheme at various tone levels. With increasing tone values, as soon as freestanding dots simultaneously join, they induce a non-continuous tonal reproduction curve yielding irregularities known as *tone breaks*. Finally, when printing with multiple primary colors it is most likely that different color halftone layers interfere with one another. In conventional printing technologies, this phenomenon is commonly referred to as ink *trapping*.

Tone break

Trapping

Printer calibration

To calibrate the printer tone reproduction curve without a model that considers these effects, it is common to follow a *lookup-table* approach. In the *device independent* color management approach, the CIELAB coordinates of thousands of printed color halftone patches are measured and tabulated according to the requested input color coverages (a_c, a_m, a_y and a_k). To a certain degree, the obtained table reproduces an acceptable numerical approximation of the characteristic reproduction curve. It is an empirical, so-called *forward* printer model, which predicts the color coordinates based on the *CMYK* printer input values. The inversion of this table by multidimensional nearest neighbor operation and interpolation yields the calibration profile needed for the printer. The calibration profile determines the *CMYK* input values that best reproduce the required CIELAB color coordinates.

Lookup-table drawback

However, the use of such a lookup-table is specific to the type of paper, the actual halftone scheme and to other process parameters that were valid during the calibration process. Changing one of the parameters forces the user to remeasure and recalibrate the profile; a cumbersome and time-consuming task.

Applying models that account for the physical characteristics of the reproduction process should facilitate the analysis and calibration of the system. Such a model is the subject of the subsequent investigation report.

Modelling light scattering in paper

6 Lateral light scattering in paper

Identifying and characterizing each subprocess of a whole system is the basis for any control and calibration approach. The color response of any printing device is greatly determined by the interaction between light and the paper used. This may be regarded as an independent subsystem. Paper is translucent, and the background shines through it. In addition, any incident or emerging radiant fluxes, into or from the paper, are affected by the refractive index transition at its interfaces. Hence, the optical properties of the paper body as well as of its top and bottom boundaries need to be carefully considered. This chapter analyzes the internal reflections at the upper and lower paper boundaries and proposes a model of lateral light scattering in the paper bulk. It extends the KUBELKA–MUNK approach in order to model the interaction of light with multi-color halftone prints.

6.1 Extending the KUBELKA–MUNK theory

Lateral light scattering is often modeled by a *point spread function* (*PSF*). In the literature, several approaches for modeling the PSF of paper are known. Most of them were determined empirically, see for instance [RH78], or they assume a specific type of function [FRGS82, Rog99]. Others are based on numerical simulations [Gus97, YGK01], microscopic reflectance measurements [AEZ95, SNY98], image processing [NG93], multi-flux theory [JVS01] or radiative diffusion [Rog97].

Nevertheless, due to its simplicity and relevance among the concurrent light scattering theories (section 4.2.1), the theory of KUBELKA–MUNK [KM31] has found widespread acceptance for modeling the reflectance and transmittance behavior of scattering dull materials with the same surface characteristics over a wide area. However, halftone prints cannot be regarded as infinitely wide colorant layers, and the original concept fails to predict their measured color. In this respect, a recent improvement was provided by BERG [Ber97]. He introduced a lateral analysis of scattering light and presented an approach based on KUBELKA–MUNK, which, by numerical evaluation, predicts the point transmittance and reflectance profile of an ideal line print. However, his approach remains limited to a two-dimensional model and ignores the influences of brightened paper or of internal reflections at the interfaces of the paper.

The present chapter proposes a model which analyzes the scattering light fluxes in a general three-dimensional space. The transition of the refractive index at the edges of the paper are taken into account by adjusting the SAUNDERSON correction and applying it to the boundary conditions of the scattering differential

equation system. These boundary conditions allow for the internal reflections at both interfaces of a single or double-sided printed paper sheet, where the reverse side is covered with a solid color or no color at all. Furthermore, the model considers the optical behavior of brightened papers, which is introduced in the following section.

6.1.1 Considering brightened papers

Basically, the optical properties of brightened office papers are affected by enclosed *fluorescent brightening* or *whitening* additives. The supplied brighteners absorb a certain energy of the ultraviolet (UV) rays within the invisible upper frequency band, called the *excitation spectrum* ϕ_{e_λ} [Emm98]. Then, a specific amount of the absorbed energy, determined by the *quantum yield*, is released by radiative relaxation in the visible band, called the *fluorescence spectrum* ϕ_{f_λ}. Fluorescent additives compensate for the yellowish appearance of natural non-brightened papers. Since the emission of the fluorescence spectrum occurs within the paper's body in all space directions, the fluorescent emission acts like a diffuse partial light source or converter. Consequently, the brightening effect amplifies the effects of the optical dot gain in the bluish range of the visible light and must be considered when analyzing the paper's point spread function (PSF).

Fluorescence affects the optical dot gain

In addition, according to the absorptance spectrum of the applied inks, any printed layer at the top of a brightened paper may absorb a part of the excitation spectrum by acting as an upper-frequency band filter (as will be seen in section 7.2.1). This filter reduces the fluorescent spectrum and, beneath the ink layer, the paper-white becomes yellowish again. For translucent inks, this effect emphasizes the importance of taking the fluorescence of the paper bulk into account.

Printed inks diminish the brightening effect

6.2 Three dimensional scattering analysis

Two analyzing approaches are presented in this section. The first analysis is carried out in a cartesian, three-dimensional coordinate system. The second analysis applies a simplifying cylindrical symmetry and is carried out in a polar coordinate system.

6.2.1 Light scattering in cartesian coordinates

Figure 6.1 illustrates the spectral light scattering analysis applied to a tiny volume cube of a paper sheet with a total thickness D, which is placed at the origin of a cartesian coordinate system x, y, and z. As with Kubelka–Munk's theory and Berg's approach, the concept assumes finite and continuous light fluxes within the medium. It analyzes the downward and upward oriented fluxes (i_λ, j_λ) in addition to the lateral fluxes along the increasing and decreasing x–axis (p_λ, q_λ) as well as along the y–axis (r_λ, s_λ) respectively. Any light flux entering the infinitesimal

Considering light fluxes only within the medium

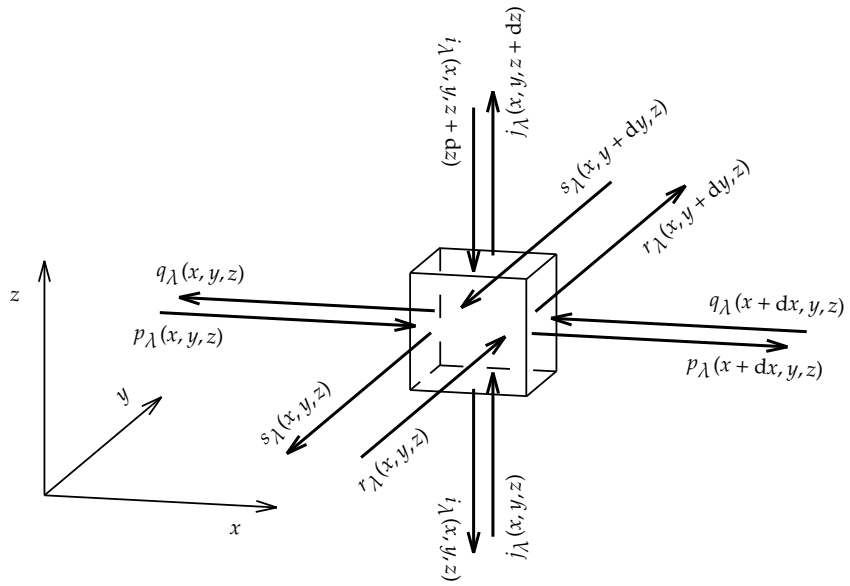

Figure 6.1: Considered optical fluxes in the cartesian coordinate system.

volume cube $\mathrm{d}x\,\mathrm{d}y\,\mathrm{d}z$ from a direction x_1, loses a fractional amount by scattering into a direction x_2 determined by $\sigma_{x_1x_2\,\lambda}\cdot dx\,dy\,dz$. In addition, the light flux loses $\alpha_\lambda\cdot dx\,dy\,dz$ by absorption and $\phi_{e_\lambda}\cdot dx\,dy\,dz$ by brightener excitation. At the same time, it gains a corresponding amount $\sigma_{x_2x_1\,\lambda}\cdot dx\,dy\,dz$ by scattering from direction x_2 and $\phi_{f_\lambda}\cdot dx\,dy\,dz$ by fluorescence from its own flux and from the other fluxes yielding for the case of i_λ

$$\begin{aligned} i_\lambda(x,y,z)\cdot\mathrm{d}x\mathrm{d}y = i_\lambda(x,y,z+\mathrm{d}z)\cdot\mathrm{d}x\mathrm{d}y + \Big[&\left(\phi_{f_\lambda}+\sigma_{ji_\lambda}\right)\cdot j_\lambda(x,y,z) + \\ &\left(\phi_{f_\lambda}-\phi_{e_\lambda}-\alpha_\lambda-\sigma_{ij_\lambda}-\sigma_{ip_\lambda}-\sigma_{iq_\lambda}-\sigma_{ir_\lambda}-\sigma_{is_\lambda}\right)\cdot i_\lambda(x,y,z+\mathrm{d}z) + \\ &\left(\phi_{f_\lambda}+\sigma_{pi_\lambda}\right)\cdot p_\lambda(x,y,z) + \left(\phi_{f_\lambda}+\sigma_{qi_\lambda}\right)\cdot q_\lambda(x+\mathrm{d}x,y,z) + \\ &\left(\phi_{f_\lambda}+\sigma_{ri_\lambda}\right)\cdot r_\lambda(x,y,z) + \left(\phi_{f_\lambda}+\sigma_{si_\lambda}\right)\cdot s_\lambda(x,y+\mathrm{d}y,z)\Big]\cdot\mathrm{d}x\mathrm{d}y\mathrm{d}z\,, \end{aligned} \tag{6.1}$$

where α_λ is the specific spectral absorption coefficient per unit volume. $\sigma_{x_1x_2\,\lambda}$ is the specific spectral scattering coefficient of a ray emerging from direction x_1 and distracted to direction x_2. ϕ_{e_λ} and ϕ_{f_λ} are the normalized excitation and fluorescent spectra respectively. Accordingly the radiant balance of the remaining fluxes are

$$\begin{aligned} j_\lambda(x,y,z+\mathrm{d}z)\cdot\mathrm{d}x\mathrm{d}y = j_\lambda(x,y,z)\cdot\mathrm{d}x\mathrm{d}y + \Big[&\left(\phi_{f_\lambda}+\sigma_{ij_\lambda}\right)\cdot i_\lambda(x,y,z+\mathrm{d}z) + \\ &\left(\phi_{f_\lambda}-\phi_{e_\lambda}-\alpha_\lambda-\sigma_{ji_\lambda}-\sigma_{jp_\lambda}-\sigma_{jq_\lambda}-\sigma_{jr_\lambda}-\sigma_{js_\lambda}\right)\cdot j_\lambda(x,y,z) + \\ &\left(\phi_{f_\lambda}+\sigma_{pj_\lambda}\right)\cdot p_\lambda(x,y,z) + \left(\phi_{f_\lambda}+\sigma_{qj_\lambda}\right)\cdot q_\lambda(x+\mathrm{d}x,y,z) + \\ &\left(\phi_{f_\lambda}+\sigma_{rj_\lambda}\right)\cdot r_\lambda(x,y,z) + \left(\phi_{f_\lambda}+\sigma_{sj_\lambda}\right)\cdot s_\lambda(x,y+\mathrm{d}y,z)\Big]\cdot\mathrm{d}x\mathrm{d}y\mathrm{d}z\,, \end{aligned} \tag{6.2}$$

$$p_\lambda(x+\mathrm{d}x,y,z)\cdot\mathrm{d}y\mathrm{d}z = p_\lambda(x,y,z)\cdot\mathrm{d}y\mathrm{d}z + \Big[\Big(\phi_{f_\lambda}+\sigma_{qp_\lambda}\Big)\cdot q_\lambda(x+\mathrm{d}x,y,z) + \Big(\phi_{f_\lambda}-\phi_{e_\lambda}-\alpha_\lambda-\sigma_{pq_\lambda}-\sigma_{pi_\lambda}-\sigma_{pj_\lambda}-\sigma_{pr_\lambda}-\sigma_{ps_\lambda}\Big)\cdot p_\lambda(x,y,z) + \Big(\phi_{f_\lambda}+\sigma_{ip_\lambda}\Big)\cdot i_\lambda(x,y,z+\mathrm{d}z) + \Big(\phi_{f_\lambda}+\sigma_{jp_\lambda}\Big)\cdot j_\lambda(x,y,z) + \Big(\phi_{f_\lambda}+\sigma_{rp_\lambda}\Big)\cdot r_\lambda(x,y,z) + \Big(\phi_{f_\lambda}+\sigma_{sp_\lambda}\Big)\cdot s_\lambda(x,y+\mathrm{d}y,z)\Big]\cdot\mathrm{d}x\mathrm{d}y\mathrm{d}z\,, \tag{6.3}$$

$$q_\lambda(x,y,z)\cdot\mathrm{d}y\mathrm{d}z = q_\lambda(x+\mathrm{d}x,y,z)\cdot\mathrm{d}y\mathrm{d}z + \Big[\Big(\phi_{f_\lambda}+\sigma_{pq_\lambda}\Big)\cdot p_\lambda(x,y,z) + \Big(\phi_{f_\lambda}-\phi_{e_\lambda}-\alpha_\lambda-\sigma_{qp_\lambda}-\sigma_{qi_\lambda}-\sigma_{qj_\lambda}-\sigma_{qr_\lambda}-\sigma_{qs_\lambda}\Big)\cdot q_\lambda(x+\mathrm{d}x,y,z) + \Big(\phi_{f_\lambda}+\sigma_{iq_\lambda}\Big)\cdot i_\lambda(x,y,z+\mathrm{d}z) + \Big(\phi_{f_\lambda}+\sigma_{jq_\lambda}\Big)\cdot j_\lambda(x,y,z) + \Big(\phi_{f_\lambda}+\sigma_{rq_\lambda}\Big)\cdot r_\lambda(x,y,z) + \Big(\phi_{f_\lambda}+\sigma_{sq_\lambda}\Big)\cdot s_\lambda(x,y+\mathrm{d}y,z)\Big]\cdot\mathrm{d}x\mathrm{d}y\mathrm{d}z\,, \tag{6.4}$$

$$r_\lambda(x,y+\mathrm{d}y,z)\cdot\mathrm{d}x\mathrm{d}z = r_\lambda(x,y,z)\cdot\mathrm{d}x\mathrm{d}z + \Big[\Big(\phi_{f_\lambda}+\sigma_{sr_\lambda}\Big)\cdot s_\lambda(x,y+\mathrm{d}y,z) + \Big(\phi_{f_\lambda}-\phi_{e_\lambda}-\alpha_\lambda-\sigma_{rs_\lambda}-\sigma_{ri_\lambda}-\sigma_{rj_\lambda}-\sigma_{rp_\lambda}-\sigma_{rq_\lambda}\Big)\cdot r_\lambda(x,y,z) + \Big(\phi_{f_\lambda}+\sigma_{ir_\lambda}\Big)\cdot i_\lambda(x,y,z+\mathrm{d}z) + \Big(\phi_{f_\lambda}+\sigma_{jr_\lambda}\Big)\cdot j_\lambda(x,y,z) + \Big(\phi_{f_\lambda}+\sigma_{pr_\lambda}\Big)\cdot p_\lambda(x,y,z) + \Big(\phi_{f_\lambda}+\sigma_{qr_\lambda}\Big)\cdot q_\lambda(x+\mathrm{d}x,y,z)\Big]\cdot\mathrm{d}x\mathrm{d}y\mathrm{d}z\,, \tag{6.5}$$

$$s_\lambda(x,y,z)\cdot\mathrm{d}x\mathrm{d}z = s_\lambda(x,y+\mathrm{d}y,z)\cdot\mathrm{d}x\mathrm{d}z + \Big[\Big(\phi_{f_\lambda}+\sigma_{rs_\lambda}\Big)\cdot r_\lambda(x,y,z) + \Big(\phi_{f_\lambda}-\phi_{e_\lambda}-\alpha_\lambda-\sigma_{sr_\lambda}-\sigma_{si_\lambda}-\sigma_{sj_\lambda}-\sigma_{sp_\lambda}-\sigma_{sq_\lambda}\Big)\cdot s_\lambda(x,y+\mathrm{d}y,z) + \Big(\phi_{f_\lambda}+\sigma_{is_\lambda}\Big)\cdot i_\lambda(x,y,z+\mathrm{d}z) + \Big(\phi_{f_\lambda}+\sigma_{js_\lambda}\Big)\cdot j_\lambda(x,y,z) + \Big(\phi_{f_\lambda}+\sigma_{ps_\lambda}\Big)\cdot p_\lambda(x,y,z) + \Big(\phi_{f_\lambda}+\sigma_{qs_\lambda}\Big)\cdot q_\lambda(x+\mathrm{d}x,y,z)\Big]\cdot\mathrm{d}x\mathrm{d}y\mathrm{d}z\,, \tag{6.6}$$

Usually, the excitation spectrum lies entirely within the invisible frequency band and does not contribute to the visible color appearance of a medium. Therefore, any absorption due to brightener excitation is neglected and hereinafter, ϕ_{e_λ} is set equal to 0.

The balance equations (6.1–6.6) are developed applying a Taylor series expansion to the fluxes at the coordinates $x+\mathrm{d}x$, $y+\mathrm{d}y$ and $z+\mathrm{d}z$ as follows

Taylor series expansion

$$i_\lambda(x,y,z+\mathrm{d}z) = i_\lambda(x,y,z) + \frac{\partial\, i_\lambda(x,y,z)}{\partial z}\cdot\mathrm{d}z + \frac{1}{2}\cdot\frac{\partial^2 i_\lambda(x,y,z)}{\partial z^2}\cdot\mathrm{d}z^2 + \frac{1}{6}\cdot\frac{\partial^3 i_\lambda(x,y,z)}{\partial z^3}\cdot\mathrm{d}z^3 + \cdots\,. \tag{6.7}$$

The higher order terms of the resulting series are neglected by assuming analytical, continuous light fluxes, which vary linearly within smallest volume cubes yielding

$$i_\lambda(x,y,z+\mathrm{d}z) = i_\lambda(x,y,z) + \frac{\partial\, i_\lambda(x,y,z)}{\partial z}\cdot\mathrm{d}z\,. \tag{6.8}$$

Applying equation (6.8) to the flux balance equation (6.1) and neglecting ϕ_{e_λ} as mentioned above yields

$$\begin{aligned} i_\lambda(x,y,z)\cdot \mathrm{d}x\mathrm{d}y = i_\lambda(x,y,z)\cdot \mathrm{d}x\mathrm{d}y + \Bigg[& \frac{\partial\, i_\lambda(x,y,z)}{\partial z} + \left(\phi_{f_\lambda} + \sigma_{ji_\lambda}\right)\cdot j_\lambda(x,y,z) + \\ & \left(\phi_{f_\lambda} - \alpha_\lambda - \sigma_{ij_\lambda} - \sigma_{ip_\lambda} - \sigma_{iq_\lambda} - \sigma_{ir_\lambda} - \sigma_{is_\lambda}\right)\cdot\left(i_\lambda(x,y,z) + \frac{\partial\, i_\lambda(x,y,z)}{\partial z}\cdot \mathrm{d}z\right) + \\ & \left(\phi_{f_\lambda} + \sigma_{pi_\lambda}\right)\cdot p_\lambda(x,y,z) + \left(\phi_{f_\lambda} + \sigma_{qi_\lambda}\right)\cdot\left(q_\lambda(x,y,z) + \frac{\partial\, q_\lambda(x,y,z)}{\partial x}\cdot \mathrm{d}x\right) + \\ & \left(\phi_{f_\lambda} + \sigma_{ri_\lambda}\right)\cdot r_\lambda(x,y,z) + \left(\phi_{f_\lambda} + \sigma_{si_\lambda}\right)\cdot\left(s_\lambda(x,y,z) + \frac{\partial\, s_\lambda(x,y,z)}{\partial y}\cdot \mathrm{d}y\right)\Bigg]\cdot \mathrm{d}x\mathrm{d}y\mathrm{d}z\ . \end{aligned} \tag{6.9}$$

Reducing the analyzed dimensions further yields an infinitesimal cube which makes it possible to ignore any non-linear differentials $\mathrm{d}x^2$, $\mathrm{d}y^2$ and $\mathrm{d}z^2$. This leads to the following system of coupled partial linear differential equations

$$\begin{aligned} \frac{\partial\, i_\lambda(x,y,z)}{\partial z} = & -\left(\phi_{f_\lambda} + \sigma_{ji_\lambda}\right)\cdot j_\lambda(x,y,z) - \\ & \left(\phi_{f_\lambda} - \alpha_\lambda - \sigma_{ij_\lambda} - \sigma_{ip_\lambda} - \sigma_{iq_\lambda} - \sigma_{ir_\lambda} - \sigma_{is_\lambda}\right)\cdot i_\lambda(x,y,z) - \\ & \left(\phi_{f_\lambda} + \sigma_{pi_\lambda}\right)\cdot p_\lambda(x,y,z) - \left(\phi_{f_\lambda} + \sigma_{qi_\lambda}\right)\cdot q_\lambda(x,y,z) - \\ & \left(\phi_{f_\lambda} + \sigma_{ri_\lambda}\right)\cdot r_\lambda(x,y,z) - \left(\phi_{f_\lambda} + \sigma_{si_\lambda}\right)\cdot s_\lambda(x,y,z)\ , \end{aligned} \tag{6.10}$$

$$\begin{aligned} \frac{\partial\, j_\lambda(x,y,z)}{\partial z} = & \left(\phi_{f_\lambda} + \sigma_{ij_\lambda}\right)\cdot i_\lambda(x,y,z) + \\ & \left(\phi_{f_\lambda} - \alpha_\lambda - \sigma_{ji_\lambda} - \sigma_{jp_\lambda} - \sigma_{jq_\lambda} - \sigma_{jr_\lambda} - \sigma_{js_\lambda}\right)\cdot j_\lambda(x,y,z) + \\ & \left(\phi_{f_\lambda} + \sigma_{pj_\lambda}\right)\cdot p_\lambda(x,y,z) + \left(\phi_{f_\lambda} + \sigma_{qj_\lambda}\right)\cdot q_\lambda(x,y,z) + \\ & \left(\phi_{f_\lambda} + \sigma_{rj_\lambda}\right)\cdot r_\lambda(x,y,z) + \left(\phi_{f_\lambda} + \sigma_{sj_\lambda}\right)\cdot s_\lambda(x,y,z)\ , \end{aligned} \tag{6.11}$$

$$\begin{aligned} \frac{\partial\, p_\lambda(x,y,z)}{\partial x} = & \left(\phi_{f_\lambda} + \sigma_{qp_\lambda}\right)\cdot q_\lambda(x,y,z) + \\ & \left(\phi_{f_\lambda} - \alpha_\lambda - \sigma_{pq_\lambda} - \sigma_{pi_\lambda} - \sigma_{pj_\lambda} - \sigma_{pr_\lambda} - \sigma_{ps_\lambda}\right)\cdot p_\lambda(x,y,z) + \\ & \left(\phi_{f_\lambda} + \sigma_{ip_\lambda}\right)\cdot i_\lambda(x,y,z) + \left(\phi_{f_\lambda} + \sigma_{jp_\lambda}\right)\cdot j_\lambda(x,y,z) + \\ & \left(\phi_{f_\lambda} + \sigma_{rp_\lambda}\right)\cdot r_\lambda(x,y,z) + \left(\phi_{f_\lambda} + \sigma_{sp_\lambda}\right)\cdot s_\lambda(x,y,z)\ , \end{aligned} \tag{6.12}$$

$$\begin{aligned} \frac{\partial\, q_\lambda(x,y,z)}{\partial x} = & -\left(\phi_{f_\lambda} + \sigma_{pq_\lambda}\right)\cdot p_\lambda(x,y,z) - \\ & \left(\phi_{f_\lambda} - \alpha_\lambda - \sigma_{qp_\lambda} - \sigma_{qi_\lambda} - \sigma_{qj_\lambda} - \sigma_{qr_\lambda} - \sigma_{qs_\lambda}\right)\cdot q_\lambda(x,y,z) - \\ & \left(\phi_{f_\lambda} + \sigma_{iq_\lambda}\right)\cdot i_\lambda(x,y,z) - \left(\phi_{f_\lambda} + \sigma_{jq_\lambda}\right)\cdot j_\lambda(x,y,z) - \\ & \left(\phi_{f_\lambda} + \sigma_{rq_\lambda}\right)\cdot r_\lambda(x,y,z) - \left(\phi_{f_\lambda} + \sigma_{sq_\lambda}\right)\cdot s_\lambda(x,y,z)\ , \end{aligned} \tag{6.13}$$

$$\begin{aligned}\frac{\partial r_\lambda(x,y,z)}{\partial y} &= \left(\phi_{f_\lambda} + \sigma_{sr_\lambda}\right)\cdot s_\lambda(x,y,z) + \\ &\left(\phi_{f_\lambda} - \alpha_\lambda - \sigma_{rs_\lambda} - \sigma_{ri_\lambda} - \sigma_{rj_\lambda} - \sigma_{rp_\lambda} - \sigma_{rq_\lambda}\right)\cdot r_\lambda(x,y,z) + \\ &\left(\phi_{f_\lambda} + \sigma_{ir_\lambda}\right)\cdot i_\lambda(x,y,z) + \left(\phi_{f_\lambda} + \sigma_{jr_\lambda}\right)\cdot j_\lambda(x,y,z) + \\ &\left(\phi_{f_\lambda} + \sigma_{pr_\lambda}\right)\cdot p_\lambda(x,y,z) + \left(\phi_{f_\lambda} + \sigma_{qr_\lambda}\right)\cdot q_\lambda(x,y,z)\ , \end{aligned} \tag{6.14}$$

$$\begin{aligned}\frac{\partial s_\lambda(x,y,z)}{\partial y} &= -\left(\phi_{f_\lambda} + \sigma_{rs_\lambda}\right)\cdot r_\lambda(x,y,z) - \\ &\left(\phi_{f_\lambda} - \alpha_\lambda - \sigma_{sr_\lambda} - \sigma_{si_\lambda} - \sigma_{sj_\lambda} - \sigma_{sp_\lambda} - \sigma_{sq_\lambda}\right)\cdot s_\lambda(x,y,z) - \\ &\left(\phi_{f_\lambda} + \sigma_{is_\lambda}\right)\cdot i_\lambda(x,y,z) - \left(\phi_{f_\lambda} + \sigma_{js_\lambda}\right)\cdot j_\lambda(x,y,z) - \\ &\left(\phi_{f_\lambda} + \sigma_{ps_\lambda}\right)\cdot p_\lambda(x,y,z) - \left(\phi_{f_\lambda} + \sigma_{qs_\lambda}\right)\cdot q_\lambda(x,y,z)\ . \end{aligned} \tag{6.15}$$

The result is a rather complex system, which cannot be directly solved. In particular, the simultaneous variation in three independent coordinates poses a profound handicap. Nonetheless, pursuing the concept of Berg [Ber97, p. 65], the lateral components $p_\lambda(x,y,z)$, $q_\lambda(x,y,z)$, $r_\lambda(x,y,z)$ and $s_\lambda(x,y,z)$ can be canceled out of the equation system by applying a two-dimensional Fourier transform along the horizontal coordinates x and y.

Semi isotrope scattering

The large number of scattering coefficients induces serious calibration difficulties and must be reduced and simplified further. For this purpose, the *semi isotrope scattering* approach was presented in [MESH01, sec. 5]. The number of considered scattering parameters is reduced to only two distinct coefficients. The *reflecting* parameter σ_{r_λ} accounting for the fraction of light flux being scattered back into the original direction, from which the radiant ray emerged, and the *distracting* parameter σ_{s_λ} representing all other sub-fluxes scattered into any other spatial direction

$$\sigma_{x_\lambda} = \sigma_{r_\lambda} \quad \text{for } x \in \{\, ij \quad ji \quad pq \quad qp \quad rs \quad sr \,\}\ , \tag{6.16}$$

$$\sigma_{x_\lambda} = \sigma_{s_\lambda} \quad \text{for } x \in \begin{Bmatrix} ip & iq & ir & is & jp & jq & jr & js \\ pi & pj & pr & ps & qi & qj & qr & qs \\ ri & rj & rp & rq & si & sj & sp & sq \end{Bmatrix}\ . \tag{6.17}$$

Applying these concepts, the differential equations are simplified and solved in section 6.3 after applying appropriate boundary conditions.

6.2.2 Light scattering in polar coordinates

The spectral measurements of common spectrophotometers are circular symmetric, due to the setup of their illumination and sensing components (section 3.1.1). This makes it possible to further simplify the analysis of the scattering light by choosing a polar coordinate system (r, θ, z) as illustrated in figure 6.2. The resulting radiant balances as well as the derived differential equation system and the

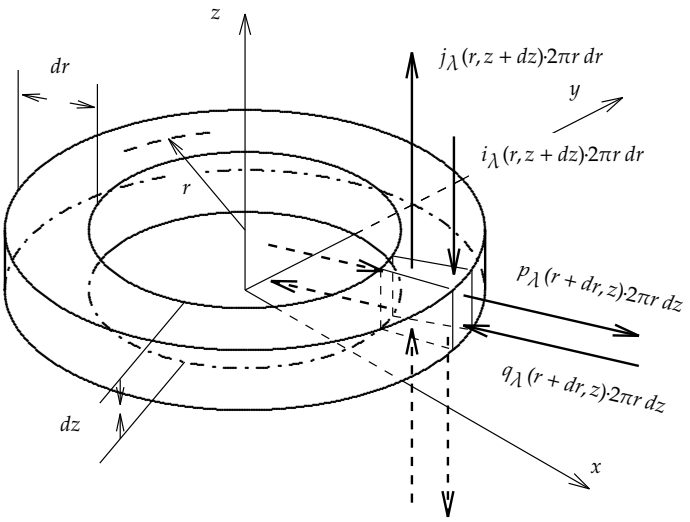

Figure 6.2: Considered optical fluxes in the polar coordinate system.

obtained modulation transfer function are all identical to the cartesian relations derived in section 6.2.1. Only the coefficients are slightly simplified. For simplicity, the presentation of the complete mathematics is described in appendix A.3.

Strictly speaking, the circular approach implies the assumption of a circular symmetrical halftone print. Combined with the reduced dimensionality, this restriction appears unacceptable for color halftone printing. However, substituting $\sqrt{x^2 + y^2}$ for r and ignoring the circular symmetry restriction yields a simplified approach of negligible numerical artifacts as will be presented in section 7.2.4.

6.3 Solving the light scattering model in the cartesian coordinates system

The cartesian light scattering model equations (6.10)–(6.15) are solved by applying a Fourier transformation and boundary conditions as presented in the following subsections.

6.3.1 Simplifying the differential equation system

To model the reflectance or the transmittance of halftone prints, only the vertical fluxes need to be solved. Following the solving concept discussed earlier, the differential equation system (6.10)–(6.15) is transformed by applying a two-dimensional Fourier transform $\mathcal{F}_{x,y}$ on the lateral dimensions x and y [Bra00, p. 330]. The obtained lateral frequencies are χ and ψ. Using the simplifying dif-

ferentiation theorem of the two-dimensional Fourier transform

$$\mathcal{F}_{x,y}\left[\frac{\partial\, g\,(x,y,z)}{\partial\, x}\right] = 2\,\pi\,\mathbf{i}\cdot\chi\cdot\mathcal{G}\,(\chi,\psi,z) \quad \text{and} \tag{6.18}$$

$$\mathcal{F}_{x,y}\left[\frac{\partial\, g\,(x,y,z)}{\partial\, y}\right] = 2\,\pi\,\mathbf{i}\cdot\psi\cdot\mathcal{G}\,(\chi,\psi,z) \tag{6.19}$$

changes the differential nature of the four lateral equations (6.12)–(6.15) to common algebraic equations. $\mathcal{G}$ is the Fourier transform of g and $\mathbf{i}$ is the imaginary constant. Processing the transformed system algebraically with Mathematica® [Wol00] cancels the lateral equations, and the equation systems are reduced to the following perpendicular Fourier transformed differential equations

$$\frac{\partial\,\mathcal{I}_\lambda(\chi,\psi,z)}{\partial\, z} = a_{12_{\chi\psi,\lambda}}\cdot\mathcal{J}_\lambda(\chi,\psi,z) + a_{21_{\chi\psi,\lambda}}\cdot\mathcal{I}_\lambda(\chi,\psi,z)\ , \tag{6.20}$$

$$-\frac{\partial\,\mathcal{J}_\lambda(\chi,\psi,z)}{\partial\, z} = a_{12_{\chi\psi,\lambda}}\cdot\mathcal{I}_\lambda(\chi,\psi,z) + a_{21_{\chi\psi,\lambda}}\cdot\mathcal{J}_\lambda(\chi,\psi,z)\ , \tag{6.21}$$

with $\mathcal{I}_\lambda(\chi,\psi,z)$ and $\mathcal{J}_\lambda(\chi,\psi,z)$ the Fourier transform of the perpendicular fluxes $i_\lambda(x,y,z)$ and $j_\lambda(x,y,z)$. $a_{12_{\chi\psi,\lambda}}$ and $a_{21_{\chi\psi,\lambda}}$ are substitution constants formulated in detail in appendix A.1.

6.3.2 Paper boundary interreflections

The obtained equations (6.20) and (6.21) are only valid within the continuum of the paper body. Therefore, it is important to choose adequate boundary conditions, and special care must be taken with the physical discontinuities of the paper sheet. On the one hand, the boundary conditions strongly affect the model's accuracy and complexity. On the other hand, they bridge the pure mathematics with the measured physics.

General model assumptions

As described in section 3.1.1, the spectral measurements are performed using common spectrophotometers with an approximately circular (45/0°)-illumination. The proposed model analyzes a paper sheet in a *reflectance or transmittance* measurement mode. The paper is placed in both modes on a backing with a known spectral reflectance R_{b_λ}. The paper faces may be covered with a coating layer. Hereinafter, the word *coating* is used as a generic term, which also includes any printed ink layers. The inks are assumed to be *non-fluorescent* and *non-scattering*. For scattering inks, one may consider extending the presented approaches by the extensions proposed by Kubelka [Kub54, eq. (8)+(10)] or more recently by Stollnitz [SOS98, eq. (7)]. Extensions taking into account fluorescent *inks* may rely on the approach of Emmel [EH98, Emm98].

As illustrated in figure 6.3, the proposed model considers *solid* or *halftone* color prints at the front side of the paper and solely *solid prints* at the reverse side of the paper. The analyzed substrates are assumed to have almost the same refractive index as *air*, which is in general agreement with commonly used office papers. For

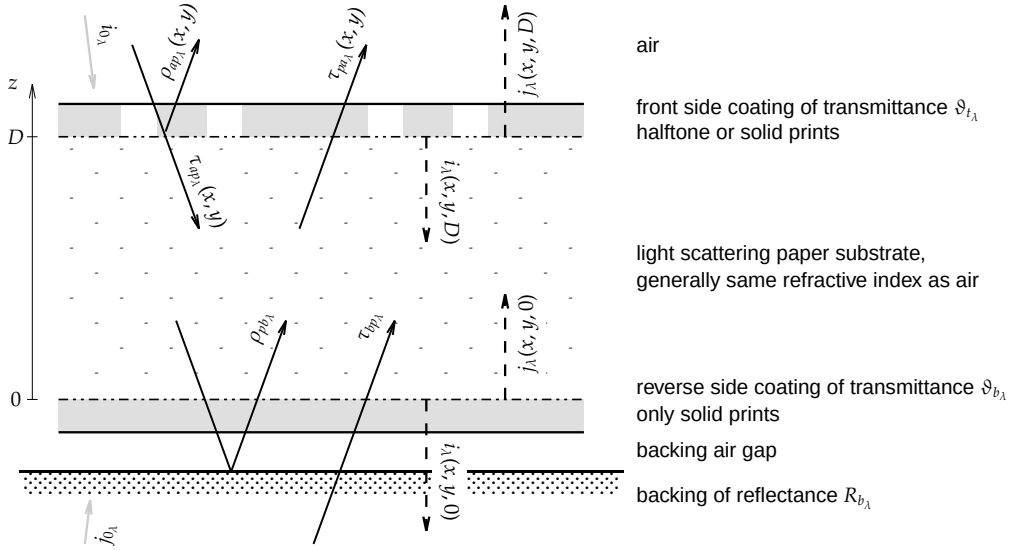

Figure 6.3: Scheme of the considered interreflections at the boundaries of a double side printed paper sheet. The dashed radiant represents the fluxes within the continuum of the paper substrate. i_{0_λ} and j_{0_λ} are the illuminations of a reflectance or transmittance measurement respectively.

high gloss or photo paper alternative considerations are needed and therefore, these papers extend beyond the scope of this thesis.

Considering multiple reflections

Any light flux passing through the coating interfaces is subject to multiple reflections [Tuc47]. Basically, multiple internal reflections (also called *interreflection*) within an optical layer induce a lateral spreading of the light fluxes. However, this lateral spreading is negligible since the coating layers are usually much thinner than a paper thickness. Hence, the considered optical dot gain is assumed to be mainly influenced by the scattered light within the paper bulk. However, multiple reflections also induce an augmentation of the filter density as seen in section 4.1.3. The present model considers these density augmentations by applying adopted Saunderson corrections, see equation (4.12). These corrections take the multiple reflections into account and determine the fraction of light being transmitted through or reflected by the paper interfaces as illustrated in figure 6.3. At the front side these corrections include the directly reflected fraction from the coating ρ_{ap_λ}, the transmitted fraction into the paper bulk τ_{ap_λ} as well as the transmission back from the paper into the air τ_{pa_λ}. At the reverse side, the corrections account for the reflection back into the paper bulk ρ_{pb_λ} and the transmission from the backing into the paper body τ_{bp_λ} for the case of a transmittance measurement. The derivation introduced hereafter is based on the interreflections within a simple optical filter presented in section 4.1.3.

Each printed interface of a paper sheet acts as an independent filter placed in contact with the substrate. In the case under consideration, where the refractive index of paper and air are almost equal, the Fresnel factors at the air and at the substrate interface of the coating layer are assumed to be equal, i.e. $\rho_{i1_\lambda} = \rho_{i2_\lambda} = \rho_{i_\lambda}$ and so forth. In this case, $\tau_{f_{12_\lambda}}$ and $\rho_{f_{12_\lambda}}$ of equations (4.6) and (4.7) become τ_{f_λ}

and ρ_{f_λ} respectively.

To derive the appropriate corrections at the reverse side of the paper, the interreflections within the coating filter as well as within the *backing gap* are considered. The backing gap refers to the air gap between the measured sample and the instrument backing. As depicted in figure 6.4, a part of the radiant reaching

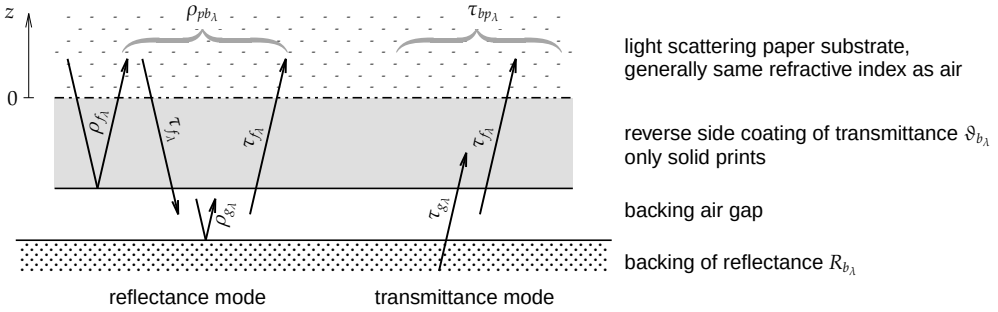

Figure 6.4: An enlarged detail of figure 6.3 showing the considered reflectance and transmittance through the backing air gap.

the bottom face of the substrate is reflected at the reverse side coating directly into the paper by ρ_{f_λ}. Another part τ_{f_λ} is transmitted through the coating into the backing gap. In this gap, additional interreflections ρ_{g_λ} occur, which are illustrated in figure 6.5. As the Fresnel transmittance τ_{s_λ} at the coating inferior surface is already considered in τ_{f_λ} eq. (4.6), the resulting backing air gap reflectance ρ_{g_λ} needs only to consider the rays just before they enter the coating. The reflectance at the backing air gap is given by the infinitive sum

Backing gap reflectance

$$\begin{aligned}\rho_{g_\lambda} &= R_{b_\lambda} + \rho_{s_\lambda} \cdot R_{b_\lambda}^2 + \rho_{s_\lambda}^2 \cdot R_{b_\lambda}^3 + \cdots \\ &= \frac{R_{b_\lambda}}{1 - \rho_{s_\lambda} \cdot R_{b_\lambda}} \,. \end{aligned} \tag{6.22}$$

After being reflected at this gap, the flux transmits again into the paper substrate through the coating layer τ_{f_λ}. According to figure 6.4, the total reflection at the

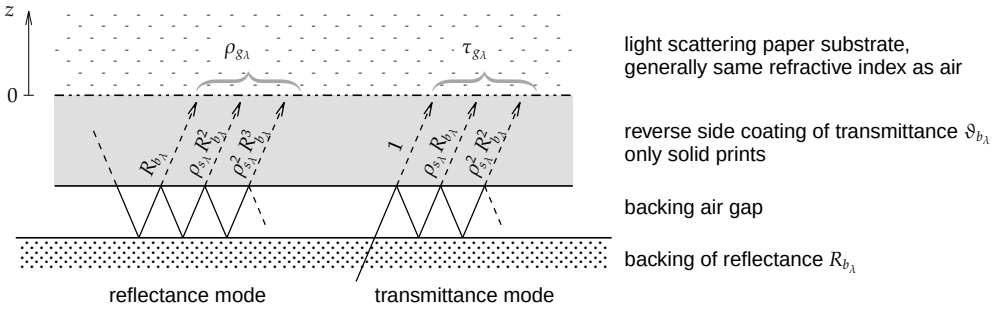

Figure 6.5: Scheme of the considered interreflections within the backing air gap.

backing interface given by ρ_{pb_λ} is composed by one part reflected at the bottom of the reverse side coating and another part reflected from the backing across the

reverse side coating. Using equations (4.6) and (4.7) one obtains

$$\rho_{pb_\lambda} = \rho_{f_\lambda} + \tau_{f_\lambda} \cdot \rho_{g_\lambda} \cdot \tau_{f_\lambda} = \rho_{s_\lambda} + \tau_{s_\lambda} \cdot \tau_{i_\lambda} \cdot \frac{\rho_{i_\lambda} \cdot \vartheta_{b_\lambda}^2}{1 - \rho_{i_\lambda}^2 \cdot \vartheta_{b_\lambda}^2} + \left(\tau_{s_\lambda} \cdot \tau_{i_\lambda} \cdot \frac{\vartheta_{b_\lambda}}{1 - \rho_{i_\lambda}^2 \cdot \vartheta_{b_\lambda}^2} \right)^2 \cdot \frac{R_{b_\lambda}}{1 - \rho_{s_\lambda} \cdot R_{b_\lambda}} . \quad (6.23)$$

paper–backing

where ϑ_{b_λ} is the internal spectral transmittance of the paper reverse side coating and is generally equal to 1. In the case of a solid printed reverse side ϑ_{b_λ} is replaced by the spectral transmittance of the ink layer.

In a transmittance mode, commonly used measurement instruments illuminate the sample through a white, diffusely transparent plate that has a reflectance R_{b_λ}. In this setup, the paper sheet is illuminated from the bottom of the instrument through the backing gap and the coating. Based on figure 6.5 the radiant part τ_{g_λ} transmitted into the substrate is derived similarly to ρ_{g_λ}

$$\tau_{g_\lambda} = 1 + \rho_{s_\lambda} \cdot R_{b_\lambda} + \rho_{s_\lambda}^2 \cdot R_{b_\lambda}^2 + \cdots = \frac{1}{1 - \rho_{s_\lambda} \cdot R_{b_\lambda}} . \quad (6.24)$$

Backing gap transmittance

Given this transmittance and τ_{f_λ} of the coating, the emerging flux τ_{bp_λ} into the paper substrate through the backing is derived according to figure 6.4

$$\tau_{bp_\lambda} = \tau_{g_\lambda} \cdot \tau_{f_\lambda} = \tau_{s_\lambda} \cdot \tau_{i_\lambda} \cdot \frac{\vartheta_{b_\lambda}}{1 - \rho_{i_\lambda}^2 \cdot \vartheta_{b_\lambda}^2} \cdot \frac{1}{1 - \rho_{s_\lambda} \cdot R_{b_\lambda}} . \quad (6.25)$$

backing–paper

As opposed to the bottom side, the present concept supports halftone prints at the front side of the paper. Hence, the considered multiple reflections at the front side coating of the paper have to keep track of the incident flux position (x, y). In this context, $\tau_{ap_\lambda}(x, y)$ describes the fraction of light transmitted from the top through the front side coating layer into the paper substrate and is directly given by equation (4.6)

$$\tau_{ap_\lambda}(x, y) = \tau_{f_\lambda}(x, y) = \tau_{s_\lambda}(x, y) \cdot \tau_{i_\lambda}(x, y) \cdot \frac{\vartheta_{t_\lambda}(x, y)}{1 - \rho_{i_\lambda}^2(x, y) \cdot \vartheta_{t_\lambda}^2(x, y)} , \quad (6.26)$$

air–paper

with $\vartheta_{t_\lambda}(x, y)$ the internal spectral point transmittance of the front side halftoned layer. The fraction of light transmitted from inside the paper into the air is correspondingly given by $\tau_{pa_\lambda}(x, y)$, which is identical to $\tau_{ap_\lambda}(x, y)$.

paper–air

Finally, another part $\rho_{ap_\lambda}(x, y)$ of the surface reflection contributes to a reflectance measurement. It is induced by the interreflections at the front side coating and equals the reflectance of a filter immersed in air according to equation (4.7)

$$\rho_{ap_\lambda}(x, y) = \rho_{f_\lambda}(x, y) = \rho_{s_\lambda}(x, y) + \tau_{s_\lambda}(x, y) \cdot \tau_{i_\lambda}(x, y) \cdot \frac{\rho_{i_\lambda}(x, y) \cdot \vartheta_{t_\lambda}^2(x, y)}{1 - \rho_{i_\lambda}^2(x, y) \cdot \vartheta_{t_\lambda}^2(x, y)} . \quad (6.27)$$

air–paper

6.3.3 Boundary condition problem

The presented multiple reflections within the coatings and at the backing air gap lead to a complete set of boundary conditions for the obtained differential equation system of section 6.2.1. The corrections relate the radiant fluxes at the inner edges of the light scattering medium with the fluxes outside the paper sheet. In this section, these corrections are used to connect the illuminating fluxes at the outside of a paper sheet with the differential equations valid inside its scattering substrate.

As briefly introduced in section 3.1.1, in a reflectance measurement setup, the sample is illuminated in a circular fashion from the top with the collimated flux i_{0_λ}. In a transmittance measurement, the sample is illuminated from beneath the backing with the flux j_{0_λ}. Both fluxes are depicted in figure 6.3. Using a calibrated reflectance and transmittance instrument, the proposed model distinguishes the illuminations by setting either i_{0_λ} or j_{0_λ} to 1 and the other to 0.

Illumination modeling

At the front side of the paper bulk with a total thickness D, directly beneath the coating, the illumination is transmitted through the front side coating $\tau_{ap_\lambda}(x, y)$ yielding

$$i_\lambda(x, y, D) = \tau_{ap_\lambda}(x, y) \cdot i_{0_\lambda} \ . \tag{6.28}$$

Top interface

Equation (6.28) corresponds to the subtractive color mixing introduced in section 5.1 assuming a non-scattering coating layer. After entering the paper bulk, the incident light becomes almost perfectly diffused. Reaching the bottom side of the substrate, the light flux is reflected diffusely by the backing. Mathematically, this is represented by a two-dimensional convolution symbolized by the convolution operator "$**$" [Bra00, p. 331]. In addition to the diffusely reflected flux, in case of a transmittance measurement, the incident light flux at the bottom side of the substrate also comprises the transmitted incident illumination j_{0_λ}

Bottom interface

$$j_\lambda(x, y, 0) = \rho_{pb_\lambda} ** i_\lambda(x, y, 0) + \tau_{bp_\lambda} \cdot j_{0_\lambda} \ . \tag{6.29}$$

Measurement modeling

Before being measured by a spectrophotometer, the upward light flux emerging from the scattering medium is transmitted diffusely again through the top coating layer by $\tau_{pa_\lambda}(x, y)$. Applying the appropriate corrections, the boundary condition of the spectral transmittance measurement estimate of a paper sheet is then given by

$$\hat{T}_\lambda(x, y) = \tau_{pa_\lambda}(x, y) ** j_\lambda(x, y, z) \Big|_{z=D,\, i_{0_\lambda}=0,\, j_{0_\lambda}=1} \ . \tag{6.30}$$

Accordingly, taking into account the surface reflection $\rho_{ap_\lambda}(x, y)$, the spectral reflectance measurement estimate is given by

$$\hat{R}_\lambda(x, y) = \rho_{ap_\lambda}(x, y) + \tau_{pa_\lambda}(x, y) ** j_\lambda(x, y, z) \Big|_{z=D,\, i_{0_\lambda}=1,\, j_{0_\lambda}=0} \ . \tag{6.31}$$

Paper's PSF

The equations (6.30) and (6.31) indicate the use of $j_\lambda(x, y, z)$ as the *point spread function* at any depth z of the paper.

6.3.4 The solution; the paper's modulation transfer function

The derived differential equation system is identical to the original equation system (4.8)–(4.9) of Kubelka–Munk. Hence, the obtained solutions of the boundary condition problem eq. (6.30)–(6.31) and (6.20)–(6.21) are also the same as the exponential solution of Kubelka–Munk given in equation (4.11).

$$\hat{T}_\lambda(x,y) = \tau_{bp_\lambda} \cdot \mathcal{F}_{x,y}^{-1}\Bigg[\mathcal{F}_{x,y}\left[\tau_{pa_\lambda}(x,y)\right] \times \frac{2 \cdot c_{\chi\psi,\lambda} \cdot e^{D\, c_{\chi\psi,\lambda}}}{c_{\chi\psi,\lambda} - a_{21_{\chi\psi,\lambda}} - a_{12_{\chi\psi,\lambda}} \cdot \rho_{pb_\lambda} + \left(c_{\chi\psi,\lambda} + a_{21_{\chi\psi,\lambda}} + a_{12_{\chi\psi,\lambda}} \cdot \rho_{pb_\lambda}\right) \cdot e^{2D\, c_{\chi\psi,\lambda}}} \Bigg], \tag{6.32}$$

Transmittance MTF

$$\hat{R}_\lambda(x,y) = \rho_{ap_\lambda}(x,y) + \tau_{ap_\lambda}(x,y) \cdot \mathcal{F}_{x,y}^{-1}\Bigg[\mathcal{F}_{x,y}\left[\tau_{pa_\lambda}(x,y)\right] \times \frac{a_{12_{\chi\psi,\lambda}} + \left(c_{\chi\psi,\lambda} + a_{21_{\chi\psi,\lambda}}\right) \cdot \rho_{pb_\lambda} + \left(-a_{12_{\chi\psi,\lambda}} + \left(c_{\chi\psi,\lambda} - a_{21_{\chi\psi,\lambda}}\right) \cdot \rho_{pb_\lambda}\right) \cdot e^{2D\, c_{\chi\psi,\lambda}}}{c_{\chi\psi,\lambda} - a_{21_{\chi\psi,\lambda}} - a_{12_{\chi\psi,\lambda}} \cdot \rho_{pb_\lambda} + \left(c_{\chi\psi,\lambda} + a_{21_{\chi\psi,\lambda}} + a_{12_{\chi\psi,\lambda}} \cdot \rho_{pb_\lambda}\right) \cdot e^{2D\, c_{\chi\psi,\lambda}}} \Bigg], \tag{6.33}$$

Reflectance MTF

where D is the thickness of the paper. The derivation of the given solution is given in detail in appendix A.2. $c_{\chi\psi,\lambda}$, $a_{12_{\chi\psi,\lambda}}$ and $a_{21_{\chi\psi,\lambda}}$ are substitution coefficients given explicitly in appendix A.1.

The obtained solution is rather involved and prevents a feasible inverse analytical Fourier transformation. However, it is well suited for numerical transformation by an inverse two-dimensional fast Fourier transform (FFT) [Bra00]. Actually, the fractions in the second line of eq. (6.32) and (6.33) respectively describe the mathematically derived *modulation transfer function (MTF)* of the paper in both a transmittance as well as a reflectance consideration. In this respect, the obtained general solution given in equation (A.30) represents an analytically derived form of the point reflection model established by Ruckdeschel and Hauser in [RH78, eq. 7]. Combined with the interreflection correction terms ρ_{ap_λ}, τ_{ap_λ}, τ_{pa_λ}, ρ_{pb_λ} and τ_{bp_λ}, the solution also accounts for the multiple reflections occurring within the coatings at both sides of the paper for reflectance or transmittance considerations. Corresponding numerical calibration and evaluations are presented in chapter 7.

6.4 Fluorescence versus scattering

The additive relationship of the scattering and fluorescence coefficients in the differential equations (6.10)–(6.15), and their simultaneous appearance as factors for every flux emphasize the considered diffuse nature of the fluorescent spectrum ϕ_{f_λ}. The additive effect of the coefficients remains coupled, and the individual contributions of the parameters σ_λ and ϕ_{f_λ} cannot be separated while measuring a bare unprinted paper with a general illumination setup. Chapter 7 proposes a

complete identification approach of the individual coefficients using the dependency of the fluorescent intensity upon the illumination spectrum.

6.5 Discussion and limitations

This chapter presented two paper modulation transfer functions derived mathematically. They describe the amount of the scattered light radiant being transmitted through or reflected back from the paper bulk at any given position away from its entry point. As introduced in section 6.3.2, the established boundary conditions problem assumes *non-scattering, non-fluorescent* and *non-penetrating* inks. The last-mentioned restriction is largely met by electrophotographic color printers where colored toner particles are deposited on the printing substrate without penetrating the substrate. Finally, with an appropriate adaption of the boundary conditions, the given concept is generally extendible to other paper substrates or to different light scattering media such as human tissues, fog or cloud layers within the atmosphere.

7 Calibrating the light scattering model

The derived paper modulation transfer functions of the last chapter are well suited to fast numerical evaluations by applying two-dimensional FFT transformations. Based on fundamental measurements, this chapter introduces a calibration concept of the related optical parameters of the paper and of its surface. The calibration employs reflectance and transmittance measurements of solid patches only. Then, the calibrated model is compared with microscopic spectral measurements of a particular ink arrangement. Finally, it presents numerical model evaluations of different halftone print samples illustrating the effect of the optical dot gain.

7.1 Calibration considerations

The Kubelka–Munk theory is a phenomenological theory and is highly dependent on the particular measurement arrangement [GB80, p. 325]. Without taking supporting measures, the theory is moderately reliable, due to the measurement noise as shown by Berg in [Ber97, sec. 5.1.4].

Another handicap arises from the inaccessibility by means of physical measurement. The introduced spectral paper parameters such as light absorption and scattering cannot be measured directly. The only conceivable alternative is to estimate the considered parameters numerically. This is performed by fitting the model to spectral measurements of predefined *calibration samples*, which consist of the spectra of printed primary inks as well as of the bare paper-white.

Physical inaccessibility

This section addresses the practical calibration aspects of the paper model and presents the measures undertaken in order to ensure a certain reliability of the fitted unknown parameters.

7.1.1 Calibrating with solid patches

Given the internal spectral point transmittance of a printed halftone $\vartheta_{t_\lambda}(x, y)$, both modulation transfer functions (MTF) introduced in section 6.3.4 calculate the expected spectral point transmittance and reflectance spectra. These MTFs account broadly for the effect of the optical dot gain induced by the paper under consideration. The optical dot gain generally results in darker reproductions and only vanishes if no ink is applied or if a full area coverage is printed, i.e. a solid print [RH78]. The reflectance measurement of a solid patch is not affected by the optical dot gain. Additionally, the reproduction of solid patches is not as much

Solid patches are dot gain free

affected by the printing system's non-linearities as by medium level halftones. Therefore, the most promising approach to follow is to calibrate the model based on reflectance and transmittance measurements of primary color solid patches.

Printing solid patches of primary colors with an almost uniform transmittance ϑ_{t_λ} makes it possible to simplify the model coefficients by applying the singular Fourier transform of a constant k

$$\mathcal{F}_{x,y}[k] = k \cdot \delta(\chi, \psi) \ , \qquad \text{where} \tag{7.1}$$

$$\delta(\chi, \psi) = \begin{cases} 1 & (\chi, \psi) \equiv (0,0) \ , \\ 0 & \text{otherwise} \ . \end{cases}$$

$\delta(\chi, \psi)$ is the two dimensional Dirac impulse symbol, [Bra00, ch. 5]. The resulting simplified MTF coefficients $c_{00,\lambda}$, $t_{00,\lambda}$, $r_{1\cdots3_{00,\lambda}}$ and $d_{1\cdots3_{00,\lambda}}$ are given in appendix A.1.1.

Optimization problem

Applying the simplified coefficient set to the model eq. (6.32)–(6.33), the unknown parameters are identified using constrained nonlinear curve fitting algorithms implemented in Matlab™[Mat01]. They solve the coefficient fitting problem in a least squares sense. Given the measured spectra of the calibration samples, the algorithms find the parameter set that best fits the computed result of the particular nonlinear model (see section 7.2.2).

7.1.2 Applying redundant measurement geometries

In order to improve the estimation reliability of the model parameters, an over-determined set of redundant measurements is used. The over determination is

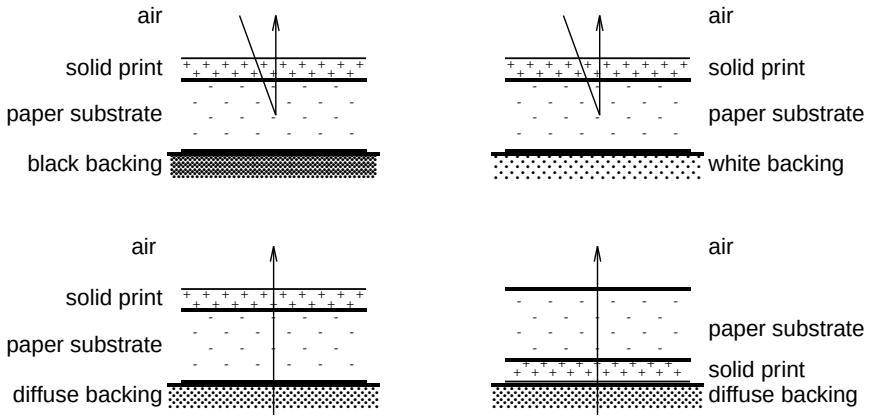

Figure 7.1: Enhancing the calibration reliability with four redundant measurements of a single-side printed paper. *Upper left*: Spectral reflectance of a paper sheet placed on a black backing. *Upper right*: Spectral reflectance factor on a white backing. *Lower left*: Regular spectral transmittance. *Lower right*: Flipped spectral transmittance.

accomplished by varying the geometric measurement setup of the calibration samples introduced above, i.e. the spectra of all printer primary inks as well as

the spectrum of the bare paper-white. Generally, using a reflectance/transmittance spectrophotometer makes it possible to acquire the measurements in four different geometric arrangements. As illustrated in the upper row of figure 7.1, two of the arrangements are the measurements of the spectral reflectance with a black or white backing. The remaining two arrangements in the lower row are the acquisition of the spectral transmittance where the printed paper side is put once facing the sensor and once flipped towards the illumination side of the spectrophotometer.

Observing inner paper parameters

Varying the backing in reflectance measurements influences the amount of reflected light from beneath the sample and helps to determine its translucency. On the other hand, altering the illuminated side of the paper in a transmittance measurement varies the illumination primary path length through the uppermost layers and helps in determining the inner transmittance spectra of the printed layers.

With the introduced interreflection corrections of section 6.3.2, the numerical model supports all the proposed redundant arrangements and accounts for the considered physical effects. When evaluating the model to fit the different measurements, none of the inner optical parameters of the paper needs to be changed. The variation of the measurement arrangements is only taken into account by changing the specific optical layer constants in the mentioned interreflection equations (6.23)–(6.27). The only exception is the fluorescence spectrum, which is treated separately in section 7.1.3.

7.1.3 Calibrating the model for brightened papers

A printed ink layer on a brightened paper behaves like a spectral illumination filter placed at the illumination side of the spectrophotometer. Therefore, varying the measurement arrangements as proposed in the past section also changes the excitation spectra of the brighteners and helps to determine their fluorescent spectrum (see section 6.1.1). According to the theory, altering the excitation energy does not change the general shape of the fluorescent spectrum ϕ_{f_λ} but only its intensity [Emm98, sec. 3.6]. This results in a proportional intensity derogation, which can be considered with a single, *non wavelength-dependent* diminishing constant factor, the *print excitation barrier* $\delta\phi_{f\,print}(x, y)$ multiplied with the fluorescent spectrum ϕ_{f_λ} [MESH01]. $\delta\phi_{f\,print}(x, y)$ keeps track of the spatial position (x, y) because it is dependent on the print, which may be a halftone patch.

Print excitation barrier

Common reflectance/transmittance spectrophotometers have two different light sources built-in, one for the reflectance and one for the transmittance measurements. Hypothetically, they may not be completely adjusted in the higher frequency band and therefore stimulate brightening fluorescent spectra of different intensities. Strictly speaking, the different white and black backings of the reflectance measurements induce a similar but less pronounced effect. This is due to their general unequal reflectance distributions in the upper frequency band.

Further illumination corrections

These mis-adjustments make it difficult to predict the parameter of brightened papers accurately. In order to consider both mis-adjustments numerically, two additional *non wavelength-dependent* adjusting factors are introduced. The *illumination adjustment* $\delta\phi_{f\ illum}$, which accounts for the different excitations induced by the different spectrophotometer light sources, and the *backing adjustment* $\delta\phi_{f\ bck}$, which allows for the different reflectances of the upper frequency bands of the applied backing. Depending on the particular measurement arrangement, the correcting multiplication term $\delta\phi_{f\ \ldots} \cdot \phi_{f_\lambda}$ is substituted for the fluorescent spectrum ϕ_{f_λ} in the coefficient set given in appendix A.1 or A.1.1.

7.2 Measurements and calibration results

All the assumptions are generally based on a series of detailed measurements with different instruments. This section reviews the most relevant measurements and presents a microscopic qualitative model verification.

7.2.1 Bispectral fluorescence measurements of brightened paper

The color of brightened office papers depends upon the intensity and spectral distribution of the illumination under which the paper is viewed, and the way the material interacts with that illumination [Spr97]. Basically, the spectral radiant

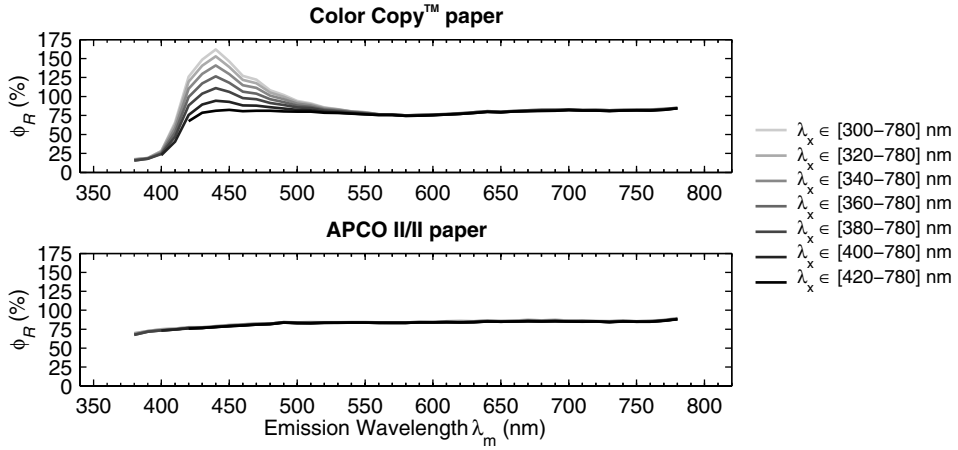

Figure 7.2: Comparison of measured spectral total radiance factors of two different papers. Besides the intensity values reaching more than 100 %, the spectra plotted in the upper graph also demonstrate the impact of varying the illumination spectrum λ_x on the fluorescent spectrum ϕ_{f_λ} of a brightened paper.

distribution of brightened papers measured using common (45/0°) spectrophotometers is more than a simple reflectance. In this case, the instrument registers the *total radiance factor* $\phi_{\mathcal{R}_\lambda}$, which is composed of the reflected component ϕ_{r_λ} and the fluorescent component ϕ_{f_λ} [EH98]

$$\phi_{\mathcal{R}_\lambda} = \phi_{r_\lambda} + \phi_{f_\lambda} \ . \tag{7.2}$$

To separate these components, a *bispectral measurement* is applied, which incorporates two distinct monochromators (see section 3.1.1). One monochromator is

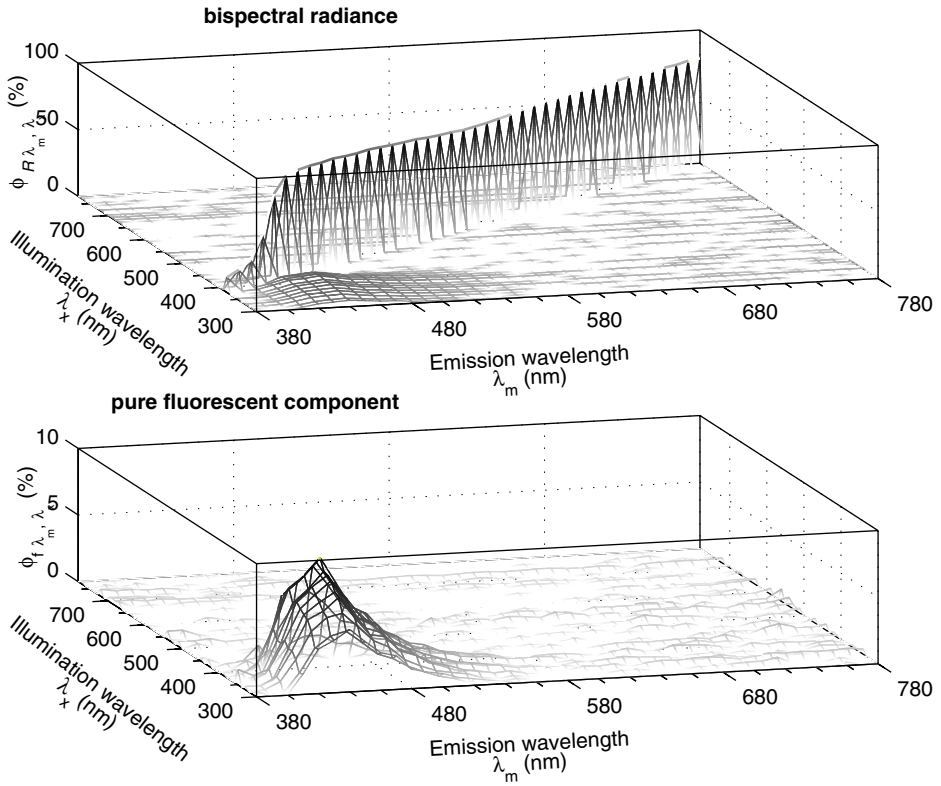

Figure 7.3: Bispectral radiance matrix of the brightened ColorCopy™paper. The lower graph illustrates the pure fluorescent component ϕ_{f_λ} extracted as a detail out of $\phi_{\mathcal{R}_\lambda}$, which is shown in the upper graph.

located between the illumination and the sample in order to separate the *illuminating* radiation ϕ_{λ_x}—also called the *excitation*—into its spectral components before it reaches the sample. The other monochromator, located between the sample and the photodetector array, separates the *emission* radiation ϕ_{λ_m} reflected from the sample surface into its spectral components [GF00]. The separated spectral data are organized in a matrix called the *bispectral radiance matrix* $\phi_{\mathcal{R}_{\lambda_m,\lambda_x}}$ containing all the separate contributions of the illumination wavelength λ_x according to the emission wavelength λ_m. Figure 7.2 illustrates a common reflectance measurement of both a brightened office *ColorCopy*™ paper [Neu00], and a non-brightened standardized *APCO II/II* paper [ISO97]. The figure also demonstrates the effect of varying the illumination wavelength range λ_x on the intensity of the fluorescent spectrum ϕ_{f_λ}. The corresponding variation of the contributing illumination flux is considered by the illumination adjustment $\delta\phi_{f\ illum}$ and the backing adjustment $\delta\phi_{f\ bck}$ introduced in section 7.1.3.

In contrast to the common spectral reflectance measurements introduced in section 3.1.1, the bispectral radiance matrix measurement is truly illumination-independent. In addition, given a bispectral radiance matrix $\phi_{\mathcal{R}_{\lambda_m,\lambda_x}}$, the fluores-

Measuring the fluorescent spectrum

cent emission spectrum ϕ_{f_λ} is determined by the sum of the total illuminating wavelength λ_x after suppressing the pure reflectance spectrum ϕ_{r_λ} from the diagonal of the matrix. Figure 7.3 shows a corresponding graphical representation of the radiance matrix and illustrates a comparison with the isolated fluorescence of the brightened office paper. The measurements were performed with a *BFC-450* manufactured by *Labsphere®*. Finally, figure 7.4 shows the effect of the print

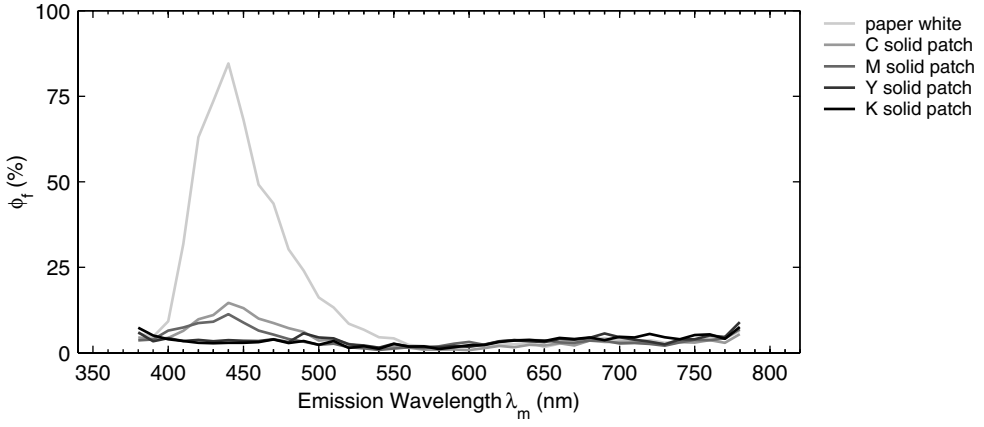

Figure 7.4: Separated fluorescent spectra ϕ_{f_λ} of the brightened office paper printed with different solid patches. According to the theory, its general shape remains unchanged and the intensity of the spectrum diminishes according to the color of the printed solid patches.

excitation barrier taken into account by $\delta\phi_{f\,print}(x, y)$. The figure demonstrates how solid color patches printed at the front side may reduce the intensity of the fluorescent spectrum ϕ_{f_λ} according to their spectral absorptance distribution in the upper frequency band.

7.2.2 Calibration results of a brightened paper

In order to obtain accurate spectral predictions, the light scattering model parameters and the excitation correcting factors need to be estimated for each paper/printer combination. Generally, the model parameters are fitted by calculating the spectral predictions and minimizing their deviation from the measured spectra by constrained non-linear optimization routines of Matlab™[Mat01]. The calibration is performed by presenting all the measured spectra of the calibration samples introduced in section 7.1 simultaneously as an optimization goal to the optimization routine. Specifying reasonable algorithm constraints ensures a physically relevant estimation range of the involved factors and parameters. The optimization of a complete parameter set takes about an hour on a contemporary computer system.

Figure 7.5 illustrates the reflectance and transmittance spectra of the calibration samples measured using a common spectrophotometer such as the *Gretag-Macbeth™ SpectroScan T*. Combined with the measurements, the figure also depicts

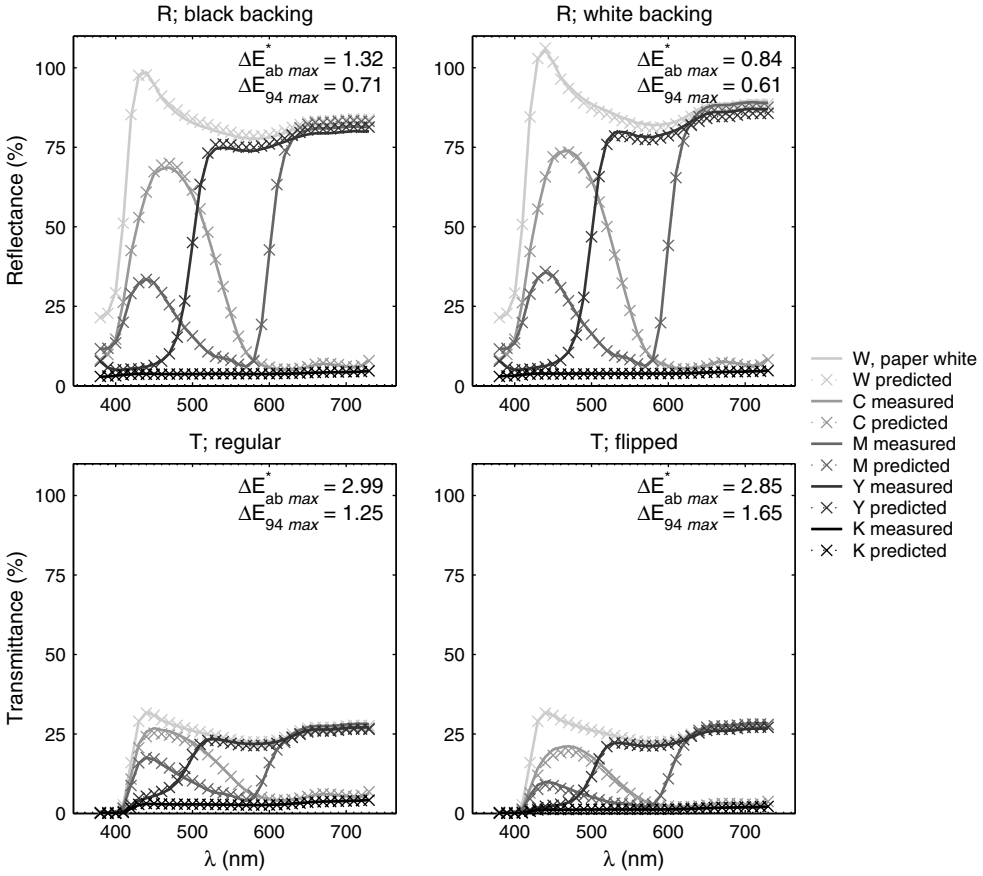

Figure 7.5: Optimization performance of the light scattering model using a measured fluorescent spectrum ϕ_{f_λ}.

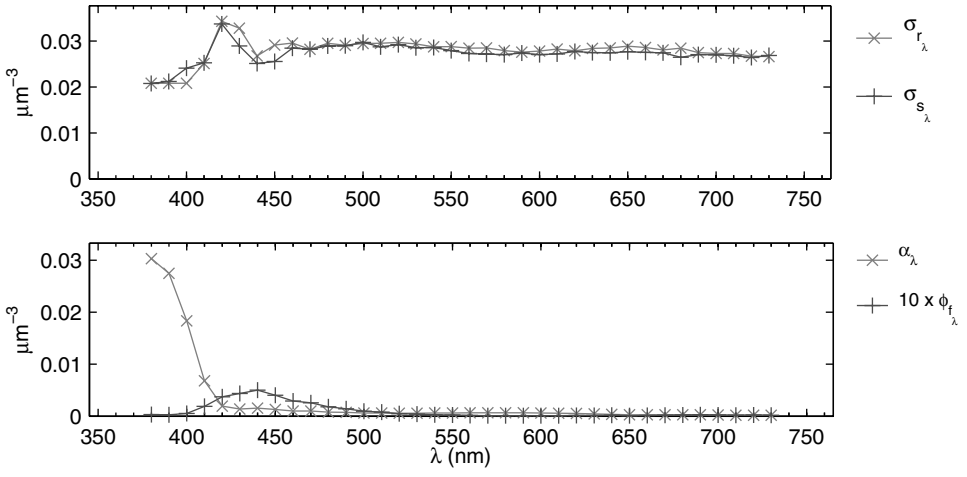

Figure 7.6: Obtained estimates of the spectral parameters σ_{s_λ}, σ_{r_λ}, α_λ and ϕ_{f_λ}.

the optimization results obtained by estimating all the optical coefficients simultaneously except the fluorescent spectrum ϕ_{f_λ}, which was measured bispectrally

as illustrated in figure 7.4. The optimization cannot guarantee the correctness of the estimated model coefficients. Nonetheless, the obtained accuracy of a maximal root mean square spectral (*RMS*) error of less than 0.88 % demonstrates the effectiveness of the proposed concept for the simultaneous consideration of the various geometrical setups. Figure 7.6 plots the obtained spectral estimates of the scattering σ_λ and absorption α_λ coefficients as well as the normalized fluorescent spectrum ϕ_{f_λ}. The average estimates of the Fresnel factors are

$$\rho_s = 2.7\%\,, \qquad \tau_s = 99\%\,, \qquad \rho_i = 2\% \qquad \text{and} \qquad \tau_i = 98\%.$$

Finally, the fluorescent spectrum may be predicted if the measurement equipment is unavailable. A corresponding experiment with the same calibration set yielded an *RMS* of about 1 % and a slightly increased colorimetric deviation.

7.2.3 Model verification with micro line prints

As long as the light scattering model is applied only to estimate the reflectance and transmittance spectra of simple solid patches, there may be no need for any additional reliability proof of the estimated coefficients. However, to use the model for the prediction of halftone prints, an additional independent confirmation experiment is needed.

Due to the scattering light, the spectral reflectance of the paper-white is affected by ink dots printed within the considered direct neighborhood [Eng99, a.o.]. In order to analyze the micro reflectance of the bare paper, a series of micro-spectral scans of the test strip shown in figure 7.7 were performed. The sample

Figure 7.7: Test strip with a series of white micro-lines spared out of a magenta solid patch. The line thickness ranges between $100\,\mu m$ and $1\,mm$.

was scanned vertically using a servo scanning board under a *DMR X* microscope combined with a *MPV SP Leica*™ micro-spectrophotometer. The spatial scanning step size is $10\,\mu m$, and the dimension of the scanning aperture in the object plane is $8\,\mu m$ vertically and $20\,\mu m$ horizontally, i.e the aperture is oriented parallel to the micro-lines. The objective is a semi-apochromat with a wide field of optical performance well suited for photomicrography. It has a 50× magnification and a numerical aperture of 0.85. The analyzed test strip was gravure printed on a white non-brightened paper and illuminated under the microscope with a circular 45/0° arrangement.

Micro-spectral measurements are generally subject to interreflections on the various fibers and the ink/coating interfaces. The localized interreflections induce noisy reflectance scans that inhibit an absolute numerical microscopic verification. Nevertheless, the obtained scans agree qualitatively with the proposed model for each line thickness.

With an appropriate specification of the boundary interreflection equations (6.26)–(6.27), the same micro-spectral scans were simulated applying equation (6.33). Given two fixed wavelengths $\lambda = 530$ and $650\,nm$, figure 7.8 illustrates a

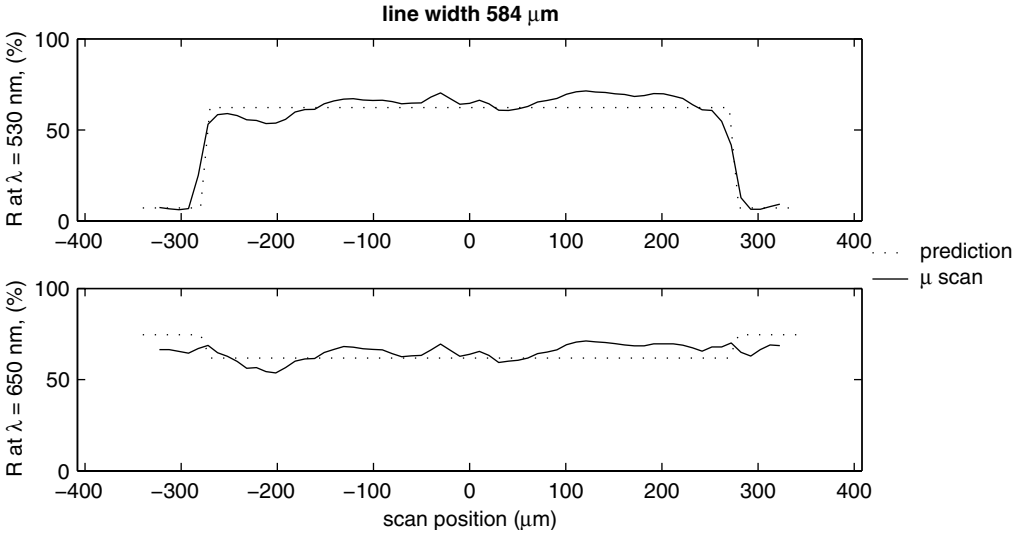

Figure 7.8: Micro-prediction comparison at fixed wavelengths of a $0.6\,mm$ micro-line.

comparison of a spectral scan of the $0.6\,mm$ micro-line with the corresponding prediction calculated by the appropriately calibrated model. In this graph, the consistent behavior at the edges is of particular interest. In fact, the weaker steepness of the measured reflectance at the edges is due to the mechanical dot gain of the gravure print, which was not considered by the simulation.

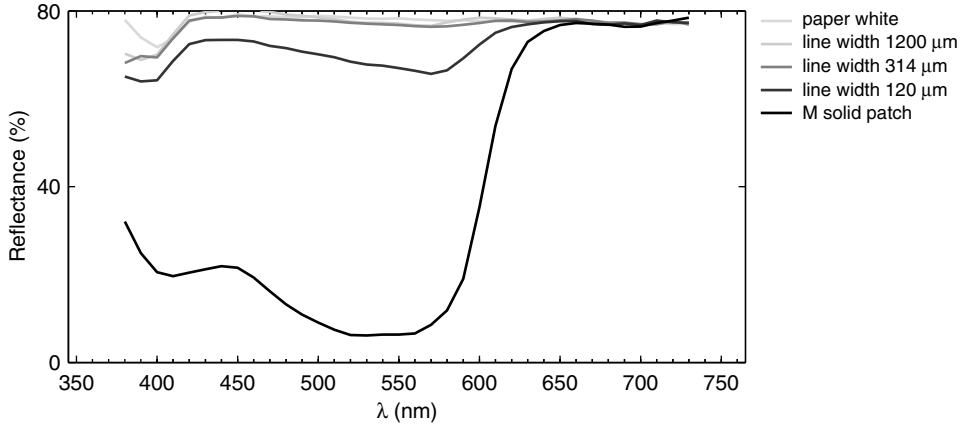

Figure 7.9: Micro-spectral measurements at the center of the micro-lines of figure 7.7, for different line width.

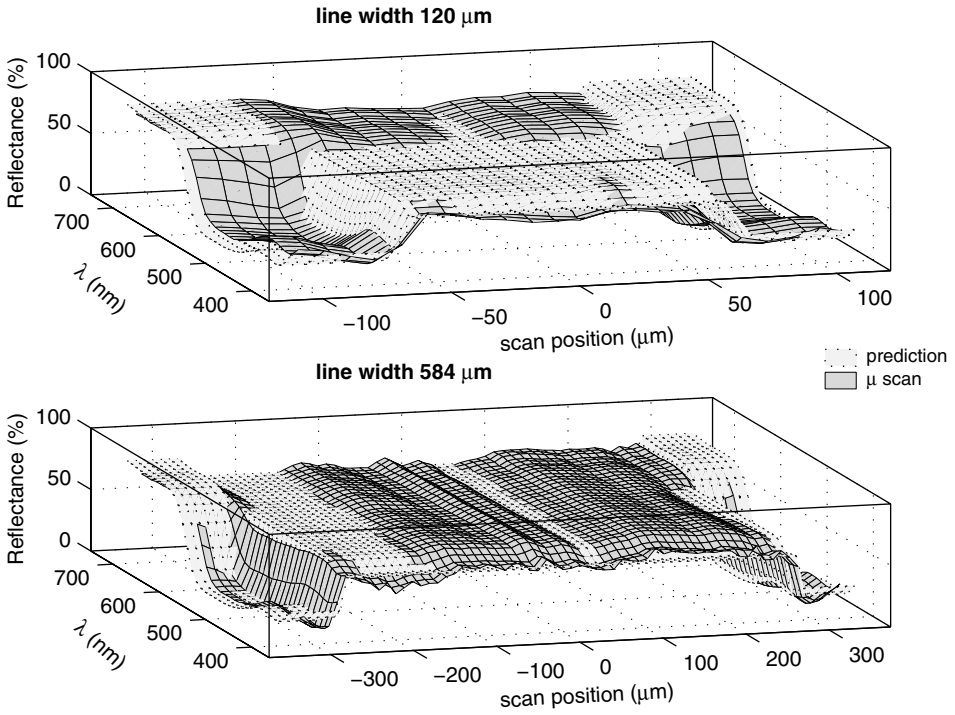

Figure 7.10: Comparison of micro-spectral measurement and prediction for a $0.6\,mm$ and a $0.1\,mm$ wide micro-line.

In addition to the shown qualitative edge agreement, the average match of the predicted spectral reflectance of the paper-white in the center of the micro-lines is also of interest, especially their dependence on line thickness. Figure 7.9 shows some of the spectral reflectances of the white micro-lines obtained by averaging the measurements of the middle areas where no magenta ink is apparent. The plot demonstrates the measured effect of the light scattered within the paper substrate. Obviously, without considering lateral scattering, a reflectance prediction of a printed halftone patch would lead to a brighter estimation than the real reflectance of the patch.

Qualitative micro-spectral agreement

Finally, the graphs in figure 7.10 show the obtained qualitative agreement for two different line thicknesses. They illustrate the measured micro-spectral reflectances at all scanned positions simultaneously in one graph.

7.2.4 Model evaluations, cartesian versus polar coordinates and the rotational symmetry

Besides being analytically similar, the light scattering models of chapter 6 obtained from the analysis in the cartesian and polar coordinate systems yield similar numerical results. As illustrated in figure 7.11, numerical evaluations of both models lead to a weak absolute deviation of less than 1 %. On the other hand, the point reflectance of a circular bitmap ought to be rotational symmetric too. The obtained

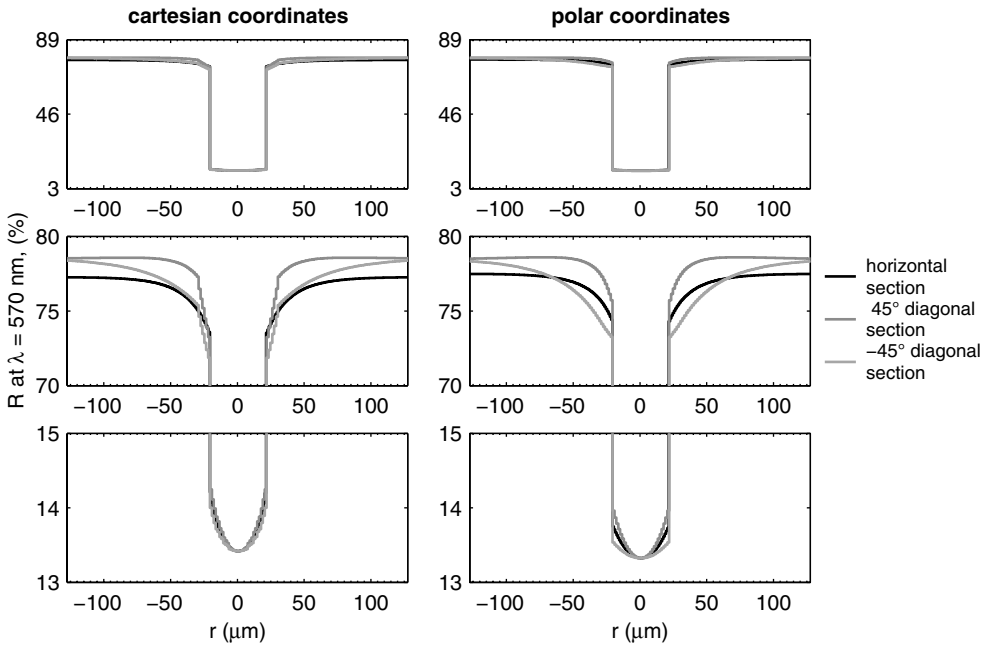

Figure 7.11: Comparison of the circular symmetry of the cartesian versus the polar coordinates light scattering model. The simulated bitmap is a circular black dot of 42 μm diameter placed at the center of a white patch.

rotational symmetry of the spectral reflectance predictions is also tested in figure 7.11 by the sketched diagonal and horizontal sections. It is equally fulfilled for both models to about 99 %. Moreover, the remaining partial asymmetry is due to aliasing and numerical artifacts of the two-dimensional convolution and its inverse numerical FFT transform. Nevertheless, in agreement with the purpose of the thesis, and in order to reduce the load of the numerical evaluations, the model based on the polar coordinates is chosen for all further numerical calculations.

7.3 Simulating the effects of the optical dot gain

The correspondence between the micro-spectral measurements and the light scattering model (section 7.2.3) makes it possible to simulate the point reflectance of arbitrary prints accurately. Further, assuming an ideal printer that reproduces without mechanical dot gain, the separate effect of the optical dot gain can be analyzed with a simple simulation of a black and white halftone print at different scales as illustrated in figure 7.12. In this figure, the variation of the paper-white as a function of the reproduction scale represents the key effect of the optical dot gain. As opposed to the general expectation, no significant edge deterioration is apparent compared with the whiteness degradation of the white areas. The corresponding reflectance profiles given in figure 7.13 demonstrate the whiteness degradation even better. This numerical experiment again emphasizes the importance of taking the considered effects into account. It further stresses the di-

Edge sharpness versus paper-white

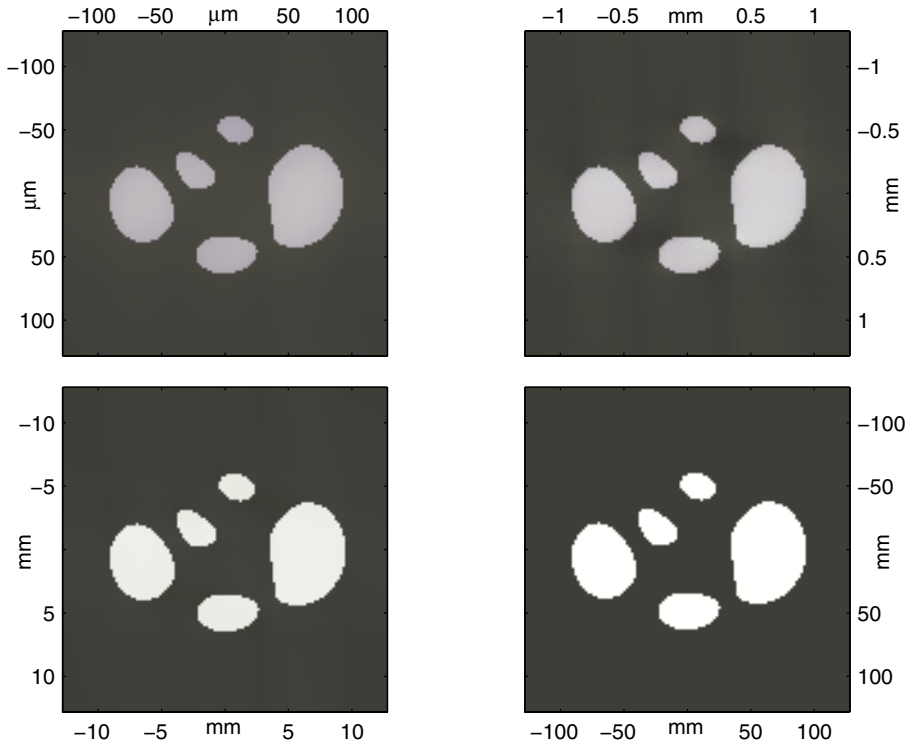

Figure 7.12: Reflectance simulations of an arbitrary black and white halftone print at different reproduction scales. The images represent a gray value transformation of the predicted reflection spectra.

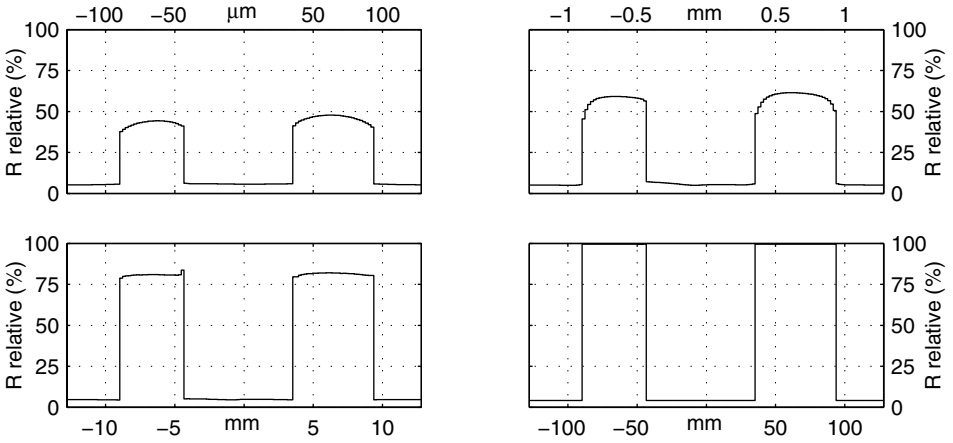

Figure 7.13: Horizontal sections through the center of the simulated point reflectance of figure 7.14 at $570\,nm$ relative to paper-white.

rect dependence of any color-management concept upon the underlying halftone algorithms used.

Clearly, the assumption of a perfectly semi-isotropic scattering medium explains the obtained results. Over a certain dimension—which may be called the *mean free path* [Gus97]—the incident light is attenuated by an average of the point transmittance function of the surface print. Then, within the substrate, the light

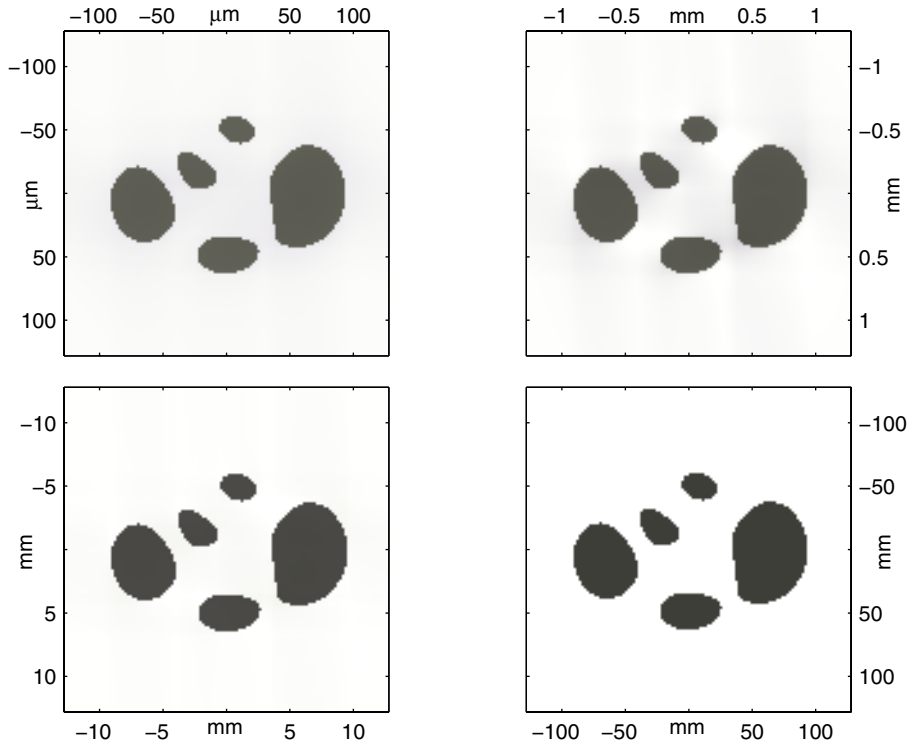

Figure 7.14: Reflectance simulations of a halftone print at different reproduction scales employing the inverted bitmap of figure 7.12.

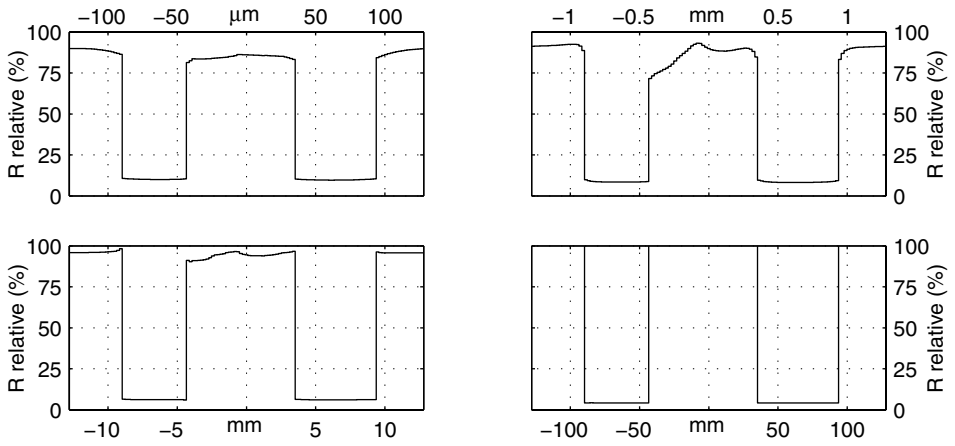

Figure 7.15: Horizontal sections through the center of the simulated point reflectance of figure 7.14 at $570\,nm$ relative to paper-white.

flux is homogeneously diffused and bears a spectral intensity to the first order corresponding to the average of the considered print area. Due to this theory, the diffuse substrate acts now as a diffuse light source illuminating the surface print from the bottom, which is in general agreement with [RH78, sec. iii]. In this constellation, the pronounced proportion of the paper-white degradation versus the almost unnoticeable dot sharpness deterioration is obvious. Corresponding simulations of the inverted bitmap are shown in figures 7.14 and 7.15. In con-

Discussion: an isotropic scattering result

trast to the simulations of a mainly black bitmap, the paper-white degradation is much less apparent in the case of sparely printed black halftone dots. However, in the black regions, the reflected intensity—or more precisely its corresponding density—changes considerably as a function of the halftone pattern width. The main feature of the light scattering effect, namely its induced wide neighboring dependency, remains present.

7.4 Discussion

The proposed model calibration approach presents a paper characterization method that fits well into the traditional work-flow of macroscopic optical measurements of solid prints. In particular, the approach facilitates the characterization of the light scattering property of a given paper substrate *independently* of the used printer's mechanical dot gain.

In order to determine the point transmittance $\vartheta_{t_\lambda}(x, y)$ of printed halftones, additional models are needed, which account for the physical effects of the ink deposition of a given printing device as a function of any input halftone color separation bitmap. The following section introduces a simulation model that computes the internal transmittance microstructure of electrophotographic toner halftone prints.

Electrophotographic application

8 Modeling electrophotography

Given a calibrated light scattering model for a chosen paper type, it is possible to estimate the point reflectance of any halftone patch as a function of the point transmittance of the printed ink layers. As an application of this theory, selecting the electrophotographic process as an example of a well established modern digital printing device is proposed.

After a short review of the development of electrophotography, the chapter proposes an estimation concept of the point transmittance of any uniform color halftone patch. With simplified numerical models, the concept analyzes and simulates the relevant effects of the involved electrophotographic subprocesses. They comprise the exposure of the printed bitmap, the forming of the attracting electrostatic field, the random charging and sizing of the toner particles, the toner layer transfer and color accumulation, as well as the concluding fusing step. The point transmittance of a printed halftone patch is estimated by starting from a bitmap of the input page and simulating all the main process steps.

8.1 History of electrophotography

In the early twentieth century, people could not easily reproduce documents. The *mimeograph*, also called the *stencil duplicator* invented by Edison, was one of the only competitive copying techniques. The name is derived from *mimos*, an ancient Greek word for burlesque theater. It is basically a duplicating machine that uses a stencil consisting of a coated fiber sheet through, which ink is pressed [Bri]. However, the reproduction with the mimeograph was tedious and required a prepared stencil and careful printing. The alternatives at that time were limited to expensive photo copies or to retyped documents.

Carlson, a patent attorney, clearly identified the needs of modern offices for easily made and less costly document copies. With the help of his assistant Kornei, in 1938 he obtained a first dry-copy by applying the fascinating combination of electrostatics and photoconductivity. A sample of the copy is shown to the right. The invention was called *electrophotography* or *xerography*, a Greek word for *dry writing*. During the past century, electrophotography became the basic technology for copying machines and laser printers [XHs].

8.2 The electrophotographic process

The key process of electrophotography is the formation of an electrostatic latent image on a *photoconductor*, and the development of that image with electrostatically charged powders. The photoconductor is usually applied to a grounded belt and acts as an insulator in the darkness. In the presence of light it generates and transports electron-hole pairs in response to absorbed photons. Many of the scientific aspects of electrophotography, such as electrostatic, material science, tribology and adherence are rather elaborate and yet not fully explained. Basically, the electrophotographic process illustrated in figure 8.1, is subdivided into six subprocesses and introduced hereafter [Wil84, Sch96].

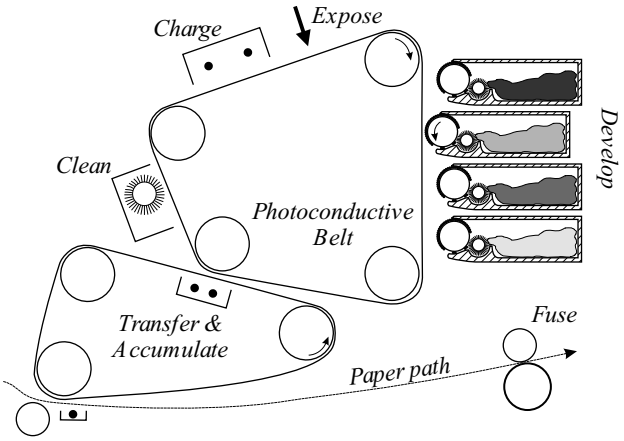

Figure 8.1: Schematic representation of an electrophotographic color desktop printer.

8.2.1 Charging the photoconductor

Corona

Scorotron

In the absence of light, the initially uncharged surface of the photoconductor is uniformly charged to the *dark voltage* , which reaches values of ± 1 kV. The uniform charge distribution is generated by absorbing ionized gas molecules that arise from a supplied electrical *corona* device. This device employs thin wires set to a very high potential inducing a high electric field in the vicinity of the wires. The field accelerates any free electrons to sufficiently high velocities so as to ionize any intervening gas molecules. Influenced by the applied field, the generated ions and electrons move in opposite directions. The electrons reach the corona device and reenter the electric circuit. On the other hand, the ions move towards the photoconductor, charging up its surface electrostatically. The uniformity of the ion deposition on the photoconductor surface is controlled by an additional wire screen set to a voltage that determines the approximate charge potential of the photoconductor. Such a screen-controlled corona device is called *Scorotron*. Generally, the resulting surface charge is considered to be neither dependent on the current bitmap nor on the previously printed ones.

8.2.2 Exposing the photoconductor

Within the exposure step, the charges at the surface of the photoconductor are selectively recombined and discharged. In common digital printers, the image is exposed pixel by pixel by applying a focused laser beam or line-wise by a diode array. The exposed energy generates charge carriers within the *charge generation layer* of the photoconductor. The amount of generated charges is determined by the *quantum efficiency* that reaches values between 0.1 and 1. Influenced by the internal electric field arising from the initially charged photoconductive surface, the generated charges drift through the *charge transport layer* with a drift velocity of about 50 mm/s. The velocity is determined by the *hole* or *charge mobility*. Reaching the surface, the transported charges recombine with the deposited surface ions and liberate neutralized gas molecules. The value of the resulting discharged surface voltage is called the *image potential* or the *light voltage*. The difference in potential between the dark and the light voltage is called the *contrast voltage*, which is usually situated between 300 and 600 V.

Contrast voltage

8.2.3 Image development

The exposed invisible *latent image* is made visible by the deposition of *toner* particles onto the photoconductor. This development step relies on the movement of charged bodies in electric fields driven by the Coulomb force. This force is determined by the variations in voltage along the photoconductive surface and thus by the image potential.

In the early twentieth century, one of the technical challenges of the development step was the image formation of solid areas. It was not solved until the basics of the acting forces within the development nip were understood. A solid area commonly has a uniformly charged latent image. Within this charged area, the only electric field above the photoconductor is associated with the fringe field at the edges of the solid area. Therefore, only the edges of the solid areas are developed. To be able to print in solid areas, a *development electrode* was introduced. It is installed within the developer unit above the development nip. This electrode adds a constant field sufficiently large to develop toner in solid areas [Sch96].

Image defect of solid areas

Driven by the competitive market, suppliers of electrophotographic devices alter their engines by varying the relevant subprocesses and by employing different underlying physical concepts. Various development subsystems and related toner families are proposed. These comprise the *two-* or *monocomponent developers*, the *magnetic* and the *non-magnetic*, the *liquid* and *dry developers* as well as the distinction made between the *conductive* and *nonconductive* toners [Wil84]. Despite these variations, the toner particles are commonly statistically distributed in charge and in size. The charge distribution is mainly controlled by the triboelectric effects, whereas the size distribution is controlled by the manufacturing process. Accordingly, a comprehensive theory of image development should account for

Types of toner

electrostatic, electrodynamic and thermodynamic forces in addition to gravity. All of them are forces which act on the toner particles and the carrier beads.

8.2.4 Image transfer

Transfer efficiency

The transfer step refers to the transportation of the developed image onto the printing substrate such as a paper or a transparency. Usually, the transfer step is accomplished by applying a *transfer corona* device, which induces a supporting electrostatic field. The corona device helps to reinforce the attraction of the toner layers to the printing substrate and to optimize the separation of the toner upon separating the paper from the photoconductor surface. The rate of transfered toner particles is called the *transfer efficiency*. It is mainly determined by the geometrical setup of the transfer unit and the developed image in addition to the dielectric constants of the involved layers. After transfer, the charged toner sticks temporarily to the paper due to the electrostatic force and the image needs to be fixated for any subsequent handling.

8.2.5 Image fusing

Fusing is the long-term fixation of the transfered image onto the printing substrate by applying *heat and pressure*. This technique has proven to be a reliable method for permanently fixing the image. Other, but less significant fixation techniques also have been applied. Among others they comprise *solvent*, *pure thermal*, *pure pressure* fixing or fusing by *post processed*uv-*additives*.

Determining print quality

Many of the attributes of printing quality such as *image gloss* or *paper curl* are determined by the fusing step. In the case of the widely used heat and pressure fusing process, the obtained quality depends on the applied *fusing temperature*, the *nip geometry*, the achieved *pressure* and the *dwell time*. Finally, the paper properties such as the average fiber diameter, and the mean distance between fibers have also an impact on the fused image.

8.2.6 Cleaning

Cleaning failures

Before starting a new process cycle, any remaining charges or residual untransfered toner particles must be removed. Otherwise, the images of the subsequent cycles may be affected by the residual charges and particles. Common cleaning steps employ additional coronae to discharge the remaining toner charge. Light sources are also applied, which discharge the photoconductor in addition to cleaning brushes or blades, thereby wiping off any excess toner. Cleaning failures are manifold. The worst failure is the so called *fused-on toner*, which permanently alters the electrical nature of the photoconductor due to the common insulating toner property. Other cleaning defects occur due to particles displaced by a scraper blade causing *streaking*, or due to redeposited toners from cleaning brushes yielding the *cleaner offset*.

8.3 Modeling the electrophotographic process

The model presented below considers dry electrophotographic processes with mainly non-magnetic developers. Observed under a microscope, the dots of desktop electrophotographic prints appear mostly like clouds of randomly distributed toner particles. Occasionally, the particles are deposited beyond their target area and form extremely ragged dot edges. The high dot distortion causes the major difficulty in estimating the color of an electrophotographic print and affects its tonal reproduction curve. In addition, the electrophotographic particle clusters are strongly influenced by their surroundings—a phenomenon called the *adjacency effect* [Wil84]. The microscopic images in figure 8.2 of an electrophotographic print demonstrate for instance the noticeable increase of the particle concentration in the depicted target area. The higher concentration achieved in the right-hand image is simply caused by the presence of a large solid patch printed as far as 14 *dots* away from the target area.

Adjacency effect

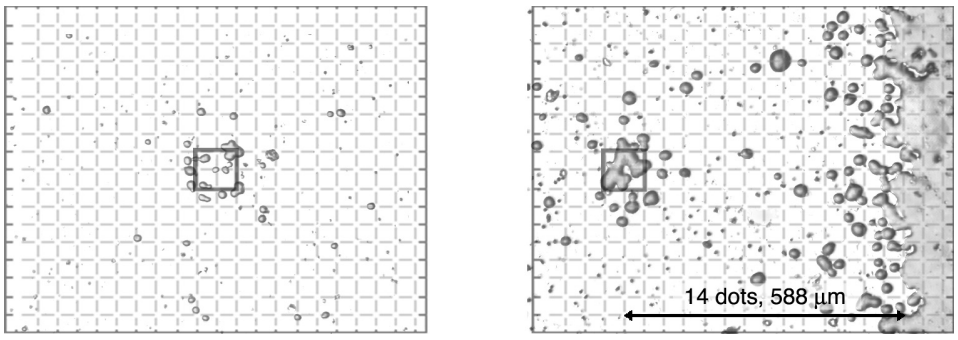

Figure 8.2: Microscopic images of electrophotographic transparency prints. The considered printer has a resolution of 600 *dpi*. The images are overlapped with a corresponding resolution grid, and a rectangle indicates the position of the addressed target area of the input bitmap. *Left side*: printing result of a 2×2 dot placed in a clear area. *Right side*: corresponding result of a 2×2 dot print in relative proximity of a solid patch.

The main reason for the high nonlinear characteristic is the combination of different forces together with the stochastic charge and size distribution of the toner particles. In order to cope with these nonlinearities, an electrophotographic simulation model is proposed, which accounts for the relevant physical effects. The model is based on simplifying assumptions representing a tradeoff between physical relevance, accuracy and simplicity [MEH00, MEH01]. In order to estimate the spectral point transmittance of any uniform color halftone patch, the model takes the input color separation of each primary ink and passes it through simulations of the important electrophotographic steps. As already mentioned, the considered steps comprise the formation of the attracting electrostatic field, the stochastic toner characteristics, the transfer and accumulation of the different color layers, as well as the concluding fusing step. The charging and cleaning steps are neglected, assuming that they operate properly and homogeneously.

8.3.1 Geometric dimensioning of the model

The model uses a microscopic pixel grid $\mathbb{XY}$ with a resolution of 6.0 μm representing the lower average particle size of commonly used toners. For a desktop printer with an addressability of 600 *dpi* (*dots per inch*), the effects of the significant process step are simulated on a 677×677 μm wide segment of a uniform color patch comprising 16×16 *dots*. Considering uniform color patches only allows to limit the extend of the analyzed segment to the proposed square of 16 dots. The surface of the photoconductive plate is assumed to be homogeneously charged. It is also assumed that the surface charge is neither dependent on the current color separation nor on the previously printed ones. Therefore, to predict toner deposition characteristics, the first significant process step is to create the attracting electrostatic forces acting above the exposed photoconductive plate.

8.3.2 The electrostatic field of an exposed bitmap

While exposing an image, the photoconductor voltage is selectively altered in proportion to the number of photons absorbed in the charge-generating layer. In the development step, the latent image is brought into the vicinity of charged toner particles under the influence of the development electrode introduced in section 8.2.3. In first order considerations, both the image contrast voltage and the constant electric field of the development electrode ascertain the total electric field within the development nip. This total field is responsible for the forces acting on the toner particles. Hence, the total field determines the obtained print image density.

The attracting electrostatic field is modeled on a circular convolution kernel derived below. The kernel characterizes the attracting field of a *single* exposed dot in the vicinity of a development electrode. To accommodate various electrophotographic systems, the kernel is constructed as an approximating function, which is sufficiently flexible to model the electrostatic field of any particular system.

Neugebauer and others have shown that the density of an electrophotographic image is essentially given solely by the perpendicular component of the electrostatic field directly above the photoconductor [Neu65a]. In his publications [Neu65b, Neu67, Sch75], Neugebauer introduced $C(k)$, a modulation transfer function (MTF) relating the electrostatic field within the developer nip to the line exposure of a photoconductor

$$C(k) = C_0 + \cosh\Big(k\cdot\big(L_1 - z\big)\Big) \times \frac{\sinh\big(k\cdot L_2\big) - \frac{\beta}{kL_2}\cdot\Big(\cosh\big(k\cdot L_2\big) - e^{-\beta}\Big)}{\Big(\cosh\big(k\cdot L_1\big)\cdot\sinh\big(k\cdot L_2\big) + \eta\cdot\sinh\big(k\cdot L_1\big)\cdot\cosh\big(k\cdot L_2\big)\Big)\cdot\Big(1 - \big(\frac{\beta}{kL_2}\big)^2\Big)}\,, \tag{8.1}$$

where C_0 describes the field enhancement induced by the development electrode. k is the exposed line frequency given as 2π line pairs per μm, L_1 is the distance

between the development electrode and the photoconductive plate and L_2 is the thickness of the photoconductive plate, see figure 8.3. β is a function of L_2 representing drift mobility, the initial plate voltage and other electrostatic effects

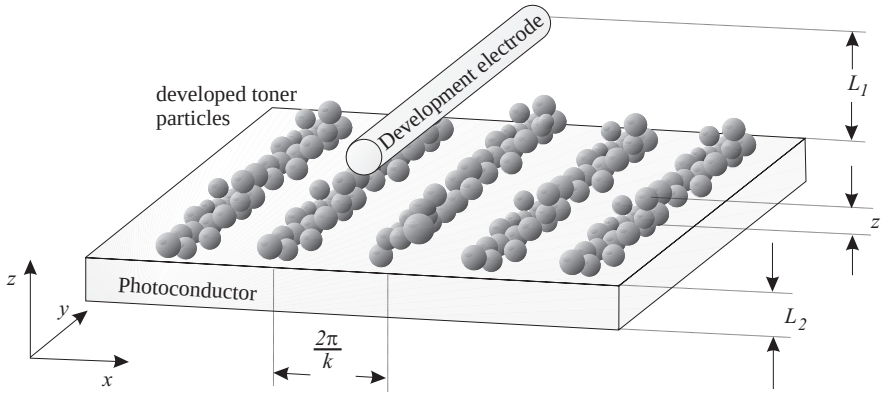

Figure 8.3: Sketch of an exposed photoconductive plate being developed in the vicinity of a development electrode.

of the charge transport layer of the photoconductor. η is the dielectric constant of the plate and finally, z is the average distance between the electrophotographic plate and the center of charge of the caught toner particles above the plate.

Inverting the MTF $C(k)$ by a high-resolution numerical Fourier transform yields the electrostatic field $c(r)$ of an infinitely small exposed dot, i.e. the point spread function (PSF) at the spatial coordinate r. Hence, the perpendicular electrostatic field component $H_{E_z}(r)$ of a particular printer is determined by the one-dimensional convolution "$*$" of $c(r)$ with the intensity profile of the exposing light spot

$$H_{E_z}(r) = I(r) * c(r)\,. \tag{8.2}$$

$I(r)$ is a saturated Gaussian Intensity profile of the exposure spot given by

$$I(r) = \begin{cases} I_{sat} & \forall r \in [\,-r_{\mathrm{Ex}}, r_{\mathrm{Ex}}\,]\ , \\ I_0 \cdot e^{-0.5\left(\frac{r}{\zeta}\right)^2} & \text{otherwise}\ , \end{cases} \tag{8.3}$$

where I_{sat} is the saturation intensity, $\pm\, r_{\mathrm{Ex}}$ are the solution of $I(r) = I_{sat}$ for r. I_0 as well as ζ are constants determined by the exposure unit. The implemented saturation is in conceptual accordance with the discussion made in [Wil84, ch. 5].

The circular convolution kernel $H_{E_z}(x, y)$ of a single exposed dot is approximated by rotating $H_{E_z}(r)$ around the vertical axis z. This is basically done by substituting $\sqrt{x^2 + y^2}$ for r where $(x, y) \in \mathbb{XY}$ (section 8.3.1). An example of the resulting dot field approximation is shown in the upper-right part of figure 8.4.

The proposed electrostatic dot field component takes into account most of the significant electrostatic parameters of the exposure and developer units. Among others, these parameters comprise the shape of the exposure spot, the thickness of

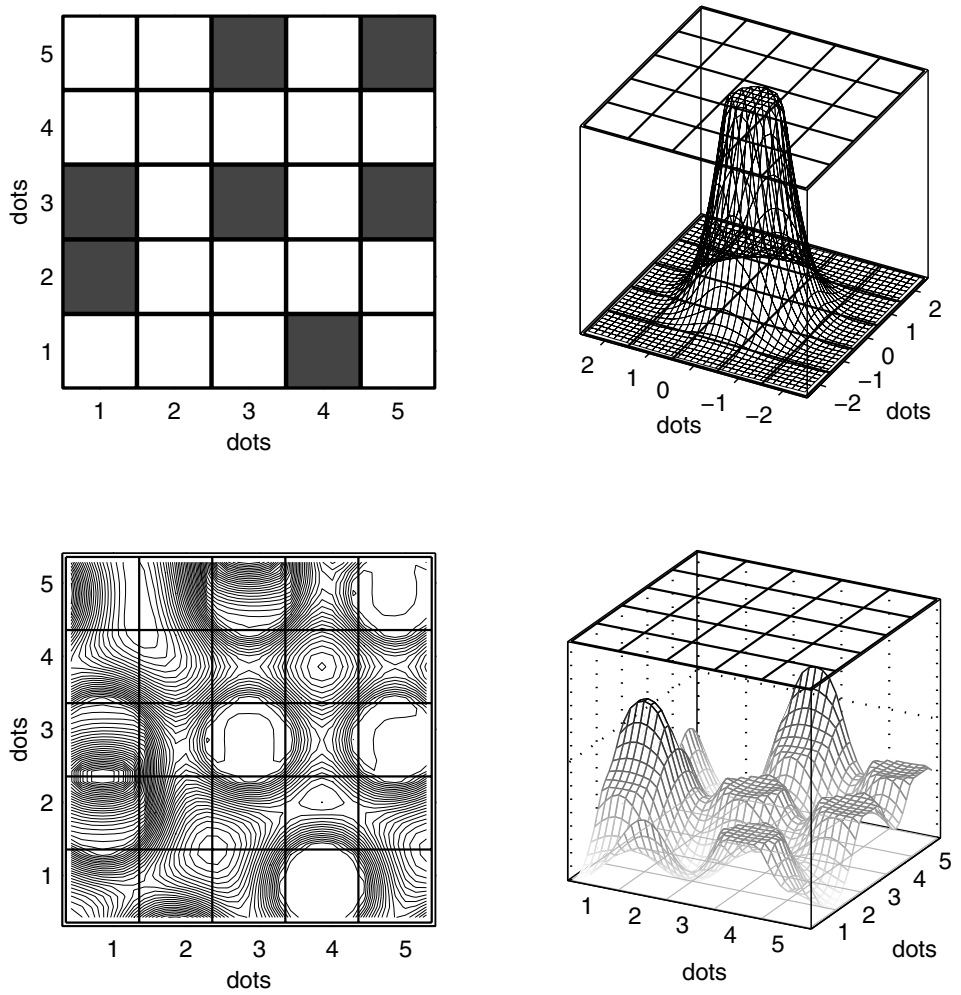

Figure 8.4: *Upper left*: Enlarged section of an input bitmap. Note, this is a part of a larger bitmap, i.e. directly adjacent but omitted dots may be exposed as well. *Upper right*: The perpendicular electrostatic field component of a single dot ($H_{E_z}(x, y)$). *Lower left*: Contour plot of the resulting electrostatic field $E_{z_c}(x, y)$ of one color separation c, i.e. the latent image. *Lower right*: Three-dimensional representation of the same electrostatic field.

the photoconductive plate, the distance between the plate and the development electrode, an average charge height above the plate of the caught toner particles, the initial plate voltage and its dielectric constant. Strictly speaking, the chosen grid of 16×16 *dots* cannot account for the total extend of the adjacency effect. However, since the field's amplitude vanishes rapidly with increased distance, for the sake of computability, its remaining influence is neglected. For any exposed bitmap $bmp_c(x, y)$ of a given color c, the overall perpendicular component of the attracting electrostatic field $E_{z_c}(x, y)$ is easily obtained by superposing the perpendicular field kernel $H_{E_z}(x, y)$ of a single dot at each exposed dot location. Mathematically this is obtained by the two-dimensional convolution "$**$"

$$E_{z_c}(x, y) = bmp_c(x, y) ** H_{E_z}(x, y) \ . \tag{8.4}$$

Figure 8.4 depicts the result of such an operation on a section of a large input bitmap shown in the upper-left part. Each center of an exposed dot is superposed by the kernel shown in the upper-right part yielding the perpendicular field distribution forming the latent image as illustrated in the lower part of the figure.

8.3.3 The toner charge and size distributions

Due to the manufacturing and charging processes, the toner particle size and charge are always distributed in a statistical manner. These distributions have a joint impact on the printed image quality. On the one hand, the charge distribution influences the development behavior. On the other hand, the size distribution mainly affects the micro transmittance structure of the printed result. In order to roughly model the toner charge and size distributions, a lognormal based probability density function (pdf) was proposed in [MEH00, MEH01], which approximates the expected statistical characteristic of the toner charge q for each color c

$$\mathrm{pdf}_{q_c}(\kappa) = \gamma - \frac{1}{\kappa \cdot \upsilon \cdot \sqrt{2\,\pi}} \cdot e^{-\frac{\ln^2(\kappa-\mu)}{\upsilon^2}} \quad , \tag{8.5}$$

with the characteristic constants γ, υ and μ. κ represents the independent statistical variable. The distribution of the particle diameters or their pile height δ is simulated according to a Rayleigh-based distribution

$$\mathrm{pdf}_{\delta_c}(\kappa) = a + \frac{\kappa}{b^2} \cdot e^{\frac{-\kappa^2}{2b^2}} \quad , \tag{8.6}$$

using a and b as distribution constants. The introduced constants need to be fitted in order to match the expected general shapes of the distributions as illustrated in figure 8.5. Generally, these distributions match the general shapes reported

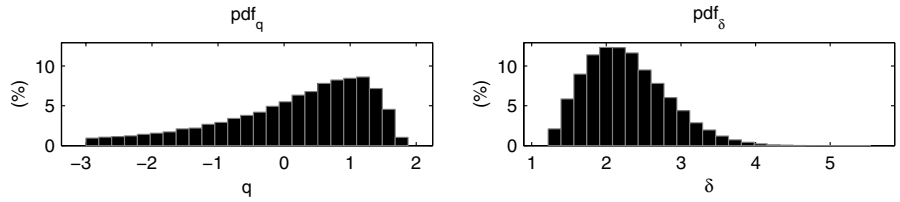

Figure 8.5: An example of the simulated toner particles charge distribution at the *left* and size distribution at the *right*.

in various investigations and measurements found e.g. in the [NGM98, a.o.]. For each pixel $(x, y) \in \mathbb{XY}$ and each color c the toner particles present at the developer nip are simulated with two independent high-resolution simulation grids of random numbers fulfilling the corresponding characteristic distributions. One grid frame $Q_c(x, y)$ represents the toner charges and is obtained using the distribution equation (8.5). The second grid frame $D_c(x, y)$ is evaluated according to the distribution equation (8.6) and is used in order to represent the pile height of the toner particles present at the developer nip.

8.3.4 The development of the latent image

In the developer nip, the obtained latent image is made visible by depositing the toner particles on the photoconductor dependent on the attracting electrostatic field. In agreement with Coulomb's law, the electrostatic force $\overrightarrow{F_C}$ is basically given by the linear relationship between the particle charge q and the acting electrostatic field $\overrightarrow{E}$

$$\overrightarrow{F_C} = q \cdot \overrightarrow{E} \ . \tag{8.7}$$

For simplicity, it is assumed that particles are deposited only as soon as the attracting perpendicular component of the Coulomb force F_{C_z} is strong enough to overcome the impeding adhesion threshold force τ_{imp}. The development condition is evaluated for each color c at each pixel (x, y) of the toner charge simulation grid frame $Q_c(x, y)$ introduced in section 8.3.3. The condition is evaluated using the perpendicular electrostatic field component $E_{z_c}(x, y)$ of the latent image given with equation (8.4). The pile height of the developed particles $\delta_{\mathrm{Dv}}(x, y)$ is simulated using $D_c(x, y)$ introduced in section 8.3.3 as follows

$$\delta_{\mathrm{Dv}_c}(x, y) = \begin{cases} D_c(x, y) & \forall\,(x, y) \in \left\{(x, y) \in \mathbb{XY} \,|\, Q_c(x, y) \cdot E_{z_c}(x, y) \ > \ \tau_{imp}\right\} \ , \\ 0 & \text{otherwise} \ . \end{cases} \tag{8.8}$$

The upper-right part of figure 8.6 illustrates the developed toner particle frame $\delta_{\mathrm{Dv}_c}(x, y)$ of a corresponding simulation using the same perpendicular component of the electric field $E_{z_c}(x, y)$ as illustrated in figure 8.4. This field is redrawn again in the upper-left part of the figure for comparison purposes. The gray level of the illustrated pixels represents the simulated pile height variation of the developed toner particles.

8.3.5 Transfer and accumulation of multi-color toner layers

The developed toner particles of each color layer are transported from the photoconductor to a transfer belt depicted in figure 8.1. Depending on the technical setup of the printer, the transfer belt accumulates the different color layers stacked on top of each other. Finally, the piled color layers are transported simultaneously to the printing medium. During this whole process, the toner particles can either be rejected or repulsed according to the *transfer efficiency* (section 8.2.4). During the transfer step, the interference between the color layers cannot be avoided and their interdependency must be taken into account.

Auto transfer efficiency

It is assumed that the main effect of the transfer step is characterized with the transfer efficiency factor ε, which determines the rejected part of the particles. The transfer efficiency of each color layer is subdivided into two components [MEH01]. A first independent *auto transfer efficiency* ε_c is introduced describing the lack of transfer of a single color layer c in the absence of any other color layers. Having a total of N simulated high-resolution pixels, the affected transfer part

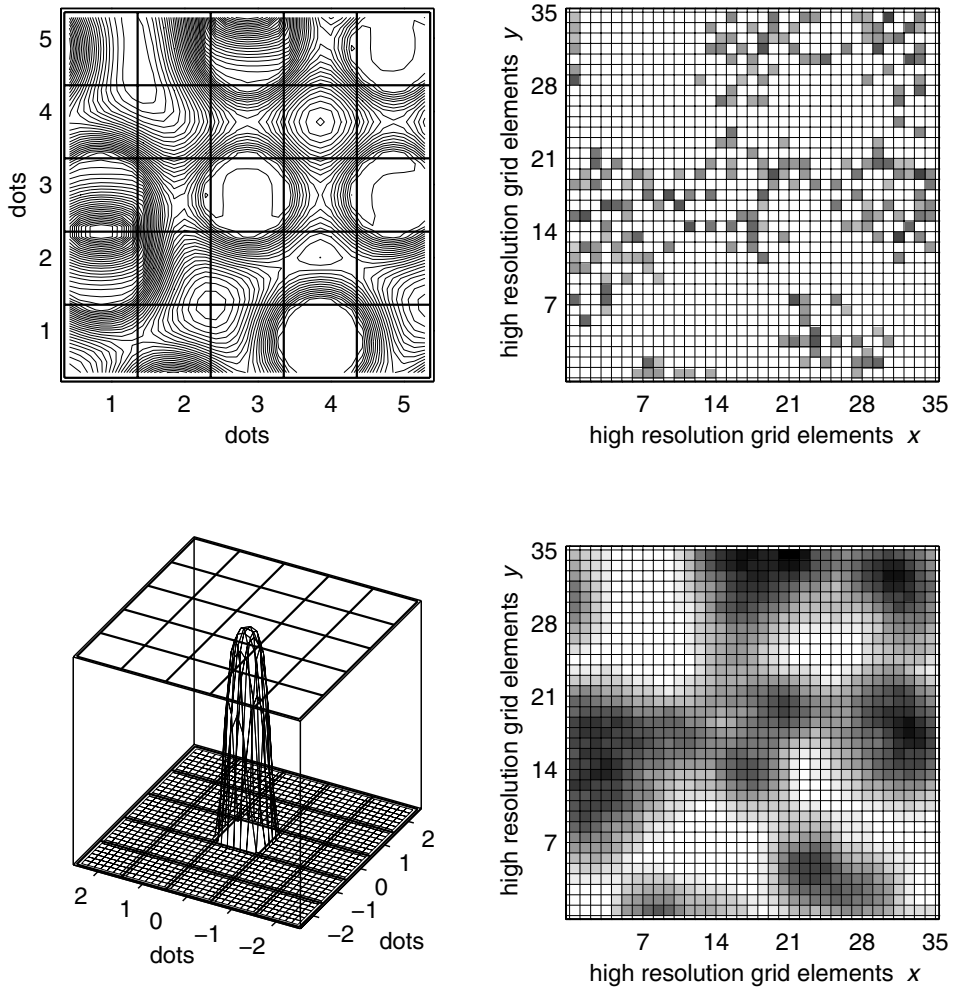

Figure 8.6: *Upper left*: Contour plot of the electrostatic field of one color separation using the same data as represented in figure 8.4. *Upper right*: Simulation of the developed toner particles. Black represents the maximum thickness, and white represents a non-developed position. *Lower left*: Convolution kernel H_{F} used to simulate the effect of the fuser on the transfered toner particles. *Lower right*: Simulation of the fusing effect on the transfered monochrome toner layer shown in the upper right part of this figure.

is modeled by randomly selecting $N \cdot (1 - \varepsilon_c)$ pixels from the developed image $\delta_{\mathrm{Dv}_c}(x, y)$ and reducing their toner pile height by the random amount ϱ. Given the operator $\mathcal{R}_K(\mathbb{S})$ that returns a randomly selected subset of total K elements of an arbitrary input set $\mathbb{S}$, the transfered layer $\delta_{\mathrm{Tr}_{c\ auto}}(x, y)$ is written as

$$\delta_{\mathrm{Tr}_{c\ auto}}(x, y) = \delta_{\mathrm{Dv}_c}(x, y) - \Delta_{\varepsilon_c}(x, y) \ , \tag{8.9}$$

where $\delta_{\mathrm{Dv}_c}(x, y)$ is given in equation (8.8). $\Delta_{\varepsilon_c}(x, y)$ is the random pile height reduction frame given by

$$\Delta_{\varepsilon_c}(x, y) = \begin{cases} \varrho & \forall\,(x, y) \in \mathcal{R}_{N\cdot(1-\varepsilon_c)}(\mathbb{X}\mathbb{Y}) \ , \\ 0 & \text{otherwise} \ . \end{cases} \tag{8.10}$$

Cross transfer efficiency

The second efficiency component is introduced as the *cross transfer efficiency* ε_{c,c_1} describing the influence of any additionally printed color layer c_1 above or beneath the layer c. The influence of the cross transfer efficiency is modeled by randomly reducing the toner pile height of the color layer c due to its interactions with the layer c_1 within a 3×3 neighborhood by a new calculated random amount ϱ. In order to formulate the concept, let us call $\mathcal{X}_{n\times n}(\mathbb{S}1, \mathbb{S}2)$ a neighborhood operator returning a subset of pixels $(x, y) \in \mathbb{XY}$, which contains at least one pixel other than zero in both layers $\mathbb{S}1$ and $\mathbb{S}2 \subset \mathbb{XY}$ within a $n \times n$ neighborhood. N_3 shall be the total number of pixels $(x, y) \in \mathcal{X}_{3\times3}(\delta_{\mathrm{Dv}_c}, \delta_{\mathrm{Dv}_{c1}})$, then assuming that these interactions takes only place at $N_3 \cdot (1 - \varepsilon_{c,c1})$ pixels, the transfered layer $\delta_{\mathrm{Tr}_{c,c1}}(x, y)$ may be written as

$$\delta_{\mathrm{Tr}_{c,c1}}(x, y) = \delta_{\mathrm{Dv}_c}(x, y) - \Delta_{\varepsilon_{c,c1}}(x, y) \qquad \text{with} \tag{8.11}$$

$$\Delta_{\varepsilon_{c,c1}}(x, y) = \begin{cases} \varrho & \forall\,(x, y) \in \mathcal{R}_{N_3\cdot(1-\varepsilon_{c,c1})}(\mathcal{X}_{3\times3}(\delta_{\mathrm{Dv}_c}(x, y)\,, \delta_{\mathrm{Dv}_{c1}}(x, y)))\ , \\ 0 & \text{otherwise}\ . \end{cases}$$

Taking the neighborhood into account makes it possible to approximate the effects of the electrostatic interactions between neighboring particles located in different layers. Finally, when printing with 3 different colors, the total transfered particles of each color c_n are given by the combination of the relations (8.9) and (8.11) influenced by all other color layers c_m where $m \in \mathcal{N}_n = \{1 \cdots 3\} \setminus \{n\}$ where "\" is difference operator of two sets. Additionally, overprinting all primary colors together may affect each separate color layer c_n. This is considered with the factor $\varepsilon_{c_n,all}$ yielding an approach which may easily be generalized to the case of printing M colors

$$\delta_{\mathrm{Tr}_{c_n}}(x, y) = \delta_{\mathrm{Tr}_{c_n\ auto}}(x, y) + \sum_{m\in\mathcal{N}_n} \delta_{\mathrm{Tr}_{c_n,cm}}(x, y) + \delta_{\mathrm{Tr}_{c_n,all}}(x, y)\ . \tag{8.12}$$

8.3.6 Toner spreading during the fusing step

After transferring the toner layers to the printing medium, the developed image is fixed permanently by melting the toner to the medium. The main effects of the fixing heat and pressure within the fuser nip, such as toner flow, spread and particle join are simulated by applying a smoothing filter on the transferred particles $\delta_{\mathrm{Tr}_c}(x, y)$ of equation (8.12). For simplicity, the proposal is to apply a fusing filter convolution kernel $H_{\mathrm{F}}(r)$ based on a hyper-parabola given by

$$H_{\mathrm{F}}(r) = \begin{cases} 1 - \left(\frac{r}{r_{\mathrm{F}}}\right)^4 & \forall r \in [\,-r_{\mathrm{F}}, r_{\mathrm{F}}\,]\ , \\ 0 & \text{otherwise}\ , \end{cases} \tag{8.13}$$

where r_{F} represents the average fuser spreading width. The fused thickness profile $\delta_{\mathrm{F}_c}(x, y)$ of each color layer c is then given by the convolution operation

$$\delta_{\mathrm{F}_c}(x, y) = \delta_{\mathrm{Tr}_c}(x, y) \ast\ast H_{\mathrm{F}}(x, y)\ , \tag{8.14}$$

where (x, y) is substituted for r in equation (8.13). The filter operation averages the discontinuous character of the simulation of the transfered toner particles and produces a smooth image that corresponds to a high degree to microscopic images of electrophotographic prints [MEH00]. Such a simulation is illustrated in the lower-right part of figure 8.6. The obtained toner *relief* $\delta_{\mathrm{F}_c}(x, y)$ representing the relative thickness of the deposited toner clusters is the key element for the subsequent spectral transmittance calculation.

8.4 Computing the inner transmittance spectra of halftone prints

The internal point transmittance distribution $\vartheta_{t_\lambda}(x, y)$ needed in eq. (6.26) and (6.27) is computed by applying Bouguer–Beer–Lambert's law (section 4.1.2). Assuming weak light-scattering inks, the law given in equation (4.5) associates the internal transmittance ϑ_{c_λ} of a filter c having the relative thickness δ_c to its normalized transmittance $\vartheta_{ref_{c\,\lambda}}$

$$\vartheta_{c_\lambda} = \vartheta_{ref_{c\,\lambda}}^{\delta_c} . \tag{8.15}$$

Printing M overlapped primary inks, the point transmittance distribution $\vartheta_{t_\lambda}(x, y)$ is approximated according to equation (5.1) by the product of the internal spectral transmittance distributions

$$\vartheta_{t_\lambda}(x, y) = \prod_{c=1}^{M} \vartheta_{ref_{c\,\lambda}}^{\delta_{\mathrm{F}_c}(x,y)} , \tag{8.16}$$

with the fused relative thickness relief $\delta_{\mathrm{F}_c}(x, y)$ obtained from equation 8.14.

The presented electrophotographic model makes it possible to calculate the expected internal spectral point transmittance of a multi-color layer as a function of the input color separation $bmp_c\,(x, y)$ of all primary inks c. Using completely transparent transparencies, the presented electrophotographic model can be applied independently and calibrated as proposed in [MEH00, MEH01]. Furthermore, the lateral light scattering model presented in part II makes it possible to use the calibrated electrophotographic model to predict the spectral point reflectance of halftone prints on common office papers [MESH02]. Chapter 9 presents corresponding numerical calibration and evaluation results for color halftone prints.

9 Electrophotographic evaluations

The parameters of the proposed electrophotographic simulation model are estimated by using the previously established light scattering model. This chapter introduces a calibration approach where the reflectance spectra of a halftone calibration set are predicted and compared with measured spectra. The model parameters are fitted by minimizing the sum square differences between the spectral predictions and the measurements. Then, the chapter presents prediction results using a calibrated model for a particular electrophotographic desktop printer.

9.1 Calibrating the electrophotographic model

Independent calibration of both models

As shown in chapter 7, the calibration samples of the light scattering model consist solely of measured spectra of the paper-white in addition to the spectra of printed solid patches of each considered primary color. Therefore, for a particular paper/printer combination, the light scattering model is calibrated independently from any halftone prediction model such as the present electrophotographic simulation model.

Common spectral measurements

The proposed calibration approach requires only macroscopic spectral reflectance measurements that may be measured using a common spectrophotometer. Without loss of generality, the current presentation of the calibration is restricted to the trichromatic case, i.e considering only *cyan*, *magenta* and *yellow* halftone prints in addition to their combinations. Given a calibrated light scattering model and the input color separation $bmp_c\,(x, y)$, the spectral reflectance of any halftone patch is predicted by applying the model equations (8.16) and (6.33) sequently. The spectral reflectance estimate of a whole patch $\hat{R}_\lambda$, which corresponds to a macroscopic measurement with a common spectrophotometer, is given by the mean value of the spectra of the high-resolution grid elements $(x, y) \in \mathbb{XY}$ (see section 8.3.1) yielding

$$\hat{R}_\lambda = \frac{1}{N} \cdot \sum_{(x,y)\in\mathbb{XY}} \hat{R}_\lambda(x, y) \ , \tag{9.1}$$

where N is the total number of the computed grid elements. Equation (9.1) com-

bined with the insights of section 7.3 explains how macroscopic reflectance measurements of a print on paper depends on the microscopic point reflectances.

Calibration samples

Most of the model parameters determine the reproduction characteristics of monochrome halftone prints, i.e. single primary color prints. Only the cross transfer efficiency factors $\varepsilon_{c,cm}$ and $\varepsilon_{c,all}$ of equation (8.11) are determined by the multichrome reproduction characteristics. Accordingly, the *calibration samples* of the electrophotographic simulation model are subdivided into three groups. The first group comprises three *monochrome* halftone patches of each considered primary color, two intermediate halftone levels and the solid print. The second group considers the *bichromatic* print and consists of four halftone patches of each bichromatic combination, yielding a total of twelve patches for the considered *CMY* case. Finally, the third group comprises the *trichromatic* combination of an intermediate halftone level in addition to the solid prints of each primary color yielding a set of eight patches. The result is a calibration chart having only 29 halftone patches, which ought to fully characterize the considered electrophotographic desktop printer.

9.1.1 Calibration results of a brightened paper

Like the light scattering model, the parameters of the electrophotographic model are estimated by minimizing the deviations between the spectral predictions and the corresponding measurements. As illustrated in figure 9.1, the electrophotographic model is calibrated by presenting the measured spectra of the calibration samples, group by group, as an optimization goal to the constrained non-linear optimization routines[1] of Matlab™. Figure 9.1 depicts the individually obtained spectral optimization performances for the calibration patch set reaching a maximum spectral *RMS* deviation of as little as 2.1 %. The obtained optimization colorimetric *mean* error equals 2.22 ΔE^*_{94}, its *median* equals 1.67 ΔE^*_{94} and its *maximum* reaches 8.30 ΔE^*_{94}.

9.2 Model evaluations for a particular printer

Test samples

Once the optimization is completed, the obtained model parameters are fixed to the fitted values (a numerical list of the obtained parameters is given in appendix B). In order to analyze the prediction performance of the electrophotographic simulation model, the spectral reflectance of 1728 different samples of a *test chart* is computed and compared with common spectral measurements of the corresponding prints. The test chart is printed independently from the calibration samples of section 9.1 and comprises color halftone patches spanning the entire printable *CMY* color gamut. The patches are organized as a three-dimensional wedge with the twelve intermediate levels {0, 3.1, 6.5, 10.1, 14.0, 18.3, 23.1, 28.6, 35.1, 43.4, 55.0

[1] The implemented calibration approach needs about two days computation time of a contemporary 1 *GHz*, 500 *MB* Intel® -based dual processor computer.

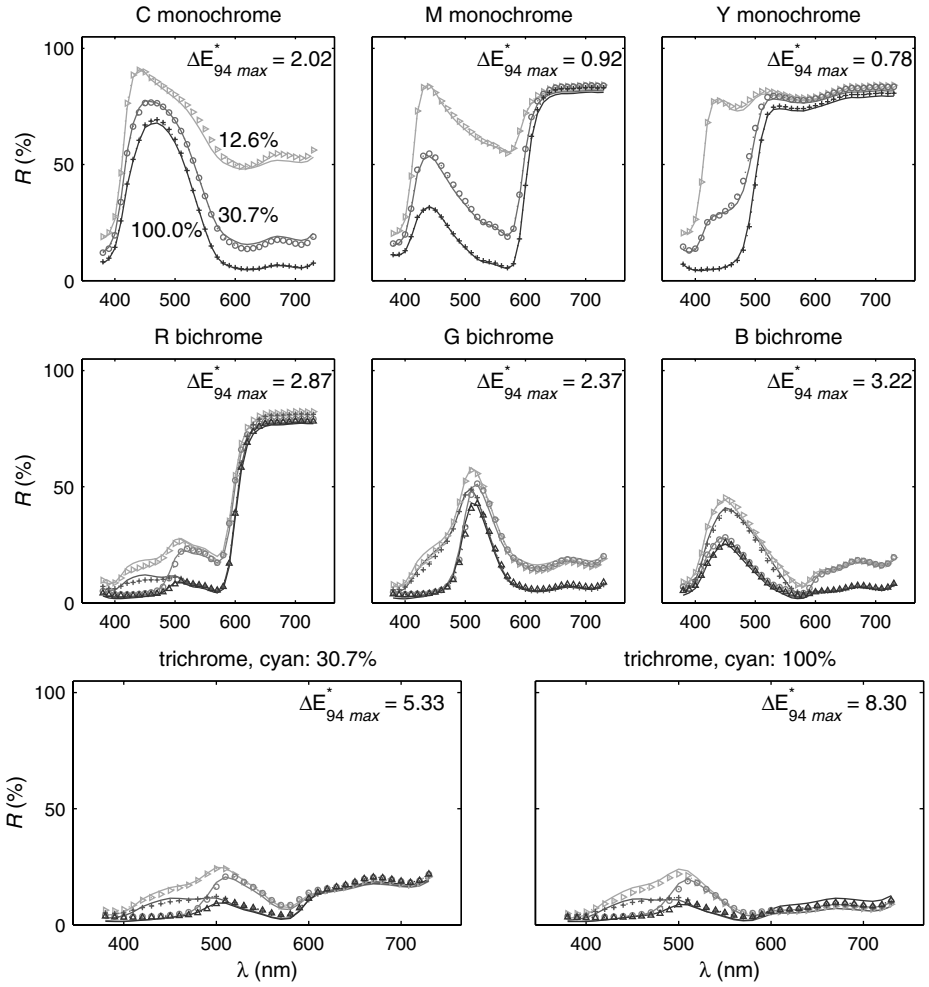

Figure 9.1: Optimization performance of the electrophotographic simulation model for the calibration patch set (learning set). The single graphs correspond to the individual calibration groups. The predictions are depicted by the marked lines, and the measurements by the solid lines. The area coverage of the individual primary colors was 12.6, 30.7 and 100.0 % and their respective combinations respectively.

and 100.0 %} of each primary color. This yields the above-mentioned total of 1728 different monochromatic, bichromatic and trichromatic color halftone patches. The halftoning algorithm for the test samples was based on an *error diffusion* algorithm filling the space according to a Hilbert path [Kan99]. The printer used for the tests was a 600 *dpi* Tektronix™ Phaser 560 laser desktop printer employing *CMY&K* as primary colors.

9.2.1 Colorimetric printer repeatability

The *repeatability* of the used printer, i.e. its ability to accurately reproduce a given color, plays a major role in the analysis of the prediction performance. In order to estimate the printer repeatability, the introduced test chart with the 1728 patches was printed and measured independently three times. The average spec-

tral reflectance of each patch was obtained as a mean value of five subsequent measurements at slightly varied spatial spots. The *Gretag-Macbeth™ SpectroScan T* with a black backing was used for the measurements without additional optical filters. This spectrophotometer claims a *colorimetric accuracy* of 0.4 ΔE^*_{ab} and a short-time *repeatability* of 0.02 ΔE^*_{ab}. For homogenous color, the repeatability is defined as the standard deviation of 10 measurements over 10 seconds.

Given the spectral measurements of the test chart, the printer repeatability is expressed as the average colorimetric deviation between the individual reproductions. Figure 9.2 illustrates the obtained reproduction error statistics given in ΔE^*_{94} units. The right graph facilitates the reading of the maximum reproduction

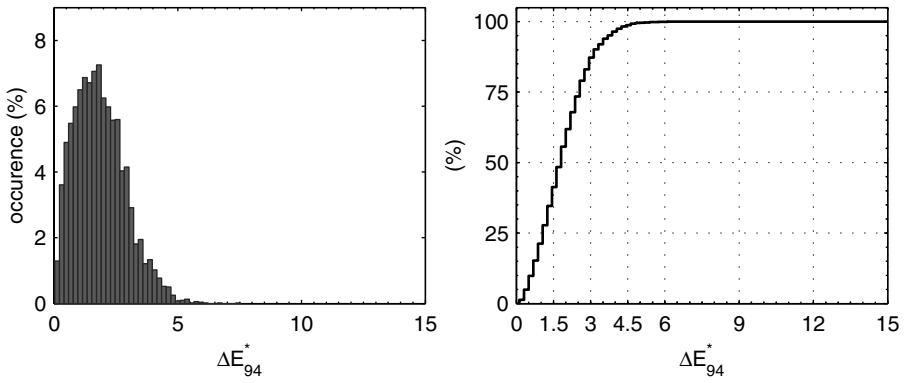

Figure 9.2: Colorimetric printer repeatability *Left side*: colorimetric deviation histogram illustrating the measurement statistics of three independent prints of the same test samples comprising 1728 different patches. *Right side*: cumulative sum representation of the same histogram, which allows to read the maximum expected error at a given percentage of the whole printer gamut.

error for a given percentage of all test samples. As an example, 50 % of the patches are reproduced with a colorimetric deviation of less than 1.6 ΔE^*_{94}, representing the *median* of the reproduction accuracy. This median represents an error only 1/10 lower than the prediction presented in section 9.1.1.

9.2.2 Prediction performance of a test set (1928 patches)

The prediction performance of the model is quantified by comparing the measured and predicted reflectance spectra of the various patches of the test chart. The predictions are also compared with the obtained performance of the classical halftone models reviewed in chapter 5. The classical models were adequately calibrated obtaining a fair comparison with the presented model. Among all classical models, the Yule–Nielsen corrected spectral Neugebauer equation (5.15), with fitted area coverages $a_{t\,fit}$ and a fitted n-value, performed best within the entire printer gamut. Therefore, it was chosen hereinafter as a reference for the performance of the classical models. Comparing the model predictions with the various test chart measurements yields a *worst*, an *average* and a *best* case performance. All of them are depicted in figure 9.3 in addition to the performance of the

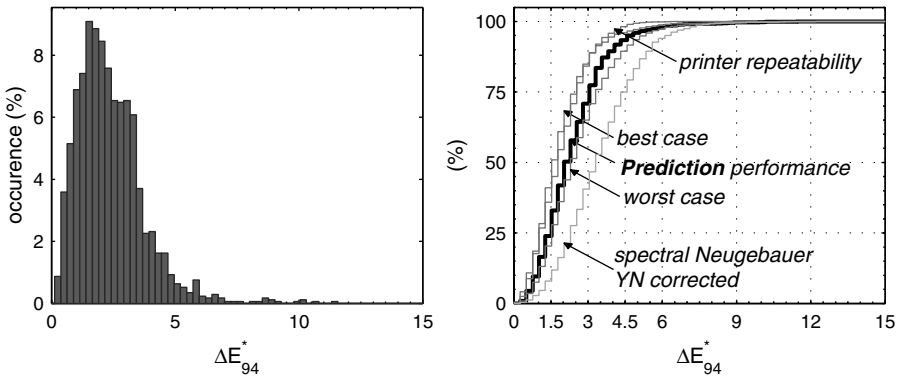

Figure 9.3: Prediction benchmark of color halftone prints on the *brightened* ColorCopy™paper. *Left side*: histogram of the best-case predictions of the test samples. *Right side*: cumulative sum representation of the same histogram in addition to the average and the worst-case prediction as well as the printer repeatability and the performance of the classical model. The bold line represents the average prediction performance.

classical model and the corresponding printer repeatability of figure 9.2. For the prediction model, including the effect of fluorescence (section 7.2.2), the average predication error equals $2.38\,\Delta E^*_{94}$, its median is $2.16\,\Delta E^*_{94}$ and its maximum is $11.38\,\Delta E^*_{94}$.

Up to now, the considered paper type was the brightened *ColorCopy*™, which is a paper optimized for desktop publishing applications. To complete the picture, figure 9.4 illustrates the performance obtained for the non-brightened APCO II/II paper. It is a paper of a higher strength, and the electrophotographic model experiences more convergence and prediction difficulties than with the optimized office paper. Accordingly, the prediction could not reach the same accuracy. Its average error equals $3.13\,\Delta E^*_{94}$, its median is $2.74\,\Delta E^*_{94}$ and its maximum is $19.57\,\Delta E^*_{94}$.

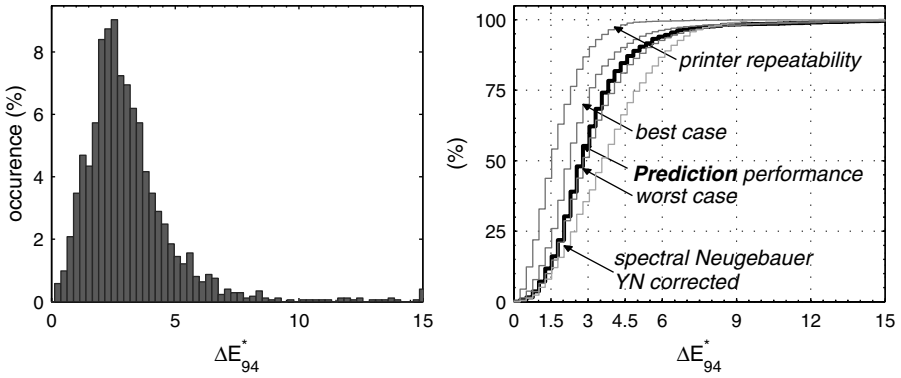

Figure 9.4: Prediction benchmark for the *non-brightened* APCO II/II paper compared with the corresponding printer repeatability and the performance of the classical models.

Generally, the performance of a calibrated system prediction model cannot be expected to overtake the reproduction repeatability of the system itself. Hence, the comparisons clearly demonstrate the accuracy potential of the applied concepts.

However, combined with the understanding of the underlying processes, the comparisons also demonstrate the obvious difficulty of obtaining a consistent, highly accurate electrophotographic printer model.

9.3 Impact of ignoring the paper brighteners

Considering the possibility of ignoring the fluorescent spectrum of a brightened paper. For instance, a light scattering model is considered to be calibrated if it uses the same data as presented in figure 7.5 but completely ignoring the fluorescent spectrum. Despite the fact that the light scattering model assumed a non-brightened paper, it succeeded in estimating a parameter set that was, however, less accurate. In particular, the fitting of the light scattering model transmittance spectra (section 7.2.2) failed to match and the maximum colorimetric deviation persisted at $7.02\,\Delta E^*_{94}$. Nevertheless, the prediction of the reflectance measurements on the black and white backing yielded an accuracy of $2.32\,\Delta E^*_{94}$. However, as presumed in section 6.1.1, the combined models fail to predict the achieved halftone colors accurately as presented in figure 9.5. To recall, as soon as the paper is covered by colors that absorb a certain amount of the excitation radiation, the paper whiteness beneath the print attenuates and becomes yellow-

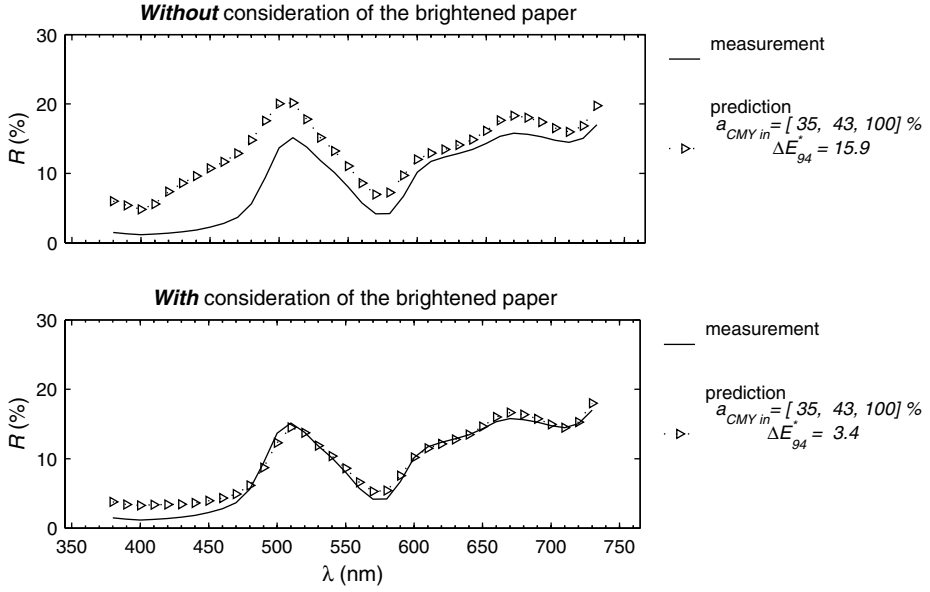

Figure 9.5: *Upper graph*: spectral illustration of the resulting blue shift that arises from ignoring the fluorescent spectrum and its excitation barrier. The predictions are depicted by the marked lines and the measurements by the solid lines. *Lower graph*: comparison graph illustrating the predictions of the same halftone patches obtained with the calibrated model of figure 9.3.

Bluish prediction shift

ish again. A model that ignores this effect would always predict a bright paper yielding an intractable *bluish prediction shift*. It is clearly apparent in the upper graph of the figure 9.5 at the wavelengths between 400 and 500 *nm*. The average shift Δb^* reaches 3.95 units towards blue compared with just 0.52 units of the well

calibrated models. In comparison, the average ΔL^* and Δa^* are in both cases less than 1 and hence negligible.

9.4 Three-dimensional visualization of a toner profile

Certainly one of the important intermediate results is the predicted microscopic relief $\delta_F(x, y)$ of the fused toner residing at the top of a paper surface. It is obtained from the fusing equation (8.14). Applying equations (8.16) and (6.33), each pixel

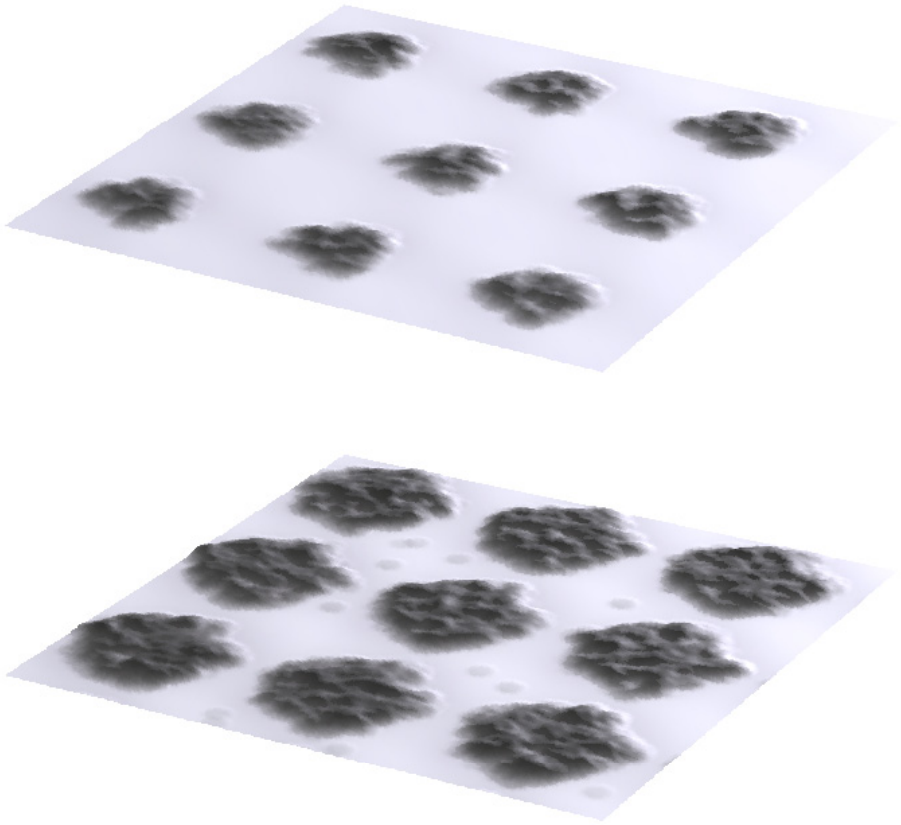

Figure 9.6: Two simulated microscopic toner profiles of clustered dot halftones. The halftone area coverages are 10 and 30 % respectively. Each illustrated area has a dimension of $1 \times 1\,mm$ and is illuminated from the rear right corner.

is accurately colored by the estimated point spectral reflectance $\hat{R}_\lambda(x, y)$. As an example, figure 9.6 illustrates two halftone patches at different area coverages. The applied halftoning scheme follows the classical clustered dot approach described in [Kan99]. As a result of the combined models, the obtained visualization takes into account the electrophotographic characteristics of the printer as well as the light scattering effect within the paper substrate.

10 Conclusion

The visual appearance of printed media is determined by the underlying physical phenomena, i.e. spectral light absorption and scattering. Knowing and controlling the characteristics of a printing process is essential in order to correctly reproduce an initial image. Dot gain mainly affects the reproduction accuracy and is divided into a mechanical and an optical dot gain. *Physical* dot gain is caused by the dot formation and the deposition properties of inks or toner on the printing substrate. *Optical* dot gain is due to lateral scattering of light within the bulk of paper and due to internal reflections within the coatings. As a first insight, the thesis analyzes the incident lateral light scattering through the paper substrate, as the main reason for optical dot gain.

A second insight explains how fluorescent agents added to most paper substrates may accentuate the halftone reproduction non-linearity. Activated by the invisible ultraviolet light, the fluorescent additives emit blue light, compensating for the yellowish appearance of natural paper fibers. The emission occurs diffusely in all space directions and amplifies the effects of the optical dot gain within the blue wavelength range. Furthermore, the excitation energy depends on the printed ink layers, which may filter the incident light yielding a reduced fluorescence emission.

By taking into account lateral scattering, multiple reflections and paper fluorescence, this thesis presents a comprehensive mathematical model for the analysis of the optical dot gain effects on halftone prints. It is based on the main contributing physical phenomena. The lateral scattering model relies on a 3D differential equation system describing the scattering of light in space. The spectral model takes into account the effect of fluorescent agents added to the substrate of common papers. The derived solution is a closed analytical equation described in the Fourier domain. The obtained equation makes it possible to compute the spectral point reflectance of arbitrary halftone prints as a function of the spectral point transmittance of the corresponding color layer combinations.

When properly considering optical interreflections within the two interfaces of a paper sheet, the model permits an accurate calibration for any particular combination of paper and inks. With the assumption of isotropic light scattering within paper, halftone reproductions can be characterized without explicit optical dot gain measurements. Spectral reflectance and transmittance measurements of simple solid patches are sufficient for the characterization of the relevant optical properties of common papers.

The presented light scattering model makes it possible to predict the spatial properties of halftone prints. Using comparative microscopic spectral measurements, the model was qualitatively verified. Thanks to the calibrated model, the thesis presents demonstrative microscopic simulations of arbitrary halftone samples at various spatial scales. The simulations create the bridge between the macroscopic structures and the macroscopic appearance.

The light scattering model is used to predict the reflectance spectra of color halftone patches printed on a dry toner electrophotographic desktop printer. The newly introduced mechanical dot gain model simulates the characteristic dot formation of electrophotographic printers and computes the point transmittances of any given input image. Calibrated with the spectral measurements of only 30 calibration halftone patches, the aggregation of both models is able to predict the full color response of the considered printer-paper combination. The obtained prediction errors were close to the general printer repeatability, confirming an excellent agreement between theory and measurements.

The thesis proposes a new fundamental framework for prospective developments of color halftone printing systems. Using the proposed model, paper manufacturers are now able to accurately characterize the optical properties of their products. Moreover, it is now possible to introduce easier printer calibration procedures. The groundwork introduced by the thesis offers the possibility of conceiving novel, user friendlier and self-calibrating color halftone printer control systems.

Mathematical appendix

A Lateral light scattering model

The complexity of the light scattering model was reduced by applying a systematic replacement of the coefficients of the radiant fluxes with simple constants. The obtained substitutions for the cartesian equation system are listed in appendix A.1. The derivation of the cartesian solution given in chapter 6 is presented in appendix A.2. Finally, as the whole light scattering analysis in polar coordinates is identical to the cartesian analysis, the detailed presentation of the polar coordinates equation system is moved from the main part of the thesis to appendix A.3.

A.1 Substitution list of the cartesian model

The following substitutions are introduced in order to obtain the simplified differential equation system (6.20) and (6.21). The substitutions were carried out using MATHEMATICA®.

$$c_{\chi\psi,\lambda} = \sqrt{a^2_{21_{\chi\psi,\lambda}} - a^2_{12_{\chi\psi,\lambda}}} \,, \tag{A.1}$$

$$a_{12_{\chi\psi,\lambda}} = \frac{s_{2_{\chi\psi,\lambda}}}{s_{1_{\chi\psi,\lambda}}} \,, \tag{A.2}$$

$$a_{21_{\chi\psi,\lambda}} = \frac{s_{3_{\chi\psi,\lambda}}}{s_{1_{\chi\psi,\lambda}}} \,, \tag{A.3}$$

$$
\begin{aligned}
s_{1_{\chi\psi,\lambda}} = {} & q_{1_{\chi\psi,\lambda}}^{4} + q_{3_{\chi\psi,\lambda}} \cdot q_{4_{\chi\psi,\lambda}} \cdot q_{5_{\chi\psi,\lambda}} \cdot q_{6_{\chi\psi,\lambda}} + \Big(2 \cdot \Big(q_{3_{\chi\psi,\lambda}} + q_{4_{\chi\psi,\lambda}} + q_{5_{\chi\psi,\lambda}} + q_{6_{\chi\psi,\lambda}} \Big) \cdot q_{1_{\chi\psi,\lambda}} - \\
& \Big(q_{3_{\chi\psi,\lambda}} + q_{4_{\chi\psi,\lambda}} \Big) \cdot \Big(q_{5_{\chi\psi,\lambda}} + q_{6_{\chi\psi,\lambda}} \Big) \Big) \cdot q_{7_{\chi\psi,\lambda}}^{2} - \\
& \Big(q_{3_{\chi\psi,\lambda}} \cdot q_{4_{\chi\psi,\lambda}} + q_{5_{\chi\psi,\lambda}} \cdot q_{6_{\chi\psi,\lambda}} + 4 \cdot q_{7_{\chi\psi,\lambda}}^{2} \Big) \cdot q_{1_{\chi\psi,\lambda}}^{2} \,, \qquad \text{(A.4)}
\end{aligned}
$$

$$
\begin{aligned}
s_{2_{\chi\psi,\lambda}} = {} & -\Big(q_{1_{\chi\psi,\lambda}}^{2} - q_{3_{\chi\psi,\lambda}} \cdot q_{4_{\chi\psi,\lambda}} \Big) \cdot \Big(q_{1_{\chi\psi,\lambda}}^{2} - q_{5_{\chi\psi,\lambda}} \cdot q_{6_{\chi\psi,\lambda}} \Big) \cdot q_{1_{\chi\psi,\lambda}} + \\
& \Big(8 \cdot q_{1_{\chi\psi,\lambda}}^{3} + q_{3_{\chi\psi,\lambda}} \cdot q_{4_{\chi\psi,\lambda}} \cdot q_{5_{\chi\psi,\lambda}} + q_{4_{\chi\psi,\lambda}} \cdot q_{5_{\chi\psi,\lambda}} \cdot q_{6_{\chi\psi,\lambda}} + \Big(q_{4_{\chi\psi,\lambda}} + q_{5_{\chi\psi,\lambda}} \Big) \cdot q_{3_{\chi\psi,\lambda}} \cdot q_{6_{\chi\psi,\lambda}} - \\
& 3 \cdot \Big(q_{3_{\chi\psi,\lambda}} + q_{4_{\chi\psi,\lambda}} + q_{5_{\chi\psi,\lambda}} + q_{6_{\chi\psi,\lambda}} \Big) \cdot q_{1_{\chi\psi,\lambda}}^{2} + \Big(-2 \cdot q_{5_{\chi\psi,\lambda}} \cdot q_{6_{\chi\psi,\lambda}} + \\
& \Big(q_{5_{\chi\psi,\lambda}} + q_{6_{\chi\psi,\lambda}} \Big) \cdot q_{4_{\chi\psi,\lambda}} + \Big(q_{5_{\chi\psi,\lambda}} + q_{6_{\chi\psi,\lambda}} - 2 \cdot q_{4_{\chi\psi,\lambda}} \Big) \cdot q_{3_{\chi\psi,\lambda}} \Big) \cdot q_{1_{\chi\psi,\lambda}} \Big) \cdot q_{7_{\chi\psi,\lambda}}^{2} - \\
& 2 \cdot \Big(2 \cdot q_{1_{\chi\psi,\lambda}} - q_{3_{\chi\psi,\lambda}} - q_{4_{\chi\psi,\lambda}} \Big) \cdot \Big(2 \cdot q_{1_{\chi\psi,\lambda}} - q_{5_{\chi\psi,\lambda}} - q_{6_{\chi\psi,\lambda}} \Big) \cdot q_{7_{\chi\psi,\lambda}}^{3} \,, \qquad \text{(A.5)}
\end{aligned}
$$

$$
\begin{aligned}
s_{3_{\chi\psi,\lambda}} = {} & -\Big(q_{1_{\chi\psi,\lambda}}^{2} - q_{3_{\chi\psi,\lambda}} \cdot q_{4_{\chi\psi,\lambda}} \Big) \cdot \Big(q_{1_{\chi\psi,\lambda}}^{2} - q_{5_{\chi\psi,\lambda}} \cdot q_{6_{\chi\psi,\lambda}} \Big) \cdot q_{2_{\chi\psi,\lambda}} + \\
& \Big(4 \cdot q_{1_{\chi\psi,\lambda}}^{3} + \Big(4 \cdot q_{2_{\chi\psi,\lambda}} - q_{3_{\chi\psi,\lambda}} - q_{4_{\chi\psi,\lambda}} - q_{5_{\chi\psi,\lambda}} - q_{6_{\chi\psi,\lambda}} \Big) \cdot q_{1_{\chi\psi,\lambda}}^{2} + \\
& q_{4_{\chi\psi,\lambda}} \cdot q_{5_{\chi\psi,\lambda}} \cdot q_{6_{\chi\psi,\lambda}} + \Big(q_{3_{\chi\psi,\lambda}} + q_{4_{\chi\psi,\lambda}} \Big) \cdot \Big(q_{5_{\chi\psi,\lambda}} + q_{6_{\chi\psi,\lambda}} \Big) \cdot q_{2_{\chi\psi,\lambda}} + \\
& \Big(q_{5_{\chi\psi,\lambda}} \cdot q_{6_{\chi\psi,\lambda}} + \Big(q_{5_{\chi\psi,\lambda}} + q_{6_{\chi\psi,\lambda}} \Big) \cdot q_{4_{\chi\psi,\lambda}} \Big) \cdot q_{3_{\chi\psi,\lambda}} - \\
& 2 \cdot \Big(q_{3_{\chi\psi,\lambda}} \cdot q_{4_{\chi\psi,\lambda}} + q_{5_{\chi\psi,\lambda}} \cdot q_{6_{\chi\psi,\lambda}} + \Big(q_{3_{\chi\psi,\lambda}} + q_{4_{\chi\psi,\lambda}} + q_{5_{\chi\psi,\lambda}} + q_{6_{\chi\psi,\lambda}} \Big) \cdot q_{2_{\chi\psi,\lambda}} \Big) \cdot q_{1_{\chi\psi,\lambda}} \Big) \cdot q_{7_{\chi\psi,\lambda}}^{2} - \\
& 2 \cdot \Big(2 \cdot q_{1_{\chi\psi,\lambda}} - q_{3_{\chi\psi,\lambda}} - q_{4_{\chi\psi,\lambda}} \Big) \cdot \Big(2 \cdot q_{1_{\chi\psi,\lambda}} - q_{5_{\chi\psi,\lambda}} - q_{6_{\chi\psi,\lambda}} \Big) \cdot q_{7_{\chi\psi,\lambda}}^{3} \,, \qquad \text{(A.6)}
\end{aligned}
$$

$$
q_{1_{\chi\psi,\lambda}} = \phi_{f_\lambda} + \sigma_{r_\lambda} \,, \qquad \text{(A.7)}
$$

$$
q_{2_{\chi\psi,\lambda}} = \phi_{f_\lambda} - \alpha_\lambda - \sigma_{r_\lambda} - 4 \cdot \sigma_{s_\lambda} \,, \qquad \text{(A.8)}
$$

$$
q_{3_{\chi\psi,\lambda}} = q_{2_{\chi\psi,\lambda}} - 2\,\pi\,\mathbf{i} \cdot \chi \,, \qquad \text{(A.9)}
$$

$$
q_{4_{\chi\psi,\lambda}} = q_{2_{\chi\psi,\lambda}} + 2\,\pi\,\mathbf{i} \cdot \chi \,, \qquad \text{(A.10)}
$$

$$
q_{5_{\chi\psi,\lambda}} = q_{2_{\chi\psi,\lambda}} - 2\,\pi\,\mathbf{i} \cdot \psi \,, \qquad \text{(A.11)}
$$

$$
q_{6_{\chi\psi,\lambda}} = q_{2_{\chi\psi,\lambda}} + 2\,\pi\,\mathbf{i} \cdot \psi \,, \qquad \text{(A.12)}
$$

$$
q_{7_{\chi\psi,\lambda}} = \phi_{f_\lambda} + \sigma_{s_\lambda} \,. \qquad \text{(A.13)}
$$

A.1.1 Singular cartesian case

Applying the singular relation given in eq. (7.1) reduces the substitution eq. (A.4)–(A.13) as follows

$$s_{1_{00,\lambda}} = \left(q_{1_{00,\lambda}} - q_{2_{00,\lambda}}\right)^2 \cdot \left(\left(q_{1_{00,\lambda}} + q_{2_{00,\lambda}}\right)^2 - 4 \cdot q_{7_{00,\lambda}}^2\right), \tag{A.14}$$

$$s_{2_{00,\lambda}} = -\left(q_{1_{00,\lambda}} - q_{2_{00,\lambda}}\right)^2 \cdot \left(q_{1_{00,\lambda}} + q_{2_{00,\lambda}} - 2 \cdot q_{7_{00,\lambda}}\right) \cdot \left(\left(q_{1_{00,\lambda}} + q_{2_{00,\lambda}}\right) \cdot q_{1_{00,\lambda}} + 2 \cdot q_{1_{00,\lambda}} \cdot q_{7_{00,\lambda}} - 4 \cdot q_{7_{00,\lambda}}^2\right), \tag{A.15}$$

$$s_{3_{00,\lambda}} = -\left(q_{1_{00,\lambda}} - q_{2_{00,\lambda}}\right)^2 \cdot \left(q_{1_{00,\lambda}} + q_{2_{00,\lambda}} - 2 \cdot q_{7_{00,\lambda}}\right) \cdot \left(\left(q_{1_{00,\lambda}} + q_{2_{00,\lambda}}\right) \cdot q_{2_{00,\lambda}} + 2 \cdot q_{2_{00,\lambda}} \cdot q_{7_{00,\lambda}} - 4 \cdot q_{7_{00,\lambda}}^2\right), \tag{A.16}$$

$$q_{1_{00,\lambda}} = \phi_{f_\lambda} + \sigma_{r_\lambda}\ , \tag{A.17}$$

$$q_{2_{00,\lambda}} = \phi_{f_\lambda} - \alpha_\lambda - \sigma_{r_\lambda} - 4 \cdot \sigma_{s_\lambda}\ , \tag{A.18}$$

$$q_{7_{00,\lambda}} = \phi_{f_\lambda} + \sigma_{s_\lambda}\ . \tag{A.19}$$

A.2 Solving the boundary condition problem

For simplicity's sake, the lateral and the wavelength dependencies (χ, ψ) and λ of the radiant fluxes are omitted, and the equations (6.20) and (6.21) are rewritten as

$$\frac{\partial \mathcal{I}(z)}{\partial z} = a_{12} \cdot \mathcal{J}(z) + a_{21} \cdot \mathcal{I}(z)\ , \tag{A.20}$$

$$-\frac{\partial \mathcal{J}(z)}{\partial z} = a_{12} \cdot \mathcal{I}(z) + a_{21} \cdot \mathcal{J}(z)\ . \tag{A.21}$$

By rearranging equation (A.21) one obtains

$$\mathcal{I}(z) = -\frac{1}{a_{12}} \cdot \left(a_{21} \cdot \mathcal{J}(z) + \frac{\partial \mathcal{J}(z)}{\partial z}\right) \tag{A.22}$$

which combined with equation (A.20) yields the differential equation

$$\frac{\partial^2 \mathcal{J}(z)}{\partial z^2} = \left(a_{21}^2 - a_{12}^2\right) \cdot \mathcal{J}(z)\ . \tag{A.23}$$

Equation (A.23) is directly solved by applying the methods of calculus [BS97] yielding the integration solution of the emerging flux

$$\mathcal{J}(z) = C_1 \cdot e^{-z\sqrt{a_{21}^2 - a_{12}^2}} + C_2 \cdot e^{z\sqrt{a_{21}^2 - a_{12}^2}}\ , \tag{A.24}$$

where C_1 and C_2 are the constants of integration. Setting this solution back into equation (A.22) yields the solution for the incident flux

$$\mathcal{I}(z) = \frac{e^{-z\sqrt{a_{21}^2-a_{12}^2}}}{a_{12}} \times \left(\left(C_1 - C_2 \cdot e^{2z\sqrt{a_{21}^2-a_{12}^2}}\right)\cdot\sqrt{a_{21}^2-a_{12}^2} - \left(C_1 + C_2 \cdot e^{2z\sqrt{a_{21}^2-a_{12}^2}}\right)\cdot a_{21}\right). \tag{A.25}$$

The constants of integration C_1 and C_2 are solved by applying the illuminating conditions at the top and bottom interfaces given in equations (6.28) and (6.29). However, before being applied, these equations must be transformed into the Fourier domain yielding

$$\mathcal{I}_\lambda(\chi,\psi,D) = \tau_{ap_\lambda}(\chi,\psi) ** i_{0_\lambda}\ , \tag{A.26}$$

using the *convolution theorem* of the Fourier transform [Bra00, p. 117]. Accordingly, $\mathcal{J}_\lambda(\chi,\psi,0)$ is related with the constant transmittance illumination j_{0_λ} by

$$\mathcal{J}_\lambda(\chi,\psi,0) = \rho_{pb_\lambda}\cdot\mathcal{I}_\lambda(\chi,\psi,0) + \tau_{bp_\lambda} ** j_{0_\lambda}\ , \tag{A.27}$$

with the backing-paper reflectance ρ_{pb_λ} that reflects any flux reaching the bottom of the light scattering substrate. Henceforth, the dependencies (χ,ψ) and λ are omitted again after this short insertion.

Applying equations (A.26) and (A.27) to equations (A.24) and (A.25) and using the substitution (A.1) yields the constants of integration

$$C_1 = \frac{\left(a_{12} + \left(c + a_{21}\right)\cdot\rho_{pb}\right)\cdot e^{Dc}\cdot\tau_{ap} ** i_0 + \left(c + a_{21}\right)\cdot e^{2Dc}\cdot\tau_{bp} ** j_0}{c - a_{21} - a_{12}\cdot\rho_{pb} + \left(c + a_{21} + a_{12}\cdot\rho_{pb}\right)\cdot e^{2Dc}} \tag{A.28}$$

$$C_2 = \frac{\left(-a_{12} + \left(c - a_{21}\right)\cdot\rho_{pb}\right)\cdot e^{Dc}\cdot\tau_{ap} ** i_0 + \left(c - a_{21}\right)\cdot\tau_{bp} ** j_0}{c - a_{21} - a_{12}\cdot\rho_{pb} + \left(c + a_{21} + a_{12}\cdot\rho_{pb}\right)\cdot e^{2Dc}} \tag{A.29}$$

Substituting the right-hand side of equations (A.28) and (A.29) for the constants of integration C_1 and C_2 in equation (A.24) yields the general solution of $\mathcal{J}(z)$

$$\mathcal{J}(z) = \frac{\left(a_{12} + \left(c + a_{21}\right)\cdot\rho_{pb}\right)\cdot e^{Dc} + \left(-a_{12} + \left(c - a_{21}\right)\cdot\rho_{pb}\right)\cdot e^{(2z+D)c}}{\left(c - a_{21} - a_{12}\cdot\rho_{pb}\right)\cdot e^{zc} + \left(c + a_{21} + a_{12}\cdot\rho_{pb}\right)\cdot e^{(2D+z)c}}\cdot\tau_{ap} ** i_0 + \frac{\left(c - a_{21}\right)\cdot e^{2zc} + \left(c + a_{21}\right)\cdot e^{2Dc}}{\left(c - a_{21} - a_{12}\cdot\rho_{pb}\right)\cdot e^{zc} + \left(c + a_{21} + a_{12}\cdot\rho_{pb}\right)\cdot e^{(2D+z)c}}\cdot\tau_{bp} ** j_0\ . \tag{A.30}$$

As introduced in section 6.3.3, the obtained solution of $\mathcal{J}(z)$ describes the general modulation transfer function (MTF) of a diffuse light scattering medium. Applying the measurement equation (6.30) and (6.31) to this general solution easily leads to the transmittance and reflectance equations (6.32) and (6.33).

A.3 Light scattering in polar coordinates

The analysis of the scattering light in a polar coordinate system is conducted similarly to the analysis presented in section 6.2.1. Let r and z be the radial and the vertical coordinates. The azimuth θ is neglected, due to circular symmetry. As illustrated in figure 6.2, the spectral analysis of the downward and upward oriented fluxes (i_λ, j_λ) as well as the of the lateral ones (p_λ, q_λ) is applied on a cylindrical ring of a paper sheet with a total thickness D

$$\begin{aligned} i_\lambda(r,z)\cdot 2\pi r\cdot \mathrm{d}r = i_\lambda(r,z+\mathrm{d}z)\cdot 2\pi r\cdot \mathrm{d}r + \Big[&\left(\phi_{f_\lambda}+\sigma_{ji_\lambda}\right)\cdot j_\lambda(r,z) + \\ &\left(\phi_{f_\lambda}-\phi_{e_\lambda}-\alpha_\lambda-\sigma_{ij_\lambda}-\sigma_{ip_\lambda}-\sigma_{iq_\lambda}\right)\cdot i_\lambda(r,z+\mathrm{d}z) + \\ &\left(\phi_{f_\lambda}+\sigma_{pi_\lambda}\right)\cdot p_\lambda(r,z) + \left(\phi_{f_\lambda}+\sigma_{qi_\lambda}\right)\cdot q_\lambda(r+\mathrm{d}r,z)\Big]\cdot 2\pi r\cdot \mathrm{d}r\mathrm{d}z\ , \end{aligned} \tag{A.31}$$

$$\begin{aligned} j_\lambda(r,z+\mathrm{d}z)\cdot 2\pi r\cdot \mathrm{d}r = j_\lambda(r,z)\cdot 2\pi r\cdot \mathrm{d}r + \Big[&\left(\phi_{f_\lambda}+\sigma_{ij_\lambda}\right)\cdot i_\lambda(r,z+\mathrm{d}z) + \\ &\left(\phi_{f_\lambda}-\phi_{e_\lambda}-\alpha_\lambda-\sigma_{ji_\lambda}-\sigma_{jp_\lambda}-\sigma_{jq_\lambda}\right)\cdot j_\lambda(r,z) + \\ &\left(\phi_{f_\lambda}+\sigma_{pj_\lambda}\right)\cdot p_\lambda(r,z) + \left(\phi_{f_\lambda}+\sigma_{qj_\lambda}\right)\cdot q_\lambda(r+\mathrm{d}r,z)\Big]\cdot 2\pi r\cdot \mathrm{d}r\mathrm{d}z\ , \end{aligned} \tag{A.32}$$

$$\begin{aligned} p_\lambda(r+\mathrm{d}r,z)\cdot 2\pi r\cdot \mathrm{d}z = p_\lambda(r,z)\cdot 2\pi r\cdot \mathrm{d}z + \Big[&\left(\phi_{f_\lambda}+\sigma_{qp_\lambda}\right)\cdot q_\lambda(r+\mathrm{d}r,z) + \\ &\left(\phi_{f_\lambda}-\phi_{e_\lambda}-\alpha_\lambda-\sigma_{pq_\lambda}-\sigma_{pi_\lambda}-\sigma_{pj_\lambda}\right)\cdot p_\lambda(r,z) + \\ &\left(\phi_{f_\lambda}+\sigma_{ip_\lambda}\right)\cdot i_\lambda(r,z+\mathrm{d}z) + \left(\phi_{f_\lambda}+\sigma_{jp_\lambda}\right)\cdot j_\lambda(r,z)\Big]\cdot 2\pi r\cdot \mathrm{d}r\mathrm{d}z\ , \end{aligned} \tag{A.33}$$

$$\begin{aligned} q_\lambda(r,z)\cdot 2\pi r\cdot \mathrm{d}z = q_\lambda(r+\mathrm{d}r,z)\cdot 2\pi r\cdot \mathrm{d}z + \Big[&\left(\phi_{f_\lambda}+\sigma_{pq_\lambda}\right)\cdot p_\lambda(r,z) + \\ &\left(\phi_{f_\lambda}-\phi_{e_\lambda}-\alpha_\lambda-\sigma_{qp_\lambda}-\sigma_{qi_\lambda}-\sigma_{qj_\lambda}\right)\cdot q_\lambda(r+\mathrm{d}r,z) + \\ &\left(\phi_{f_\lambda}+\sigma_{iq_\lambda}\right)\cdot i_\lambda(r,z+\mathrm{d}z) + \left(\phi_{f_\lambda}+\sigma_{jq_\lambda}\right)\cdot j_\lambda(r,z)\Big]\cdot 2\pi r\cdot \mathrm{d}r\mathrm{d}z\ , \end{aligned} \tag{A.34}$$

where α_λ and $\sigma_{x_1x_2\,\lambda}$ are the specific spectral absorption and scattering coefficient per unit $2\pi r\cdot \mathrm{d}r\mathrm{d}z$ volume respectively and, ϕ_{e_λ} and ϕ_{f_λ} are the normalized excitation and fluorescent spectra. According to section 6.2.1, the system of coupled partial linear differential equations is derived applying a Taylor series expansion along $r+\mathrm{d}r$ and $z+\mathrm{d}z$ yielding

$$\begin{aligned} \frac{\partial\, i_\lambda(r,z)}{\partial z} = &-\left(\phi_{f_\lambda}+\sigma_{ji_\lambda}\right)\cdot j_\lambda(r,z) - \\ &\left(\phi_{f_\lambda}-\alpha_\lambda-\sigma_{ij_\lambda}-\sigma_{ip_\lambda}-\sigma_{iq_\lambda}\right)\cdot i_\lambda(r,z) - \\ &\left(\phi_{f_\lambda}+\sigma_{pi_\lambda}\right)\cdot p_\lambda(r,z) - \left(\phi_{f_\lambda}+\sigma_{qi_\lambda}\right)\cdot q_\lambda(r,z)\ , \end{aligned} \tag{A.35}$$

$$\begin{aligned} \frac{\partial\, j_\lambda(r,z)}{\partial z} = &\left(\phi_{f_\lambda}+\sigma_{ij_\lambda}\right)\cdot i_\lambda(r,z) + \\ &\left(\phi_{f_\lambda}-\alpha_\lambda-\sigma_{ji_\lambda}-\sigma_{jp_\lambda}-\sigma_{jq_\lambda}\right)\cdot j_\lambda(r,z) + \\ &\left(\phi_{f_\lambda}+\sigma_{pj_\lambda}\right)\cdot p_\lambda(r,z) + \left(\phi_{f_\lambda}+\sigma_{qj_\lambda}\right)\cdot q_\lambda(r,z)\ , \end{aligned} \tag{A.36}$$

$$\frac{\partial p_\lambda(r,z)}{\partial x} = \left(\phi_{f_\lambda} + \sigma_{qp_\lambda}\right)\cdot q_\lambda(r,z) + \left(\phi_{f_\lambda} - \alpha_\lambda - \sigma_{pq_\lambda} - \sigma_{pi_\lambda} - \sigma_{pj_\lambda}\right)\cdot p_\lambda(r,z) + \left(\phi_{f_\lambda} + \sigma_{ip_\lambda}\right)\cdot i_\lambda(r,z) + \left(\phi_{f_\lambda} + \sigma_{jp_\lambda}\right)\cdot j_\lambda(r,z)\ , \tag{A.37}$$

$$\frac{\partial q_\lambda(r,z)}{\partial x} = -\left(\phi_{f_\lambda} + \sigma_{pq_\lambda}\right)\cdot p_\lambda(r,z) - \left(\phi_{f_\lambda} - \alpha_\lambda - \sigma_{qp_\lambda} - \sigma_{qi_\lambda} - \sigma_{qj_\lambda}\right)\cdot q_\lambda(r,z) - \left(\phi_{f_\lambda} + \sigma_{iq_\lambda}\right)\cdot i_\lambda(r,z) - \left(\phi_{f_\lambda} + \sigma_{jq_\lambda}\right)\cdot j_\lambda(r,z)\ . \tag{A.38}$$

Besides the fluorescent parameters ϕ_{f_λ}, equations (A.35)–(A.38) are mathematically of the same type as Berg's equations (9.1)–(9.4) [Ber97]. The application of a one-dimensional Fourier transform along the radial coordinate r changes the differential nature of both lateral equations (A.37) and (A.38) to common algebraic equations. Processing the transformed system algebraically with Mathematica® [Wol00] cancels the lateral equations and the equation systems are reduced to the following perpendicular Fourier transformed differential equations

$$\frac{\partial \mathcal{I}_\lambda(\rho,z)}{\partial z} = a_{12_{\rho,\lambda}}\cdot\mathcal{J}_\lambda(\rho,z) + a_{21_{\rho,\lambda}}\cdot\mathcal{I}_\lambda(\rho,z)\ , \tag{A.39}$$

$$-\frac{\partial \mathcal{J}_\lambda(\rho,z)}{\partial z} = a_{12_{\rho,\lambda}}\cdot\mathcal{I}_\lambda(\rho,z) + a_{21_{\rho,\lambda}}\cdot\mathcal{J}_\lambda(\rho,z)\ , \tag{A.40}$$

where $\mathcal{I}_\lambda(\rho,z)$ and $\mathcal{J}_\lambda(\rho,z)$ are the Fourier transform of the perpendicular fluxes $i_\lambda(r,z)$ and $j_\lambda(r,z)$. $a_{12_{\rho,\lambda}}$ and $a_{21_{\rho,\lambda}}$ are substitution constants given explicitly in appendix A.3.1. Finally the paper's modulation transfer function derived in a polar coordinate system is given according to section A.2 by

Transmittance MTF

$$T_\lambda(r) = \tau_{bp_\lambda}\cdot\mathcal{F}_r^{-1}\left[\ \mathcal{F}_r\left[\tau_{pa_\lambda}(r)\right]\ \times \frac{2\cdot c_{\rho,\lambda}\cdot e^{D\,c_{\rho,\lambda}}}{c_{\rho,\lambda} - a_{21_{\rho,\lambda}} - a_{12_{\rho,\lambda}}\cdot\rho_{pb_\lambda} + \left(c_{\rho,\lambda} + a_{21_{\rho,\lambda}} + a_{12_{\rho,\lambda}}\cdot\rho_{pb_\lambda}\right)\cdot e^{2\,D\,c_{\rho,\lambda}}}\ \right], \tag{A.41}$$

Reflectance MTF

$$R_\lambda(r) = \rho_{ap_\lambda}(r) + \tau_{ap_\lambda}(r)\cdot\mathcal{F}_r^{-1}\left[\ \mathcal{F}_r\left[\tau_{pa_\lambda}(r)\right]\ \times \frac{a_{12_{\rho,\lambda}} + \left(c_{\rho,\lambda} + a_{21_{\rho,\lambda}}\right)\cdot\rho_{pb_\lambda} + \left(-a_{12_{\rho,\lambda}} + \left(c_{\rho,\lambda} - a_{21_{\rho,\lambda}}\right)\cdot\rho_{pb_\lambda}\right)\cdot e^{2\,D\,c_{\rho,\lambda}}}{c_{\rho,\lambda} - a_{21_{\rho,\lambda}} - a_{12_{\rho,\lambda}}\cdot\rho_{pb_\lambda} + \left(c_{\rho,\lambda} + a_{21_{\rho,\lambda}} + a_{12_{\rho,\lambda}}\cdot\rho_{pb_\lambda}\right)\cdot e^{2\,D\,c_{\rho,\lambda}}}\ \right], \tag{A.42}$$

with $\mathcal{F}_r$ and $\mathcal{F}_r^{-1}$ the one-dimensional Fourier transform in r and its inverse. τ_{bp_λ}, ρ_{pb_λ}, $\tau_{pa_\lambda}(r)$, $\rho_{ap_\lambda}(r)$ and $\tau_{ap_\lambda}(r)$ are the boundary conditions corresponding to eq. (6.23)–(6.27) formulated in polar coordinates. The substitutions $c_{\rho,\lambda}$, $a_{12_{\rho,\lambda}}$ and $a_{21_{\rho,\lambda}}$ are given in appendix A.3.1.

A.3.1 Substitution list of the polar coordinates model

The substitutions introduced for the polar coordinates model applying the semi isotrope scattering approach introduced in section 6.2.1 are

$$c_{\rho,\lambda} = \sqrt{a_{21_{\rho,\lambda}}^2 - a_{12_{\rho,\lambda}}^2} \,, \tag{A.43}$$

$$a_{12_{\rho,\lambda}} = \frac{s_{2_{\rho,\lambda}}}{s_{1_{\rho,\lambda}}} \,, \tag{A.44}$$

$$a_{21_{\rho,\lambda}} = \frac{s_{3_{\rho,\lambda}}}{s_{1_{\rho,\lambda}}} \,, \tag{A.45}$$

$$s_{1_{\rho,\lambda}} = q_{1_{\rho,\lambda}}^2 - q_{3_{\rho,\lambda}} \cdot q_{4_{\rho,\lambda}} \,, \tag{A.46}$$

$$s_{2_{\rho,\lambda}} = -q_{1_{\rho,\lambda}}^3 - \left(q_{3_{\rho,\lambda}} + q_{4_{\rho,\lambda}}\right) \cdot q_{5_{\rho,\lambda}}^2 + \left(q_{3_{\rho,\lambda}} \cdot q_{4_{\rho,\lambda}} + 2 \cdot q_{5_{\rho,\lambda}}^2\right) \cdot q_{1_{\rho,\lambda}} \,, \tag{A.47}$$

$$s_{3_{\rho,\lambda}} = 2 \cdot q_{1_{\rho,\lambda}} \cdot q_{5_{\rho,\lambda}}^2 - \left(q_{3_{\rho,\lambda}} + q_{4_{\rho,\lambda}}\right) \cdot q_{5_{\rho,\lambda}}^2 - q_{2_{\rho,\lambda}} \cdot s_{1_{\rho,\lambda}} \,, \tag{A.48}$$

$$q_{1_{\rho,\lambda}} = \phi_{f_\lambda} + \sigma_{r_\lambda} \,, \tag{A.49}$$

$$q_{2_{\rho,\lambda}} = \phi_{f_\lambda} - \alpha_\lambda - \sigma_{r_\lambda} - 2 \cdot \sigma_{s_\lambda} \,, \tag{A.50}$$

$$q_{3_{\rho,\lambda}} = q_{2_{\rho,\lambda}} - 2\,\pi\,\mathbf{i} \cdot \rho \,, \tag{A.51}$$

$$q_{4_{\rho,\lambda}} = q_{2_{\rho,\lambda}} + 2\,\pi\,\mathbf{i} \cdot \rho \,, \tag{A.52}$$

$$q_{5_{\rho,\lambda}} = \phi_{f_\lambda} + \sigma_{s_\lambda} \,. \tag{A.53}$$

A.3.1.1 Singular polar coordinate case

Applying the singular relation given in eq. (7.1) reduces the substitution eq. (A.46)–(A.53) to

$$s_{1_{0,\lambda}} = \left(q_{1_{0,\lambda}} - q_{2_{0,\lambda}}\right) \cdot \left(q_{1_{0,\lambda}} + q_{2_{0,\lambda}}\right) \,, \tag{A.54}$$

$$s_{2_{0,\lambda}} = -\left(q_{1_{0,\lambda}} - q_{2_{0,\lambda}}\right) \cdot \left(\left(q_{1_{0,\lambda}} + q_{2_{0,\lambda}}\right) \cdot q_{1_{0,\lambda}} - 2 \cdot q_{5_{0,\lambda}}^2\right) \,, \tag{A.55}$$

$$s_{3_{0,\lambda}} = 2 \cdot \left(q_{1_{0,\lambda}} - q_{2_{0,\lambda}}\right) \cdot q_{5_{0,\lambda}}^2 - q_{2_{0,\lambda}} \cdot s_{1_{0,\lambda}} \,, \tag{A.56}$$

$$q_{1_{0,\lambda}} = \phi_{f_\lambda} + \sigma_{r_\lambda} \,, \tag{A.57}$$

$$q_{2_{0,\lambda}} = \phi_{f_\lambda} - \alpha_\lambda - \sigma_{r_\lambda} - 2 \cdot \sigma_{s_\lambda} \ , \tag{A.58}$$

$$q_{5_{0,\lambda}} = \phi_{f_\lambda} + \sigma_{s_\lambda} \ . \tag{A.59}$$

B Electrophotographic parameters

For the sake of completeness, the parameter values of the calibrated electrophotographic model are listed below. They belong to the calibrated model, which produces to the results shown in figure 9.3. The table represents the numerical values of the cyan (c) layer and may serve the reader as an initial point for any calibration attempt.

Parameters of equations (8.1)–(8.3)

$$L_1 = 1.0353\ mm\,, \qquad L_2 = 0.8852\ mm\,,$$
$$z \equiv 3.1000\ \mu m\,, \qquad \zeta = 30.1497\ \mu m\,,$$
$$C_0 = 0.8703\,, \qquad I_{sat} = 0.6747\,,$$
$$\eta \equiv 6.3000\,, \qquad \beta \equiv 0.3125\,.$$

Parameters of equation (8.5)

$$\mu = 0.5357\,, \qquad \upsilon = 0.7835\,,$$
$$\gamma = 1.9589\,.$$

Parameters of equation (8.6)

$$a = 1.2145\,, \qquad b = 0.8454\,.$$

Parameters of equation (8.8)

$$\tau_{imp} = 0.2393\,.$$

Parameters of equation (8.12)

$$\varepsilon_c = 93\,\%\,, \qquad \varepsilon_{c,all} = 99\,\%\,,$$
$$\varepsilon_{c,m} = 98\,\%\,, \qquad \varepsilon_{c,y} = 97\,\%\,.$$

Parameters of equation (8.13)

$$r_{\mathrm{F}} = 31\ \mu m\,.$$

The symbol "≡" denotes preselected values. Unless explicitly stated, the listed values are given in normalized units in accordance with the purpose of the thesis.

Backmatter

Bibliography

[AEZ95] J. S. Arney, P. G. Engeldrum, and H. Zeng. A modified Murray-Davies model of halftone gray scales. In *Proc. TAGA*, pages 353–363, 1995.

[Ber97] F. Berg. *Isotrope Lichtstreuung in Papier - Neue Überlegungen zur Kubelka-Munk-Theorie*. PhD thesis, Technische Hochschule Darmstadt, April 1997.

[Bra00] R. N. Bracewell. *The Fourier Transform and its Applications*. McGraw-Hill, 3rd. edition, 2000.

[Bri] Encyclopædia britannica. `<url: http://www.britannica.com/>`.

[BS97] I.N. Bronstein and K.A. Semendjajev. *Handbook of Mathematics*. Springer, Berlin, reprint of the third edition, 1997.

[Cal98] P. Callet. *Couleur-lumière Couleur-matière; interaction lumière-matière et synthèse d'images*. Diderot Multimedia, 1998.

[Cha60] S. Chandrasekhar. *Radiative Transfer*. Dover, New York, 1960.

[CIE78] CIE. *Recommendations on uniform color spaces—color-difference equations, psychometric color terms*, 1978. Supplement Publication № 2 to CIE Publ. № 15 (E-1.3.1) 1971.

[CIE86] CIE. *Standard Colorimetric Observers*, 1st edition, 1986. S 002.

[CIE95] CIE. *Technical Report; Industrial Colour-Difference Evaluation*, 1995. 116-1995.

[CY53] F. R. Clapper and J. A. C. Yule. The effect of multiple internal reflections on the densities of half-tone prints on paper. *Journal of the Optical Society of America*, 43(7):600–603, July 1953.

[Dem24] E. Demichel. *Le Procédé*, 26:17–21, 1924.

[EH98] P. Emmel and R. D. Hersch. Spectral colour prediction model for a transparent fluorescent ink on paper. In *6th Color Imaging Conference*, pages 116–122, Scottsdale, AR, 1998. IS&T/SID.

[EH99] P. Emmel and R. D. Hersch. Towards a color prediction model for printed patches. *IEEE Computer Graphics and Applications*, 19(4):54–60, July/August 1999.

[Emm98] P. Emmel. *Modèles de prédiction couleur appliqués à l'impression jet d'encre*. PhD thesis, École Polytechnique Fédérale de Lausanne, `<url: http://diwww.epfl.ch/w3lsp/publications/colour/>`, 1998.

[Eng99] P. G. Engeldrum. The Color between the Dots. In R. Eschbach, editor, *Recent Progress in Digital Halftoning II*, chapter V, pages 383–389. IS&T, 1999.

[Fai97] M. D. Fairchild. *Color appearance models*. Addison Wesley Inc., 1997.

[Fie99] G. G. Field. *Color and Its Reproduction*. GATF*Press*, 2nd. edition, 1999.

[FRGS82] G. Fischer, J. Rodriguez-Giles, and K. R. Scheuter. Ein physikalisches Modell für die Beschreibung von Lichtstreuprozessen. *Die Farbe*, 30(1/6):199–220, 1982.

[GB80] F. Grum and C. J. Bartleson, editors. *Color Measurement*, volume 2 of *Optical Radiation Measurements*, chapter Colorant Formulation and Shading, by Eugene Allen. Academic Press, 1980.

[GF00] S. Gonzalez and M. D. Fairchild. Evaluation of bispectral spectrophotometry for accurate colorimetry of printing materials. In *8th Color Imaging Conference*, volume 8, pages 39–43, Scottsdale, AR, 2000. IS&T/SID.

[Gra53] H. Grassman. Zur Theorie der Farbenmischung. *Ann. Phys.*, 89(69), 1853.

[Gui31] J. Guild. The colorimetric properties of the spectrum. *Philosophical Transactions of the Royal Society of London*, A230:149–187, 1931.

[Gus97] S. Gustavson. *Dot Gain in Colour Halftones*. PhD thesis, Dept. of Electrical Engineering, Linköping University, September 1997.

[HK98] I. Heikkilä and S. Karttunen. The interrelations between dot shape distortions and print quality. In *25th Research Conference*, pages 1–22, Pittsburgh, PA, August 1998. IARIGAI.

[Hun98] R. W. G. Hunt. *Measuring Color*. Fountain Press, 3rd. edition, 1998.

[IPS] The Robert C. Williams American Museum of Papermaking. `<url: http://www.ipst.edu/amp>`.

[ISO97] ISO-2846-1. *Graphic technology — Colour and transparency of ink sets for four-colour-printing —*, 1.st edition, Dec. 1997. the non-brightened APCO II/II paper is specified in Annex A.

[Jud42] D. B. Judd. Fresnel reflection of diffusely incident light. *Journal of Research of the National Bureau of Standards*, 29(329), November 1942. RP1504.

[JVS01] J. J. Joshi, D. B. Vaidya, and H. S. Shah. Application of multi-flux theory based on Mie scattering to the problem of modeling the optical characteristics of colored pigmented paint films. *Color Research and Application*, 26(3):234–245, June 2001.

[JW75] D. B. Judd and G. Wyszecki. *Color in Business, Science and Industry*. John Wiley & Sons, Inc., 3rd. edition, 1975.

[Kan99] H. R. Kang. *Digital Color Halftoning*. SPIE & IEEE, 1999.

[Kip01] H. Kipphan, editor. *Handbook of Print Media: Technologies and Production Methods*. Springer, 2001.

[KM31] P. Kubelka and F. Munk. Ein Beitrag zur Optik der Farbanstriche. *Zeits. f. techn. Physik*, (12):593–601, 1931.

[Kub48] P. Kubelka. New contributions to the optics of intensely light-scattering materials. part I. *Journal of the Optical Society of America*, 38(5):448–457, May 1948.

[Kub54] P. Kubelka. New contributions to the optics of intensely light-scattering materials. part II: Nonhomogenous layers. *Journal of the Optical Society of America*, 44(4):330–335, April 1954.

[LA01] D. L. Lau and G. R. Arce. *Modern Digital Halftoning*. Signal Processing and Communications. Marcel Dekker, 2001.

[Leu93] A. Leutert, editor. *Allgemeine Fachkunde der Drucktechnik*. Baden-Verlag, 11th. edition, 1993.

[Mat01] MathWorks. MATLAB™ *Optimization Toolbox*, version 2.1.1, release 12.1, 2nd edition, 2001. consider especially lsqcurvefit and fmincon.

[MEH00] S. Mourad, P. Emmel, and R. D. Hersch. Predicting monochrome color transmittance spectra of electrophotographic prints. In *International Conference on Digital Printing Technologies, NIP16*, pages 862–866, Vancouver, B.C., 2000. IS&T.

[MEH01] S. Mourad, P. Emmel, and R. D. Hersch. Predicting transmittance spectra of electrophotographic color prints. In *Color Imaging: Device-Independent Color, Color Hardcopy, and Graphic Arts VI*, volume 4300, pages 50–57, San Jose, CA, 2001. SPIE/IS&T.

[MESH01] S. Mourad, P. Emmel, K. Simon, and R. D. Hersch. Extending Kubelka-Munk's theory with lateral light scattering. In *International Conference on Digital Printing Technologies, NIP17*, pages 469–473, Fort Lauderdale, FL, 2001. IS&T.

[MESH02] S. Mourad, P. Emmel, K. Simon, and R. D. Hersch. Prediction of monochrome reflectance spectra with an extended Kubelka-Munk model. In *10th Color Imaging Conference*, volume 10, pages 298–304, Scottsdale, AR, 2002. IS&T/SID.

[MR71] P. S. Mudgett and L. W. Richards. Multiple scattering calculations for technology I. *Journal of Applied Optics*, 10(7):1485–1502, July 1971.

[MR72] P. S. Mudgett and L. W. Richards. Multiple scattering calculations for technology II. *Journal of Colloid and Interfaces Science*, 39(3):551–567, June 1972.

[Mur36] A. Murray. A monochrome reproduction in photoengraving. *J. Franklin Inst.*, 221:721–744, 1936.

[Neu37] H. E. J. Neugebauer. Die theoretischen Grundlagen des Mehrfarbenbuchdrucks. *Zeitschrift für Photophysik und Photochemie*, 36(4):73–89, 1937.

[Neu65a] H. E. J. Neugebauer. A describing function for the modulation transfer of xerography. *Applied Optics*, 4(4):453–459, 1965.

[Neu65b] H. E. J. Neugebauer. *Xerography and Related Processes*, chapter 9, Electrostatic Fields of Xerographic Images, pages 217–257. Focal Press, New York, 1965.

[Neu67] H. E. J. Neugebauer. Development method and modulation transfer function of xerography. *Applied Optics*, 6(5):943–945, 1967.

[Neu00] Neusiedler. Color Copy paper. `<url: http://www.neusiedler.com>`, 2000. brightened, highly opaque office paper.

[NG93] C. Neß and L. Göttsching. Übertragung von Linienrastern im Offsetdruck und deren drucktechnische Bedeutung. *Das Papier*, 47(7):353–363, 1993.

[NGM98] R. J. Nash, M. L. Grande, and R. N. Muller. The effect of toner and carrier composition on the average and distributed toner charge values. In *International Conference on Digital Printing Technologies, NIP14*, pages 332–340, Toronto, Ontario, 1998. IS&T.

[PID01] B. Philips-Invernizzi and D. Dupont. Bibliographical review for reflectance of diffusing media. *Optical Engineering*, 40(6):1082–1092, June 2001.

[Ran82] H. F. Rance, editor. *Handbook of Paper Science*, volume 2, chapter Optical properties of paper, by J. A. Van den Akker. Elsevier, 1982.

[RH78] F. R. Ruckdeschel and O. G. Hauser. Yule-Nielsen effect in printing: a physical analysis. *Applied Optics*, 17(21):3376–3383, November 1978.

[Rog97] G. Rogers. Optical dot gain in a halftone print. *Journal of Imaging Science and Technology*, 41(6):643–656, November/December 1997.

[Rog99] G. Rogers. Optical dot gain: Lateral scattering probabilities. In R. Eschbach, editor, *Recent Progress in Digital Halftoning II*, chapter V, pages 495–500. IS&T, 1999.

[Rog00] G. Rogers. A generalized Clapper-Yule model of halftone reflectance. *Color Research and Application*, 25(6):402–407, December 2000.

[Sau42] J. L. Saunderson. Calculation of the color of pigmented plastics. *Journal of the Optical Society of America*, 32(4):727–736, 1942.

[SB59] W. S. Stiles and J. M. Burch. N.P.L. Color-matching investigation: Final report. In *Optica Acta*, volume 6, 1959.

[Sch05] A. Schuster. Radiation through a foggy atmosphere. *Astrophysics Journal*, 21(1), 1905. Reprinted in "Selected Papers on te Transfer of Radiation by D. H. Menzel, editor, Dover Publications, NY, 1966.

[Sch75] R. M. Schaffert. *Electrophotography*. Focal Press, London, New York, 2nd. edition, November 1975.

[Sch96] L. B. Schein. *Electrophotography and Development Physics*. Laplacian Press, rev. 2nd. edition, 1996.

[Sch02] K. Schläpfer. *Farbmetrik in der grafischen Industrie*. UGRA, St. Gall, 3rd. edition, 2002.

[SM93] Y. Shiraiwa and T. Mizuna. Equation to predict colors of halftone prints considering the optical properties of paper. *Journal of Imaging Science and Technology*, 39:385–391, 1993.

[SNY98] I. Shinichi, T. Norimichi, and M. Yoichi. Analyzing CTF of print by MTF of paper. *Journal of Imaging Science and Technology*, 42(6):572–576, November/December 1998.

[SOS98] E. J. Stollnitz, V. Ostromoukhov, and D. H. Salesin. Reproducing color images using custom inks. In *Computer Graphics Proceedings*, Annual Conference Series, pages 267–274, Orlando, FL, July 1998. SIGGRAPH.

[Spe59] N. I. Speranskaya. Determination of spectrum color coordinates for twenty-seven normal observers. *Optics and Spectroscopy*, 7(424), 1959.

[Spr97] A. W. Springsteen. Fluorescence and color, an overview of the fundamentals of measuring fluorescent color. Technical report, Labsphere, 1997.

[Tuc47] L. B. Tuckerman. On the intensity of the light reflected from or transmitted through a pile of plates. *Journal of the Optical Society of America*, 37(10):818–825, 1947.

[Vig85] J. A. S. Viggiano. The color of halftone tints. In *Proc. TAGA*, pages 647–661, 1985.

[Vig90] J. A. S. Viggiano. Modeling the color of multi-colored halftones. In *Proc. TAGA*, pages 44–62, 1990.

[WB00] D. R. Wyble and R. S. Berns. A critical review of spectral models applied to binary color printing. *Color Research and Application*, 25(1):4–19, February 2000.

[Wil84] E. M. Williams. *The Physics and Technology of Xerographic Processes*. John Wiley & Sons, Inc., 1984.

[Wol00] Wolfram Research, Inc. MATHEMATICA®, version 4.1.0.0 edition, 2000. <url: http://www.wolfram.com>.

[Wri28] W. D. Wright. A re-determination of the trichromatic coefficients of the spectral colours. *Transactions of the Optical Society*, (30):141–164, 1928.

[WS82] G. Wyszecki and W. S. Stiles. *Color Science*. John Wiley & Sons, Inc., 2nd. edition, 1982.

[XHs] The Story of Xerography. <url: http://www.xerox.co.in/aboutxerox/storyX.asp>.

[YGK01] L. Yang, S. Gooran, and B. Kruse. Simulation of optical dot gain in multichromatic tone reproduction. *Journal of Imaging Science and Technology*, 45(2):198–204, March/April 2001.

[YN51] J. A. C Yule and W. J. Nielsen. The penetration of light into paper and its effect on halftone reproduction. In *Proc. TAGA*, pages 65–75, 1951.

Biography

Personal data

Safer Mourad was born on 2 August 1968 in Damascus, Syria, where he completed his schooling in 1986. In 1987 he moved to his mother's country, Switzerland, where he pursued a degree in electronic engineering at the Swiss Federal Institute of Technology (ETH), Zurich. In 1993 he received the diploma entitled "Diplomierter Elektroingenieur der ETH-Zürich" (Master's Degree in Electrical Engineering). From 1993 to 1997 he developed software and hardware algorithms for real-time video tracking and high-end surveying instruments at Leica Geosystems in Heerbrugg, Switzerland. In 1998 he joined the Media Technology Department at the Swiss Federal Laboratories for Materials Testing and Research (EMPA) in St. Gallen. Focusing on electrophotographic applications, he has been working on color reproduction and Kubelka–Munk-based approaches of light scattering within paper. His research interests include system modeling and identification, colorimetry, image processing and real-time control applications.

He is a citizen of Switzerland and Syria, and lives near St. Gallen. He is married and has three daughters.

Scientific publications

B. Sprenger, L. Kucera , and S. Mourad
Balancing of an Inverted Pendulum with a SCARA Robot. *IEEE/ASME Transactions on Mechatronics* 3(2):91–97, June 1998.

H. Künzli, A. Noser, M. Loher and S. Mourad
Prediction of colorimetric measurements in newspaper printing using neural networks. In *Color Imaging: Device-Independent Color, Color Hardcopy, and Graphic Arts IV*, volume 3648, pages 11–17, San Jose, CA, 1999. SPIE/IS&T.

S. Mourad, P. Emmel, and R. D. Hersch
Predicting monochrome color transmittance spectra of electrophotographic prints. In *International Conference on Digital Printing Technologies, NIP16*, pages 862–866, Vancouver, BC, 2000. IS&T.

S. Mourad, P. Emmel, and R. D. Hersch
Predicting transmittance spectra of electrophotographic color prints. In *Color Imaging: Device-Independent Color, Color Hardcopy, and Graphic Arts VI*, volume 4300, pages 50–57, San Jose, CA, 2001. SPIE/IS&T.

S. Mourad, P. Emmel, K. Simon, and R. D. Hersch
Extending Kubelka–Munk's theory with lateral light scattering. In *International Conference on Digital Printing Technologies, NIP17*, pages 469–473, Fort Lauderdale, FL, 2001. IS&T.

S. Mourad, P. Emmel, K. Simon, and R. D. Hersch
Prediction of monochrome reflectance spectra with an extended Kubelka–Munk model. In *10th Color Imaging Conference*, volume 10, pages 298–304, Scottsdale, AR, IS&T/SID, 2002.

Languages

Arabic	mother tongue
German	mother tongue
English	spoken and written
French	spoken

Awards

Swiss SEV/IEEE prize for diploma thesis entitled "Balancing of an inverted pendulum with a robot", 1993.

E-mail address: safer.mourad@empa.ch

Index